UiT The Arctic University of Norway

The Faculty of science and technology
Department of Geoscience

The relationship between shallow anomalies and gas-flaring on the flank of the Nordkapp Basin in the SE Barents Sea

Joakim Haldorsen

Master thesis in petroleum geology, GEO-3900

May 2020

Abstract

This study investigates the north-east-subbasin of the Nordkapp Basin in the Barents Sea. Main focus has been on mapping shallow seismic anomalies from 3D data, their potential association with faulting and sub-surface structures, and further to compare the occurrence of seismic anomalies to possible gas-flares above the seabed from water column data.

The stratigraphic intervals from Triassic to Cretaceous have been mapped and several seismic anomalies interpreted to be bright spots are identified. The majority of the anomalies are observed in the Cretaceous Kolmule- and Kolje formations, and several are associated with rotated fault blocks giving rise to structural closures (structure A and B) along the Thor Iversen Fault Complex.

A possible meteorite impact crater is observed within the Kolmule Formation, suggested to form during Early Albian and is referred to as structure C. Bright spots were observed along the flanks of this structure. Water column data suggest, no gas flares observed above structure A-C, which could indicate that these structures are sealing.

In total, seven lines with gas flares was observed, associated with shallow faults, truncations and shallow anomalies. The potential gas flares had a relatively weak amplitude, suggesting a corresponding weak gas flow and might indicate low concentration/supply of gas or sealing of potential gas migrating upwards. Locally, other seismic amplitude anomalies were identified below the URU/seafloor, however still without clear observations of gas flares in the water column above. A possible explanation for this lack of gas flares above such shallow anomalies, might suggest that glacigenic sediments, usually dense and mudrich, could in places act as an impermeable barrier for gas into the water.

Preface

A 60 ECT thesis was written to complete a master's degree in petroleum geology at the Artic University of Norway (UiT). Stig-Morten Knutsen (NPD/UiT), Pavel Serov (UiT) and André Jensen (NPD) have all been supervisors for this study. Water column data was acquired from MAREANO, the seismic data was provided by TGS and was organized by NPD. The different assumption and views expressed in this study are solely based on the authors view and doesn't necessarily mirror that of TGS and MAREANO.

Acknowledgements

Fem år med skole er omsider forbi, som er vemodig og herlig på samme tid. Det siste året har vært fullt med ny kunnskap, irritasjon og isolasjon (pga. covid 19, hvor alle har blitt påvirket på et eller annet vis).

Jeg er veldig takknemlig for all hjelp jeg har fått gjennom dette året og vil dermed takke min hovedveileder Stig-Morten Knutsen, og biveileder Pavel Serov og André Jensen. Dere har vært veldig tålmodige, tilgjengelig, og rask og flink med tilbakemeldinger. Det har vært en omfattende oppgave med masse nye og tidkrevende elementer og det har derfor vært utrolig fint med gode mentorer!

Jeg ønsker også å rette en stor takk til familie og venner for all støtten dette året! Takk til mor og far for gode ord og økonomisk støtte. Takk til John-Einar, Steinar og Joakim for morsomme stunder, hadde ikke vært det samme uten dere! Takk til Oda for støtte og gode middager! Jeg vil også takke alle på geologibygget, kommer til å savne dere alle!

Til slutt, en stor takk til MAREANO for tilgang til vannkolonne data, til TGS for tilgangen til seismisk data og til oljedirektoratet for tilrettelegging av oppgave.

Table of Contents

1 Introduction

1.1 Study area and objective

The study area is located in the eastern parts of the Nordkapp Basin in the Norwegian Barents Sea, covering approximately 3000 km2, at water depth of approximately 220 m (Figure 1.1). The main objective of the study will be to map the shallow seismic anomalies using 3D-seismic dataset and investigate the relationship to sub-surface structures and faulting. These results will then be used and compared to mapping of gas-flares from the seafloor using the software FM Midwater on water column data acquired by the MAREANO-program. Triassic to Cretaceous strata will be investigated, with special focus on Cretaceous stratigraphy.

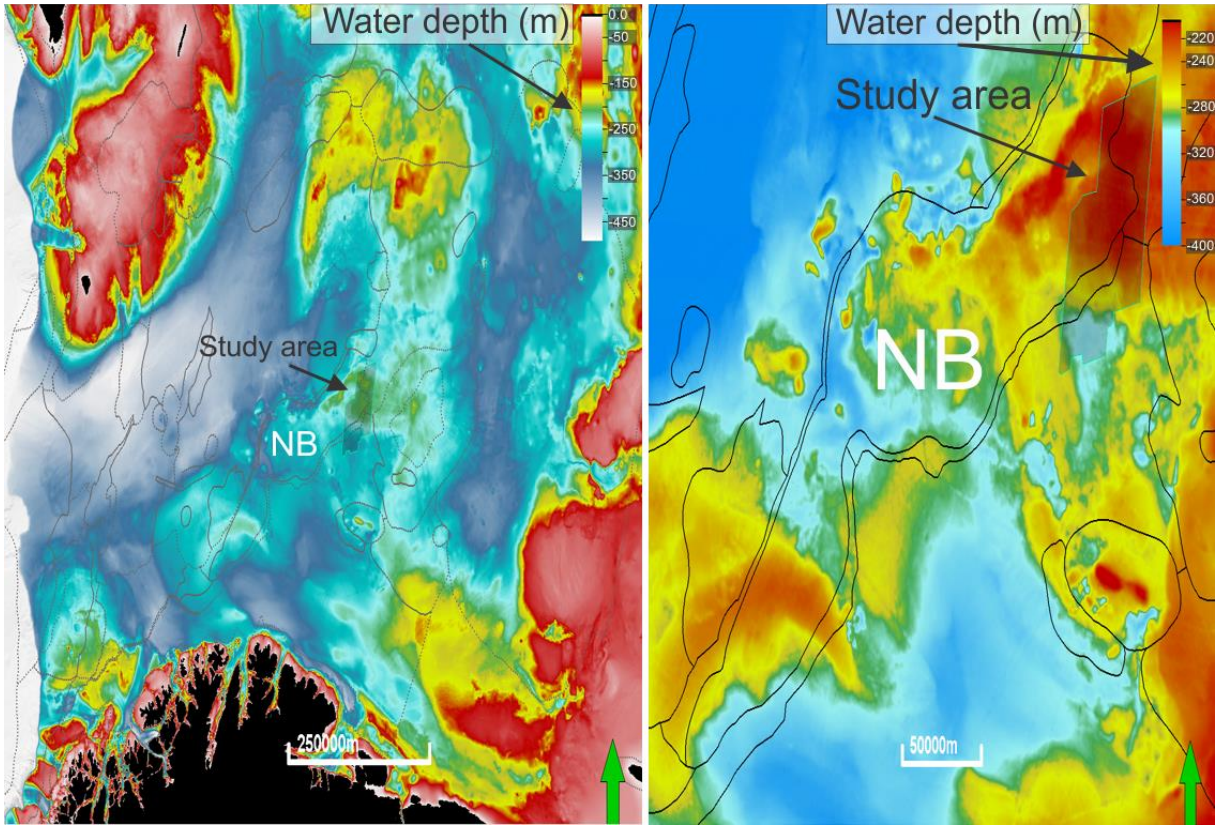

Figure 1.1: A) Bathymetric map with water depth (m) over the western Barents Sea and the location of the study area. B) Bathymetric map with water depth over the Nordkapp Basin and the location of the study area. NB=Nordkapp Basin. Structural elements was acquired from NPD. Bathymetric map was acquired from IBCAO.

1.2 Nordkapp Basin

The Nordkapp Basin has an irregular stretched out shape and are defined by Måsøy, Thor Iversen and The Nysleppen Fault Complexes (Figure 2.3). The basin has a characteristic graben structures and is bounded by the Finnmark Platform in the south and the Bjarmeland Platform in the north (Figure 2.3) (Larssen et al., 2002). The general trend of the Nordkapp Basin is NE-SW with the exception of the central parts favouring E-W orientation (Larssen et al., 2002). The Nordkapp Basin is a deep Palaeozoic basin and extends over 300 km in length and 30-80 km in width (R. Gabrielsen et al., 1990). It is believed that the basin has its origin in the late Devonian to Carboniferous time and are consisting of large amounts of salt. The specific location of the Nordkapp Basin is 71°30'N, 25°E and 73°30'N, 34°E (Figure 2.3).

1.2.1 Sub-basins in the Nordkapp Basin

The Nordkapp Basin is divided into three subbasins (Figure 3.5): the southwestern subbasin with a northeast-southwest orientation, central subbasin with an east-west trend and the northeast-southwest oriented northeastern subbasin (Gudlaugsson et al., 1998; Grimstad, 2016; Cedeño et al., 2019; Rojo et al., 2019). There are also theories suggesting the Nordkapp Basin is divided into two adjacent opposing half grabens: Nordkapp Basin North and Nordkapp Basin South (R. Gabrielsen et al., 2013). The NE subbasin is the focus of this thesis, and is bounded by the Bjarmeland Platform in the north and the Finmark Platform in the south. The two margins meet as the northeastern subbasin and narrows towards the north at the crest of the Veslekari Dome. The Thor Iversen Fault complex defines the subbasin in the south and separates the NE subbasin from the Finmark Platform and the Polstjerna Fault complex defines the subbasin in the north separating it from the Bjarmeland Platform.

1.2.2 The Thor Iversen Fault Complex

The Thor Iversen Fault Complex defines the eastern margin of the Nordkapp Basin, through the study area of this thesis (Figure 3.5, 4.2-4.3 and 4.10). The fault complex has an extensional characteristics with a W-E trend in the south and changes gradually to NE-SW to the north before it dies out at 34°E. The Thor Iversen Fault Complex is believed to be of Early Carboniferous age, with later reactivation in Mesozoic and Cenozoic (R. H. Gabrielsen et al., 1990). The fault complex also has direct ties with salt pillows, in other words interaction between faulting and salt tectonics (Rojo et al., 2019).

1.3 Petroleum exploration in the Nordkapp Basin

Petroleum exploration in the Nordkapp Basin was first initiated in the 1980s (Bugge et al., 2002). Several wells have been drilled in the region since; 7124/3-1, 7125/1-1, 7226/11-1, 7228/9-1S, 7228/7-1A, 7229/11-1, 7228/2-1S and 7435/12-1 (Figure 3.5 and Table 3.2). Exploration wells in the Nordkapp Basin are all proven to be dry except for 7228/7-1A (Table 3.2), which was still considered a noncommercial discovery (Rojo et al., 2019). In this well gas was found in the Lower and Upper Triassic reservoir intervals, which is proof of a

working petroleum system in the western subbasin (Bugge et al., 2002). The abundance of salt in the Nordkapp Basin makes it difficult to map in 2D seismic. No exploration wells exist to date in the NE subbasin (Figure 3.5), although 2D seismic data from the flank of the Nordkapp Basin show shallow seismic-anomalies believed to be fault related (Rojo et al., 2019).

2 Geological background

The Barents Sea Shelf was developed as a response to the breakup of Pangea in late Paleozoic and Mesozoic forming highs, basins (including the Nordkapp Basin) and platforms in the eastern parts of the Barents Sea (Jan I Faleide et al., 1993). The Barents Sea shelf consists of two major geological provinces categorized as the western and eastern province, covering an area of about 1.3 million km^2 (Worsley, 2008). The western province corresponds to the Norwegian part of the Barents Sea, whereas the eastern province corresponds to the Russian part. The geology of the two provinces differ greatly, the western province is of a much more complex nature because of several tectonic episodes, leading to the formation of highs, platforms and basins (Faleide et al., 1993). The Nordkapp Basin and the study area is located within the western province (Figure 2.1).

The western Barents Sea can be further divided into three geological regions. These regions are the Svalbard Platform, the province between the Svalbard Platform and Norwegian Coast and the western Barents Sea-Svalbard continental margin. The western Barents Sea contains two passive margins in northern and southern part of the province (Faleide et al., 1993). The structural elements in the Barents Sea developed in three different phases: Carboniferous, Late Jurassic-Early Cretaceous and Late Cretaceous-Paleocene (Figure 2.1) (Glørstad-Clark et al., 2010).

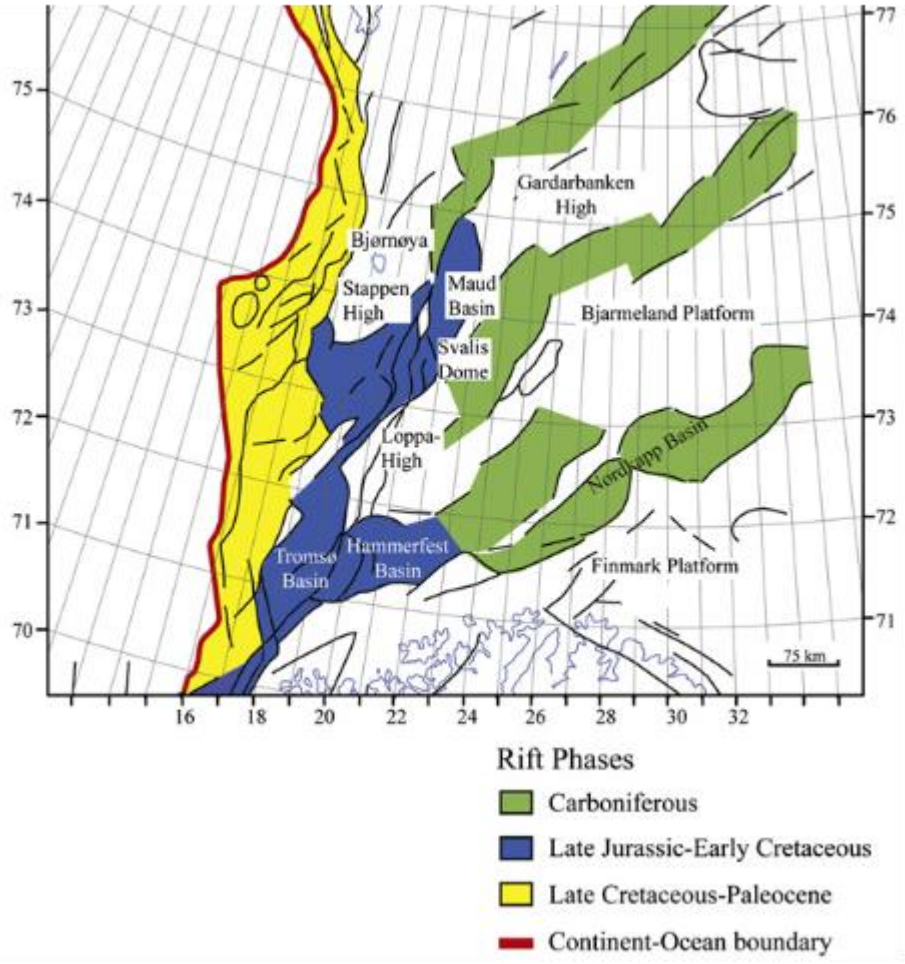

Figure 2.1: Main structural elements in the Barents Sea, the periods of the tectonic activity and associated structural elemetns are indicated by the colors. The figure is modified from Glørstad-Clark et al. (2010).

2.1.1 Structural elements in the Southwestern Barents Sea

Paleozoic

The Caledonian-Orogeny occurred approximately 400 million years ago in the Devonian and is known as the earliest event that affected the basement of the western Barents Sea. This event resulted in closing of the Iapetus Ocean, metamorphoses of the Barents Sea Shelf basement and to NE-SW trending grains (Faleide et al., 1993; Gabrielsen et al., 1990). The earliest event affecting the Barents Sea have likely influenced later structural trends, following this NE-SW orientation (Faleide et al., 2015). In mid Carboniferous a wide rift zone occurred in the southern parts of the Barents Sea, with extensional features, forming half graben basins bounded by faulted highs (Faleide et al., 2015). The orientation of the faults in

the western parts of the Barents Sea margin is dominated by a N-S strike, whereas the eastern and central parts have the same trend as the Caledonian orogeny (NE-SW orientation) (Gabrielsen et al., 1990; Smelror et al., 2009). Several basins were formed during the Carboniferous rift phase, including Nordkapp-, Bjørnøya-, Maud-, and Fingerdjupet basins (Figure 2.1).

During the Carboniferous period sediments were deposited in wide depressions and narrow grabens (Faleide et al., 2015). The earliest stratigraphic unit in Carboniferous is represented by the Billefjorden Group, consisting of continental and shallow marine siliciclastic deposits with coal beds (Figure 2.2, Larssen et al., 2002). A mix of siliciclastic sediments and carbonate shelf sediments in the west (Loppa High region) and sandstones in the south (Finmark Platform region) dominate the latest periods of the. Carboniferous to Permian age was dominated by arid climate, resulting in the formation of evaporates and dolomites (Larssen et al., 2002; Smelror et al., 2009).

Mesozoic

The Permian-Early Triassic was subject of basement involved extension as mentioned above, followed by a tectonic quite period (Faleide et al.,1993). The completion of the supercontinent Pangea led to the several episodes of orogenesis, such as the Uralides and the Caledonides. These mountain ranges were responsible for a large amount of clastic sediments into the Barents Sea, especially from the Uralides in the east. Sediments from the Uralides formed thick sediment wedges in the East-Barents Sea, prograding as deltaic systems towards the West-Barents Sea in a NW direction (Glørstad-Clark et al., 2010). The sediment package originating from the Uralides was therefore thickest in the eastern parts of the Western-Barents Sea, showing a regional thinning towards the west/northwest (Glørstad-Clark et al., 2010). A difference in loading occurred due to the difference in thickness in the Barents Sea, which affected the salt in the Nordkapp- and Maud basins, resulting in salt tectonics (R. Gabrielsen et al., 1990). Minor tectonic events occurred during Middle-Late Triassic, although the period was characterized by post-rift thermal subsidence (Smelror et al., 2009).

During Middle Jurassic to Early Cretaceous the southwestern Barents Sea was influence by renewed rifting in the North Atlantic forming highs and rift basins like; Bjørnøya-, Harstad-,and Tromsø basins. A northward propagation of the rift led to a marine connection along the Barents Shelf, representing a marine seaway (Smelror et al., 2009). The reactivated

extensional faults followed the strike-slip movement of the already existing structural lineaments (Worsley et al., 2008).

Late Jurassic-Early Cretaceous was dominated by large scale rifting events and a thick layer of organic shale, giving rise to the Hekkingen Formation (Figure 2.2) (Jan I Faleide et al., 1993). The impact of the Atlantic rifting reached all the way to the South-Western Barents Sea, resulting in further expanding of Harstad- and Tromsø basins. During the Early Cretaceous, the northern parts of the Barents Sea Shelf were significantly uplifted. As the northeastern areas experienced uplift, massive amounts of sediments migrated to the subsiding basins in the southwest (Faleide et al., 1993). The Early Cretaceous uplift is believed to be related to the different volcanic events located on Franz Josef Land, Kong Karls Land and nearby areas. The rates of subsidence observed in the Bjørnøya-, Sørvestnaget-, Harstad- and Tromsø basins were high, resulting in a massive sedimentary sequence consisting of mudstones (R. H. Gabrielsen et al., 1997). In contrast, signs of local inversion are found during Early Cretaceous along the Ringvassøy-Loppa Fault Complex and where it borders Asterias Fault Complex. Because of little bottom circulation in Early Cretaceous deposition of shale and claystone was most common, especially in the basins located in the SW of the Barents Sea (Smelror et al., 2009). The end of Cretaceous was still dominated by extensional tectonics on a regional scale. During this period folding and reverse faulting (in some cases combined with extensional faulting) became increasingly common (R. Gabrielsen et al., 1990). The rifting between Greenland and Norway was gradually being dominated by strike-slip movements in this period (Smelror et al., 2009)

Cenozoic

In the late Cretaceous–Paleocene, rifting continued and the Norwegian margin was formed as a response to the continental breakup of Norway and Greenland at around 54-55 Ma (Early Eocene) (Faleide et al., 2008). The continental breakup was dominated by extension, despite several local reverse and transverse faults. Before the breakup in the Norway-Greenland sea, a transpressive event occurred, leading to crustal shortening (estimated to be about 30 km) between the northern margin of the Barents Sea Shelf and Svalbard (Smelror et al., 2009). The seafloor spreading of the Norwegian-Greenland Sea is connected to the Arctic Eurasia Basin by the regional De Geer megashear zone system and are characterized by major Vulcanic events (Jan Inge Faleide et al., 2008).

Eocene

In Eocene the opening of the Norwegian-Greenland Sea occurred, the Barents Sea-Svalbard margin was developed as continent to continent shear and the breakup continued developing into an ocean to ocean shear margin. During Eocene most of the eastern and northern sections of the Barents Sea were uplifted, whereas the western parts continued to subside, evident by missing Eocene strata in the eastern and northern parts of the Barents Sea (Lasabuda et al., 2018). Because of this trend, the sediments were migrating from the north and eastern parts of the Barents Sea towards the west. Several basins and rifted areas were filled with clastic sediments deposited in submarine fans, from the newly uplifted areas (Smelror et al., 2009). The Eocene sediment succession primarily consist of clastic deposition, and sandstones of gravity flow origin are found in drill cores from the Sørvestnaget Basin. Marine mudstones dominate Palaeocene and lower Eocene successions in the Hammerfest Basin and the western sections of the Nordkapp Basin. The underlying Cretaceous layer with a clear unconformity marks a pause in deposition (Smelror et al., 2009). The Cenozoic is on the other hand altogether removed/absent from the Finnmark and Bjarmeland platforms below the base of the Quaternary.

Oligocene

Early Oligocene was affected by an extensional plate movement with a more westerly motion in addition to marine shallowing (Faleide et al., 2008). The Vestbakken Volcanic Province was reactivated in this period with the same faulting trend (NE-SW) and the magmatism continued. The opening of the Fram Straight and a deep-water gateway between the Arctic and North Atlantic oceans was later developed as a result of a continues separation of the Greenland and the Barents Shelf (Lasabuda et al., 2018).

Late Neogene – Plio-Pleistocene

Late Neogene was dominated by uplift and erosion throughout the western Barents Sea Shelf. The entire Barents Sea Shelf was later uplifted and eroded in Late Plio-Pleistocene (Lasabuda et al 2018). The large scale regional uplift in Neogene has limited the extent of Neogene sediments in the Eastern parts of the Barents Sea. Wellbores drilled in the Vestbakken Volcanic Province and in the Sørvestnaget Basin show outer shelf to slope sediments (Smelror et al., 2009). The extensive uplift and erosion of the Barents Sea in late Plio-Pleistocene, led to huge amounts of sediments developing into large-scale submarine

depositional depocenters across the western margin. This sediment succession was thickest in the western parts of the Barents Sea, accumulating up to 4 km-thick glacigenic sediment packages in the Bjørnøya and Storfjorden fans and was deposited through several episodes of glaciation followed by isostatic uplift (Smelror et al., 2009). 2-3 km of sediments was removed from Svalbard, adjacent areas and platform areas in the northern Barents Sea as a consequence of the maximum uplift and erosion that took place (Lasabuda et al., 2018). The southern areas such as the Nordkapp and Hammerfest basins as well as the Loppa High was slightly less affected by the uplift with less than 2 km of sediments removed on average (Lasabuda et al., 2018).

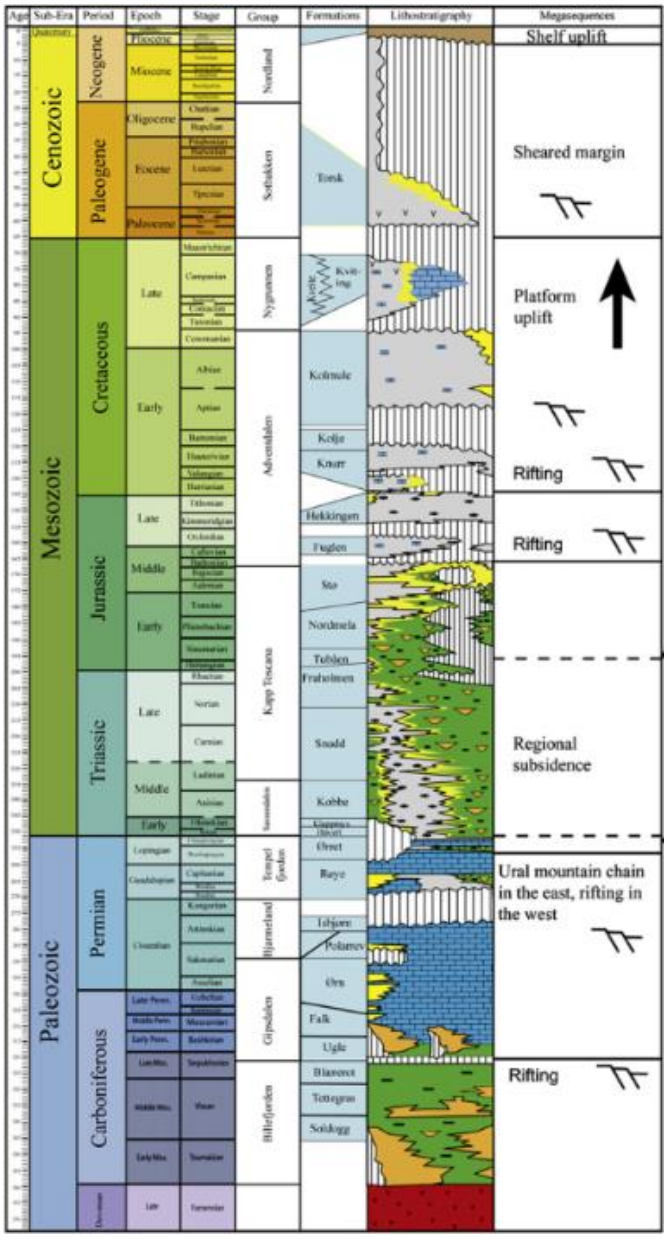

Figure 2.2: Lithostratigraphy, formations and group names of the western Barents Sea. Acquired from Glørstad-Clark et al. (2010).

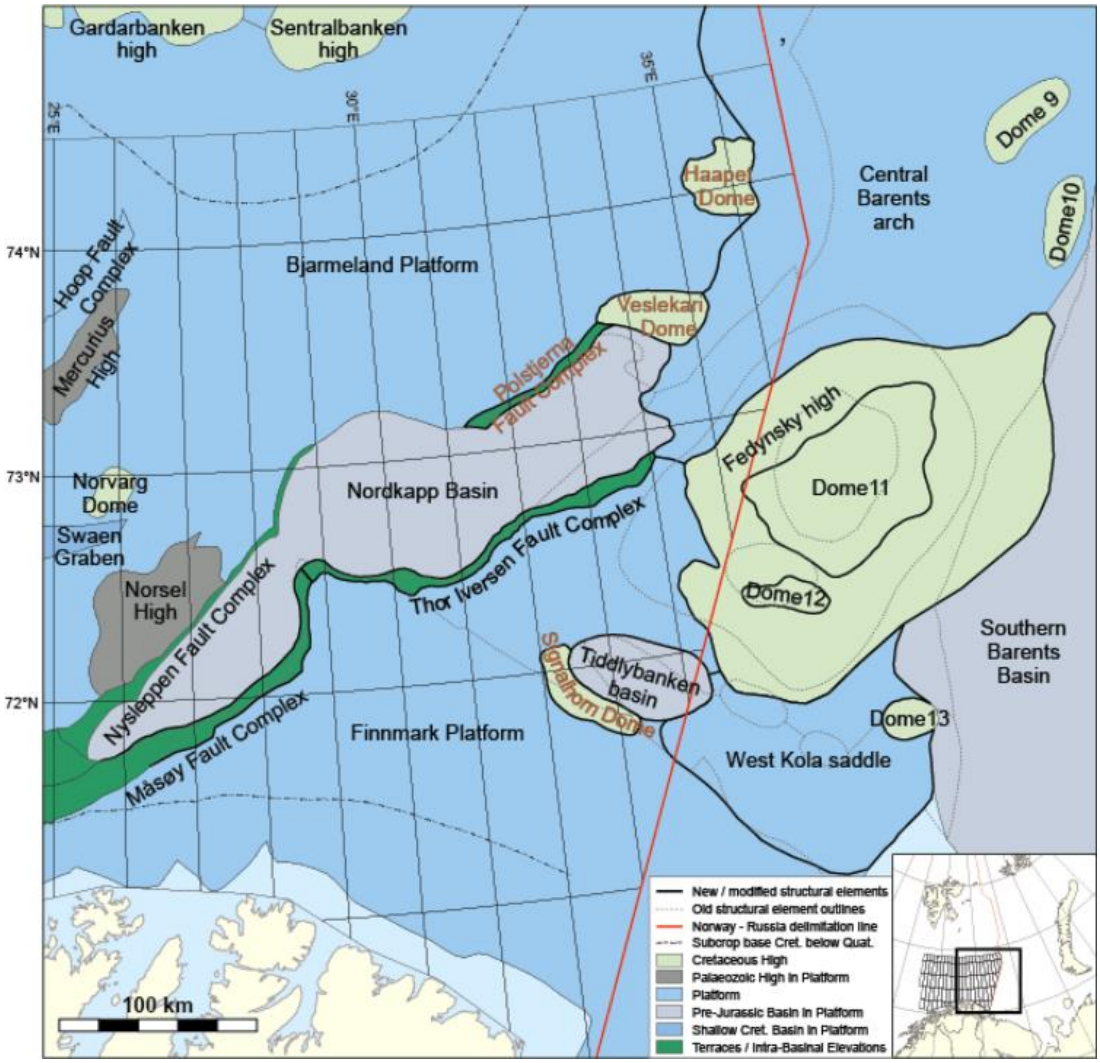

Figure 2.3: Structure elements of the Nordkapp Basin. Modified from Mattingsdal et al. (2015).

2.1.2 Geological history of the Nordkapp Basin

Late Paleozoic

The Nordkapp Basin is believed to have formed in late Devonian to Carboniferous as a result of the Devonian-Mississippian rifting of the Caledonian orogeny, along its NE-SW and SW-SE structures (Rojo et al., 2019). The basin was influenced by two separate extensional regimes, giving rise to the three sub-basins which are the NE-subbasin, central subbasin and

SW subbasin (Figure 3.5). The sediments deposited in Early to Middle Permian can be divided into two lithostratigraphic groups, characterized by their difference in depositional environment in response to variations of climate, tectonics and relative sea level changes. Deposition of evaporitic sediments dominated the Early Permian as a response to the arid climate (Larssen et al., 2002). Passive subsidence during Mid-Permian, led to a rising of the relative sea level, changing the depositional environment, where cold water carbonates where deposited (Figure 2.2). The carbonate build-ups during this period led to uneven loading over the salt layer, resulting in minor salt mobilization (Gabrielsen et al., 1990).

Mesozoic

The sediments derived from the uplifted Uralides to the east (see above) led to prograding of deltaic systems towards the West-Barents Sea in a NW direction and developed into marine and fluviodeltaic deposits, as a response to regional shallowing in Late Triassic-Early Triassic (Rojo et al., 2019). The North Atlantic rifting was initiated during Late Jurassic, which primarily affected the southwestern margin and had little impact on the Nordkapp Basin. During this period the Nordkapp Basin was influenced by passive subsidence, resulting in marine fine grained siliclastics deposits in addition to organic rich shale sediments, due to the anoxic conditions (Rojo et al., 2019). The Early Cretaceous uplift and magmatism of the northern parts of the Barents Sea shelf, caused deposits to migrate toward the south, including the Nordkapp Basin. The anoxic conditions of the area ceased, and were replaced by mainly fine grained sediments.

The fault controlled Nordkapp Basin, is dominated by salt structures and assumed to be initiated during Late Induan time (Jensen & Sørensen, 1992; Koyi et al., 1993, 1995; Nilsen et al., 1995; Grimstad, 2016). There are two triggering mechanism believed to be the cause of the mobilization: a) Permian-Triassic extension in the western margin of the Barents Sea as suggested by (Jensen & Sørensen, 1992; Koyi et al., 1993, 1995; Nilsen et al., 1995), b) differential loading in response to the Early Triassic progradation of the non-uniform Uralian sediment package (Dengo & Røssland, 1992) (M. Rowan & Lindsø, 2017), or c) a combination of both (Grimstad, 2016) (Rojo et al., 2019). Salt mobilization was triggered again, this time in Olenkian time and is known as the main diapir stage. Salt diapirs was piercing through the overburden on a large scale during this period, creating a salt induced depocenter regulating the sedimentation in the northeast and central subbasin (Grimstad, 2016) (Rojo & Escalona, 2018). The salt mobilization during Olenkian marks the transition

between reactive and passive diapirsm, becoming passive as previous reactive structures pierces through the overburden (Grimstad, 2016; Rojo & Escalona, 2018). The strata were domed and faulted as a response to reactivation of salt diapirs intruding upwards (Grimstad, 2016).

Cenozoic

During the transition from Late Cretaceous to Cenozoic, the Nordkapp Basin has been through several contraction events, associated with the opening of the North Atlantic, resulting in reactivation of faults and salt (Rojo et al., 2019). Several episodes of uplift and erosion dominated the Cenozoic and together with the Pleistocene glacial erosion, 1300 to 1500 m of sediments were removed in the Nordkapp Basin (Henriksen et al. (2011a). Majority of the Cenozoic unit is therefore missing in the Nordkapp Basin, especially the in the central and NE subbasin. The eroded strata during this time, led to the development of an unconformity between the deformed Lower Cretaceous and the overlying Quaternary rock unit, categorized as the upper regional unconformity (URU) (Andreassen et al., 2008).

3 Theory, data and method

3.1 Theory

3.1.1 Introduction to faults

A fault in geological terms is displacement of a volume of rock shown as a discontinuity or as a planar rock fracture. These discontinuities are seldom clean fractures but have a rather complex deformation (Oglesby, 2005). The characteristics of a fault are decided by several factors, such as throw, heave, slip and the placement of the hanging wall relative to the footwall. The sense of slip is however the most important aspect and can be rephrased as the main sense of movement on either side of a fault plane and thereby defining the type of fault (Figure 3.1). There are three types/groups of faults, dependent on the main sense of movement: Strike-slip, dip-slip and oblique slip faults (Anderson, 2011).

Dip-slip faults

Faults with a vertical sense of slip is referred to as dip-slip fault. These faults can be subdivided into normal (extensional fault) and reverse faults (compressional fault). Extensional faults are associated with extension of the crust and compressional faults with shortening (compressing) of the crust (Figure 3.1) (Anderson, 2011). The other key difference is the relative movement of the hanging wall compared to the footwall. In normal faults the hanging wall moves down compared to the footwall, resulting in graben and horst structures. A more low-angle normal fault is referred to as a detachment fault. With a reverse movement of the hanging wall compared to the footwall the outcome is different and the fault is therefore rightfully named reverse fault. The steepness of the reverse fault exceeds 45° and is categorized as a thrust fault otherwise. When faulting occurs, a weakness in the crust is developed and faults can be reactivated because of this weakness. The reactivated faults can even be opposite of the original fault movement, a normal fault may therefore develop into a reverse fault and the other way around (Anderson, 2011).

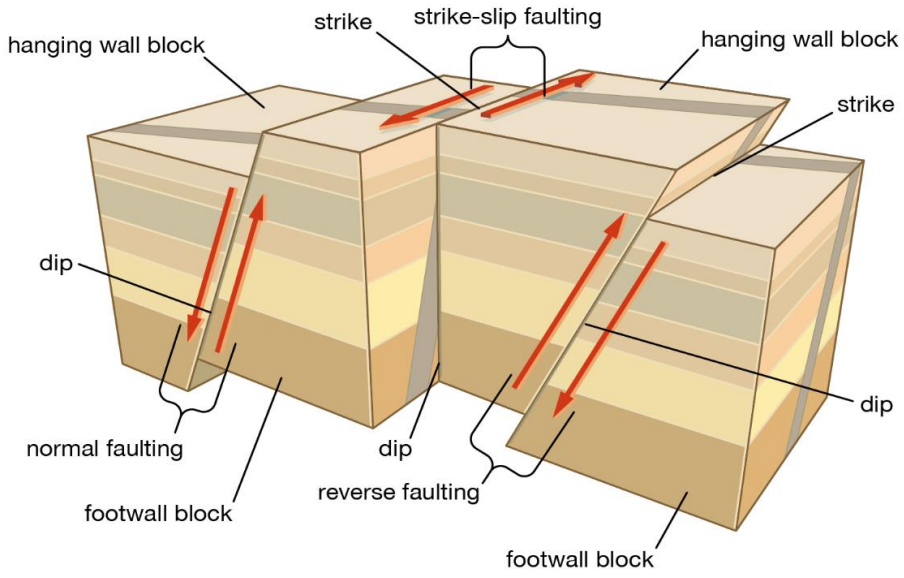

Figure 3.1: Examples of strike-slip and dip-slip faults. Acquired from Britannica.

3.1.2 Salt in association with petroleum

The Nordkapp Basin is strongly influenced by different forms of salt deposits. Salt, and salt features have historically played an important role in geological research, as it is closely related to the world´s biggest oil and gasfields (e.g., North Sea, Gulf of Mexico, Pricaspian Basin, Persian Gulf Campos Basin and Lower Congo Basin (Hudec & Jackson, 2007). The Nordkapp Basin is also quite known for being heavily influenced by tectonics in addition to uplift and erosion (R. Gabrielsen et al., 2013). In the following these factors will be described in relation to potential petroleum system in the Nordkapp Basin.

Petroleum system in salt related basins

Timing of the salt mobilization and diapirism is important in terms of understanding suprasalt reservoirs and source rocks. The salt flow; controls the reservoir distribution, creates structural traps and affects the timing and style of stratigraphic traps. Salt is impermeable because of its low permeability and function as a seal for fluid migration (Hudec & Jackson, 2007). Salt has a high conductivity, affectively 2-3 times higher than sedimentary rocks, which changes the temperature of the suprasalt and subsalt strata. The thermal regime of the suprasalt strata increases, giving it a positive anomaly, whereas strata adjacent or below the salt bodies becomes cooler, resulting in a negative anomaly. The positive suprasalt and negative subsalt can be considered a dipole, but changes into a negative monopole if the salt body reaches the surface (Mello et al., 1995). The thermal maturity of kerogen within source rock are heavily temperature dependent and increase above the salt bodies and the opposite below/adjacent to the salt bodies, expanding the oil/gas window (Cedeño et al., 2019).

3.1.3 Petroleum system in the Nordkapp Basin

The petroleum system in the Nordkapp Basin is often written off as overmature due to the depth of Paleozoic and Mesozoic rocks as a result of salt tectonics in Triassic times (Cedeño et al., 2019). 2D structural restoration done by Cedeño et al., (2019) and Rojo et al., (2019) indicate that salt diapirs piercing through the seafloor during the Triassic, may have halted the maturation process of the source rocks, and deeper prospectivity is therefore plausible. Thermal modeling done by (Cedeño et al., 2019) indicate that the salt diapirs in the Nordkapp Basin have a cooling thermal effect on adjacent and underlying strata, directly linked to the width of the diapir. In the eastern subbasin, an isolated wide salt diapir causes a strong

negative thermal anomaly, effectively making adjacent rocks 70 ◦C colder and even lower temperatures in the subsalt strata, the less wide salt diapir situated within the study area has a far lower thermal effect and lateral extent, but nevertheless an expanding effect on the hydrocarbon generation window (Cedeño et al., 2019). Diapirs more closely stacked like the central basin (Figure 3.5) have a greater lateral thermal effect (Cedeño et al., 2019) compared to greater offsets between each diapir, such as the SE subbasin (Figure 3.5). The movement of the evaporitic sediments is an important element for the petroleum system in the Nordkapp Basin and is responsible for regulating the reservoir distribution in Triassic to Cretaceous (Bugge et al., 2002). The salt affects tectonics (e.g development of structural traps), thermal evolution (e.g. migration and maturation of hydrocarbons) and sedimentation (e.g. development of reservoir and stratigraphic traps). The Cenozoic uplift of the Barents Sea is also an important aspect when evaluating the petroleum potential and may result in expelled oil reserves and gas expanding to double volume, which can result in hydraulic fracturing of the cap rocks (Chand et al., 2008).

3.1.4 Flares

In the last 20 years, gas and gas hydrates have been frequently studied because of; the global impact on the climate change, stability of platform in relation to blowouts and the provided insight into deeper hydrocarbon accumulations (Ostanin et al., 2012). The study area at the flank of the eastern subbasin in the Nordkapp Basin has been affected by several episodes of glaciation, followed by uplift and erosion, which is a common phenomenon in many of the basins situated in the SW Barents Sea (Lasabuda et al., 2018). The result of this is unloading causing reopening of already existing faults in addition to the creation of new ones and working as a conduit for fluid migration, seen as flares in water column data (Figure 3.2) (Chand et al., 2012).

The large sedimentary basins of the epicontinental Barents Sea contains huge amount of hydrocarbon trapped in common petroleum systems and numerous shallow gas and gas hydrate accumulations (Henriksen et al., 2011). Hydrocarbon leakage throughout the SW Barents Sea may indicate a working petroleum system and can be identified as; pockmarks, methane derived carbonate mounds and mud volcanoes, and in the subsurface as vertical seismic chimneys, amplitude anomalies, blow out pipes and paleo-pockmarks (Ostanin et al., 2012). The importance of shallow gas accumulation might provide information of petroleum

systems, as shallow gas accumulations often originates from deeper sources. The gas accumulation itself may also have an economic value if the accumulation is big enough (Vadakkepuliyambatta et al., 2015). Because of the cold temperature in the Barents Sea occurrence of gas hydrates are common. The stability zone of the gas hydrates is dependent on the temperature of the water close to the seafloor, depth of the water column (seabed pressure), gas composition, pore water salinity and geothermal gradient (Andreassen et al., 2017). In some cases, shallow gas accumulations shown in the seismic appears to be leaking, but no evidence of this is registered in water column data.

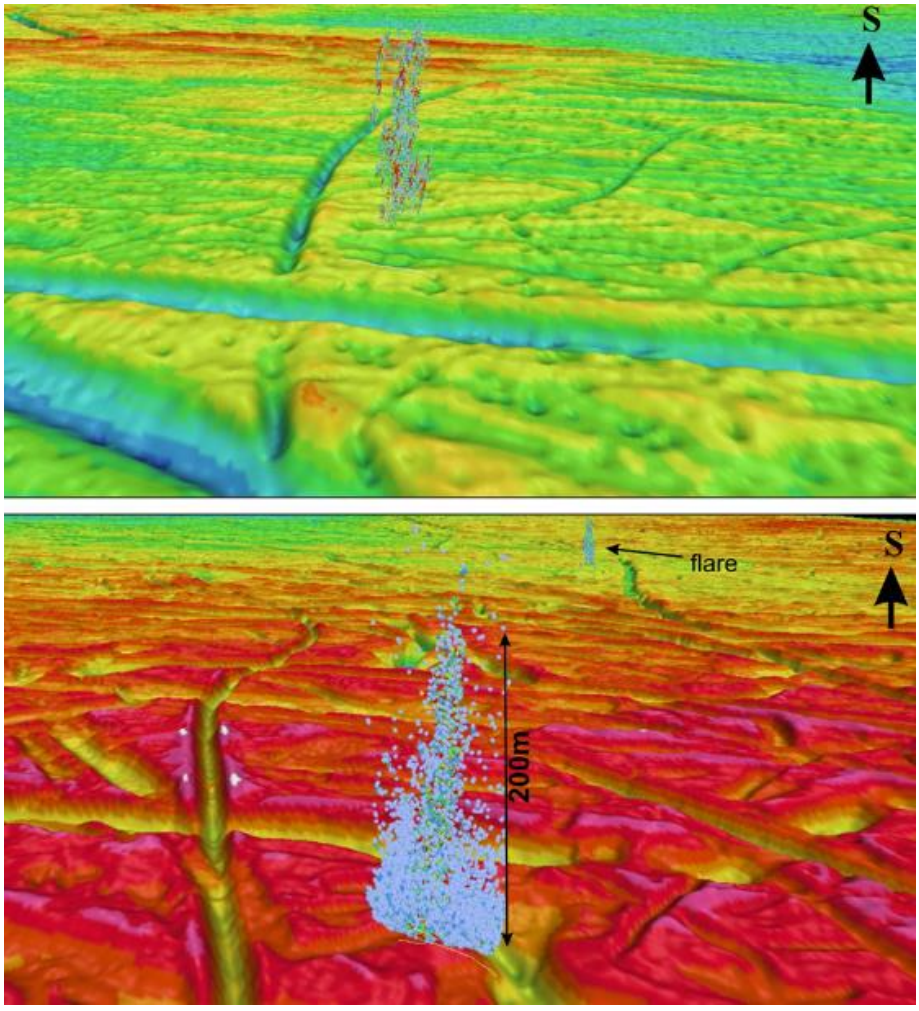

Figure 3.2: Bathymetric maps showing pockmarks, depressions and flares (appearing from plough marks) in the west Barents Sea. Modified from (Chand et al., 2012)

3.1.5 Pockmarks

Pockmarks are circular depressions located at the seafloor, with a typical diameter of 30-40 meters and 3-4 meters deep (Harrington, 1985). These depressions are often associated with silt and clay and can be found in the Barents Sea area (Chand et al., 2012) and the North Sea. There are several theories regarding the formation of pockmarks, the most widely known theory is seabed gas escape from a biogenic or petrogenic source (Harrington, 1985). Another theory is trapped pore water in soft sediments (silt or clay), the pressure increases and is eventually released, forming these circular depressions known as pockmarks(Harrington, 1985). The latter theory is often associated with glaciomarine sediments, where the porewater originates from glaciers (Harrington, 1985).

3.2 Data and Methods

This study will apply seismic 3D data, located at the margin between the Nordkapp Basin and the Fedinsky High in the Barents Sea (Figure 3.5). Exploration well 7435/12-1 (Korpfjell) available through NPD, was used for correlation of the seismic horizons identified in the 3D seismic data by utilizing a composite line composing of NPD1201-003, NPD1201-030 and BA-11-131. Multibeam echosounder water column data acquired by the MAREANO-program and processed in FM Midwater software is used to map potential sites of seabed gas release (gas flares).

3.2.1 Seismic data

The seismic 3D dataset TGS_EUR 15 was acquired in 2015 by TGS. To optimize the crossline coverage, three sources with long offsets (8000 m) were utilized. The data quality is good and ensures fair mapping of the salt diapir, the structural elements, horizons and amplitude anomalies.

Schlumberger´s software package Petrel 2019 was used to interpret the seismic and correlate the seismic horizons to well 7435/12-1 in this study. The software utilizes images of the subsurface generated by a seismic source producing elastic waves (Busby, 2003). These waves are reflected from the interfaces in the subsurface defined as reflectors. The

terminologies widely utilized in the description of seismic wave attributes are phase and polarity. The polarity of a seismic wave is determined by acoustic impedance. The polarity of a seismic wave is determined by acoustic impedance. A positive acoustic impedance contrast is associated to a normal polarity and vice versa, given a polarity standard SEG Sheriff (2006). The acoustic impedance (Z) is dependent on density (ρ) of the sediments and the velocity (V) the seismic wave travels through the unit.

$$Z = \rho V$$

A normal standard polarity gives rise to a high amplitude peak at the seafloor (the seafloor always has a positive acoustic impedance and can therefore be used as a reference), whereas a reverse polarity results in a high amplitude trough at the same boundary. The dataset TGS_EUR15 is set to normal polarity and displays a zero-phase (Figure 3.3A). At normal polarity zero-phase has a characteristic high amplitude central peak, with two minor low amplitude troughs (Figure 3.3A-B). The interface of the unit is placed at the high amplitude peak as opposed to minimum phase where the boundary is located at the wavelet onset (Figure 3.3A). The advantages of seismic interpretation using zero-phase signal is the apparent difference between peak and through between any seismic reflection (Figure 3.3B).

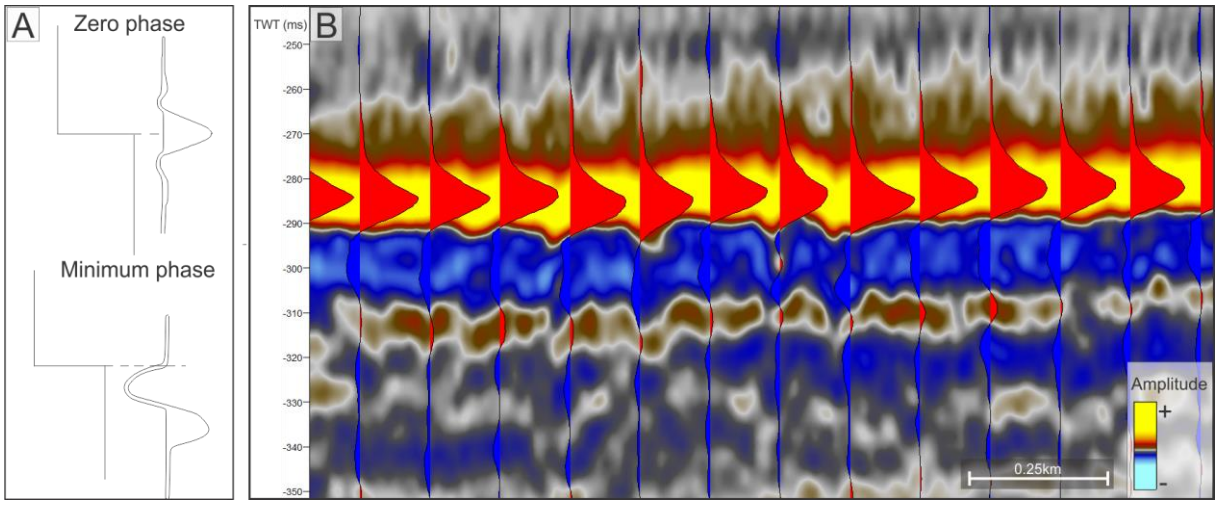

Figure 3.3: A) Simplified model showing the difference between zero and minimum phase. B) The wiggles displayed in the dataset shows zero phase with normal polarity (SEG polarity).

3.2.1.1 Hydrocarbon indicators in seismic data

Bright spots are commonly known as a direct hydrocarbon indicator, other key indicators are flat spots, dim spots and phase reversals (Andreassen et al.,2007a). A bright spot is defined as

a high seismic amplitude anomaly, related to a negative change in density and acoustic velocity, which results in a prominent impedance contrast (Figure 3.4A). Such changes in density and, consequently, acoustic velocity are often observed on a contact between a gas saturated pocket or layer and the surrounding strata (Andreassen et al., 2007). A high amplitude anomaly and bright spot share many similarities but can be distinguished. High amplitude anomaly represents both normal and reverse polarity, whereas bright spots are only associated with negative impedance contrast (Brown, 2004). Strong amplitudes are caused by high acoustic impedance contrast, which could represent the presence of gas in a porous sandstone with overlying shale marking a negative impedance contrast, because the presence of gas drastically decreases the P-wave velocity. It could also represent lithological changes, e.g. shale overlying salt, giving rise to a positive impedance contrast. Bright spots are often associated with faults and chimneys and occur along these structures in addition to above and within reservoirs (Andreassen et al., 2007). The thickness of a gas-saturated layer or pocket has to exceed a certain value to be detectable on the seismic data. In our case, it is 16.25 meters within the reflector represented by K4 and 29.5 meters within K1 assuming a velocity of 1300 m/s for the gas (Andreassen et al., 2007).

Phase reversals are associated with bright spots and are characterized by a phase shift of 180°, which represents a gas-water or gas-oil contact and can potentially result in a flat spot (Figure 3.4B)(Brown, 2004). Flat spots are anomalies which have a characteristic flat contact, unlike the adjacent reflectors, forming a discordant boundary (Figure 3.4B) (Andreassen et al., 2007). The flat contact is due to naturally flat boundaries between stratified fluids of different density, such as water, oil and gas.

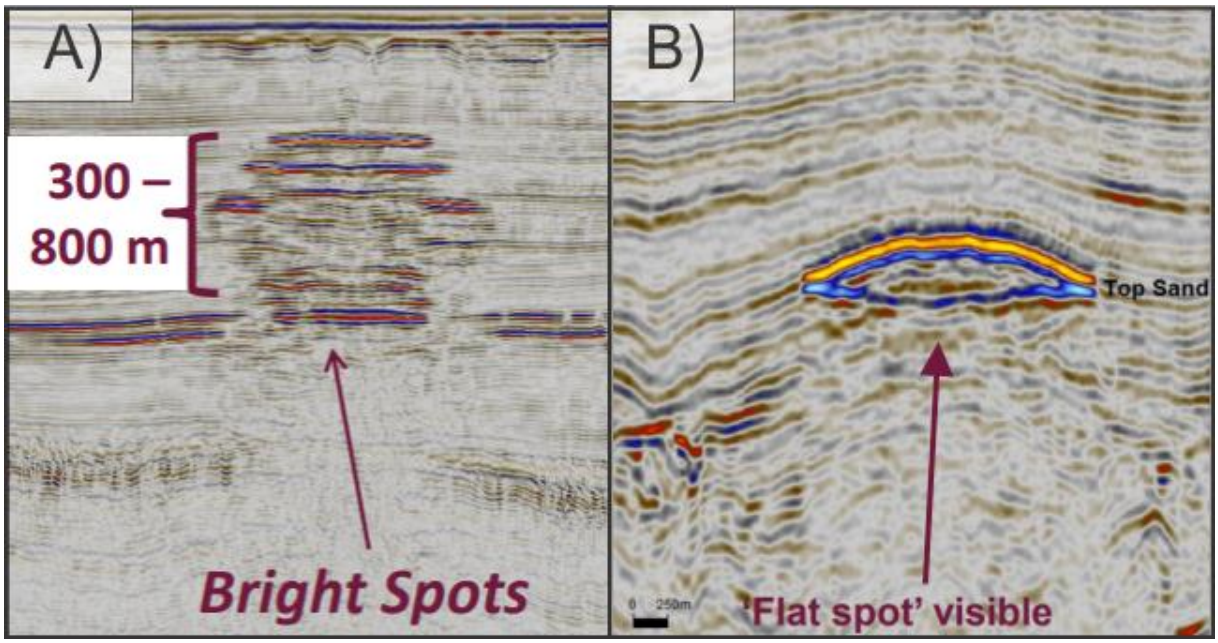

Figure 3.4: A) Displaying bright spots and their characteristic phase reversal (compared to the seafloor). B) Showing the flat contact of a flat spot. Modified from (van den Boogaard & Hoetz, 2015).

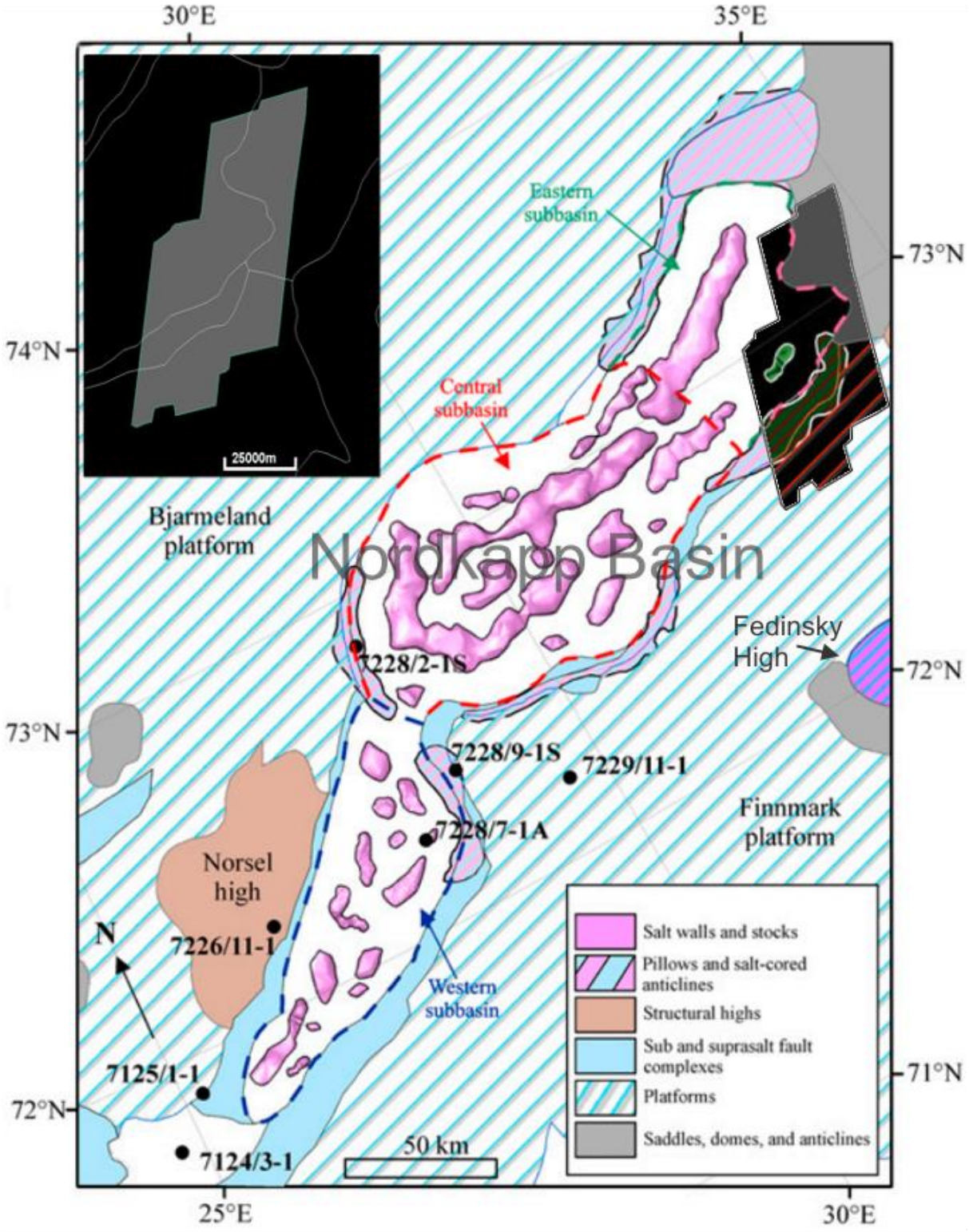

Figure 3.5: Location of the 3D cube (TGS_EUR15 – in black) together with wells adjacent to the study area and the lateral extent of the salt situated within the basin. Structural elements from NPD. (Modified from Rojo et al., 2019)

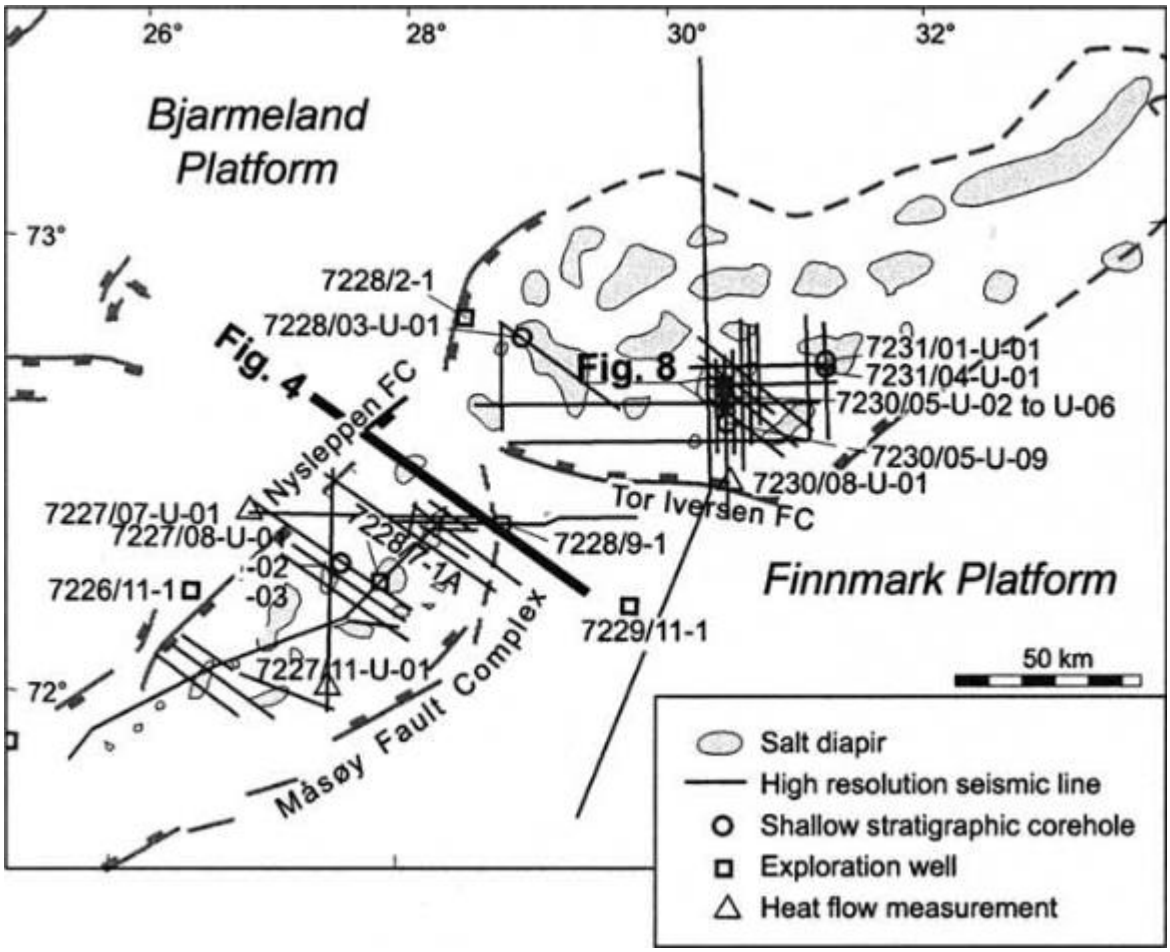

Figure 3.6: Location of shallow stratigraphic boreholes and exploration wells, located in the western and central subbasin (outside the study area), acquired from Bugge et al., 2002.

3.2.2 Seismic resolution

To identify reflectors in the seismic data, the units producing seismic reflections need to have a certain minimum thickness. Vertical and horizontal resolution of the seismic data has been calculated in order to find the minimum dimensions of a unit that could possibly be seen on the seismic data.

3.2.2.1 Vertical resolution

Vertical resolution (Vr) determines the minimum vertical thickness of a reflector detectable by the seismic method, given by equation:

$$Vr = \lambda/4$$

In order to calculate the wavelength (λ), the frequency (F) and velocity (v) is required:

$$\lambda = v/F$$

The velocity values of intra Cretaceous were based on Bugge et al. (2002), whereas the Jurassic and Triassic values were based on well 7435/12-1 (Figure 3.8).

The frequencies of each horizon were acquired in Petrel 2019, shown in table 3.1. The frequencies were picked based on the peak of each frequency representing the lower parts of the spectrum. Higher frequencies is also present in the study area.

3.2.2.2 Horizontal resolution

Horizontal resolution is defined by the radius of the Fresnel zone, which is the ability to discern two lateral features from one another. Features at the subsurface will only be visible if the radius of the Fresnel zone surpasses the lateral extent of the feature. The unmigrated Fresnel zone can be calculated by the following equation:

$$rf = v/2(t/f)^{0.5}$$

rf = radius of the Fresnel zone

v = velocity

f = frequency

t = two-way travel time (in seconds)

The results of the calculations are shown in Table 3.1.

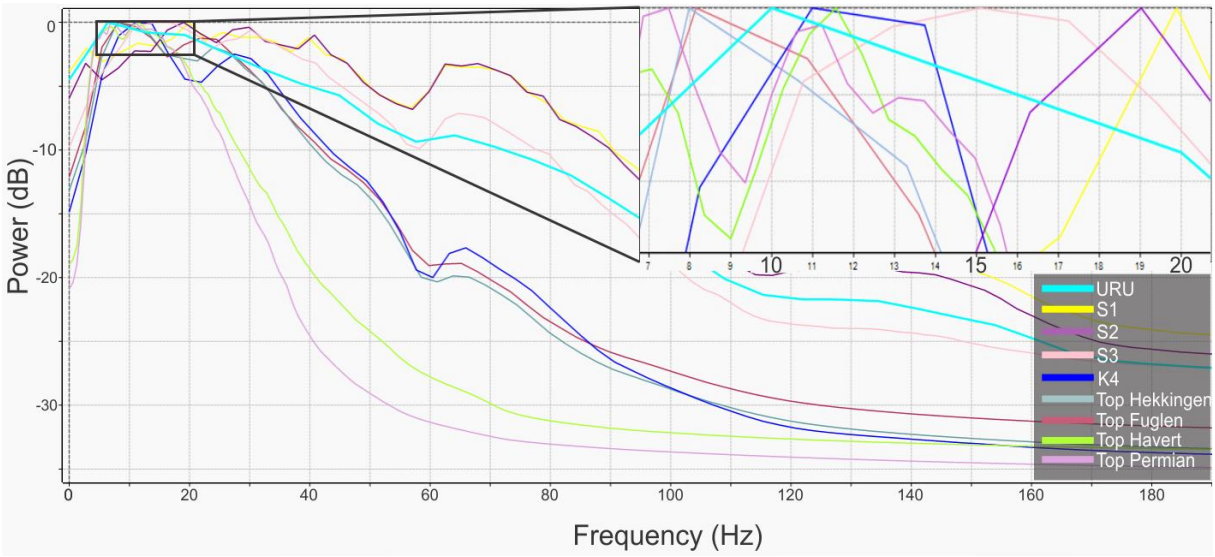

Figure 3.7: Frequency spectra of the different horizons interpreted in this study, peak frequencies were picked for the calculation of vertical and horizontal resolution.

Table 3.1: Displaying the calculated vertical and horizontal resolution for the TGS_EUR15 dataset.

Horizon	Velocity (m/s)	Frequency (Hz)	Wavelength (m)	Vertical resolution (m)	Horizontal resolution (m)
URU	1500	10	163	40	156
K1	2000	20	100	25	158
K2	2250	19	118	30	271
K3	2400	15	160	40	245
K4	2500	11	227	57	337
Top Hekkingen	2550	8	319	80	456
Top Fuglen	2650	8.2	323	81	485
Top Havert	4370	11.6	378	94	931

Top Permian	5260	7.4	7010	178	1701

The results presented in table 3.1, shows a general trend of decreasing vertical and horizontal resolution with depth, vertical resolution of the URU being the exception.

Table 3.2: Showing the characteristics of the wells closest to the study area (Figure 3.5).

Well	Completed date	Operator	Oldest penetrated age	Total depth (in meters)	Result	Distance from study area (in km)
7124/3-1	20.10.1987	Saga Petroleum ASA	Late Carboniferous	4730.0 m	Minor gas and oil discovery (named Bamse), non-commercial	29.5 km
7226/11-1	11.04.1988	Den norske stats oljeselskap a.s	Pre-Devonian	5200.0 m	Gas discovery, non-commercial	21 km
7125/1-1	30.12.1988	Saga Petroleum ASA	MIDDLE TRIASSIC	2200.0 m	Minor oil and gas discovery (named Binne), non-commercial	26 km
7228/2-1S	20.12.1989	Mobil Development Norway AS	EARLY TRIASSIC	4300.0 m	Dry well with minor shows	14 km
7228/9-1S	07.05.1990	Norsk Hydro Produksjon AS	EARLY PERMIAN	4600.0 m	Dry well with minor shows	13km

7229/11-1	15.12.1993	A/S Norske Shell	LATE CARBONIFEROUS	4630.0 m	Dry	11 km
7228/7-1A	02.02.2001	Den norske stats oljeselskap a.s	EARLY TRIASSIC	2881.0 m	Oil and gas discovery, non-commercial	15.5 km
7435/12-1	01.09.2017	Statoil	MIDDLE TRIASSIC	1540.0 m	Gas discovery	9 km

3.2.3 Well Data

Well 7435/12-1 was utilized for the well correlation of the seismic stratigraphy in this study (Figure 3.8). Main characteristics of this borehole and boreholes 7124/3-1, 7226/11-1, 7125/1-1, 7228/2-1S, 7228/9-1S, 7229/11-1 and 7228/7-1A (Figure 3.5) adjacent to the study area are shown in table 3.2. These boreholes have been used to get a better understanding of the depositional environment and petroleum system in and adjacent to the Nordkapp Basin. Source rocks, reservoir rocks, sealing potential and the presence of hydrocarbons in the study area was largely based on the combination of the wells in table 3.2 and Bugge et al.,2002, due to the absence of boreholes within the area.

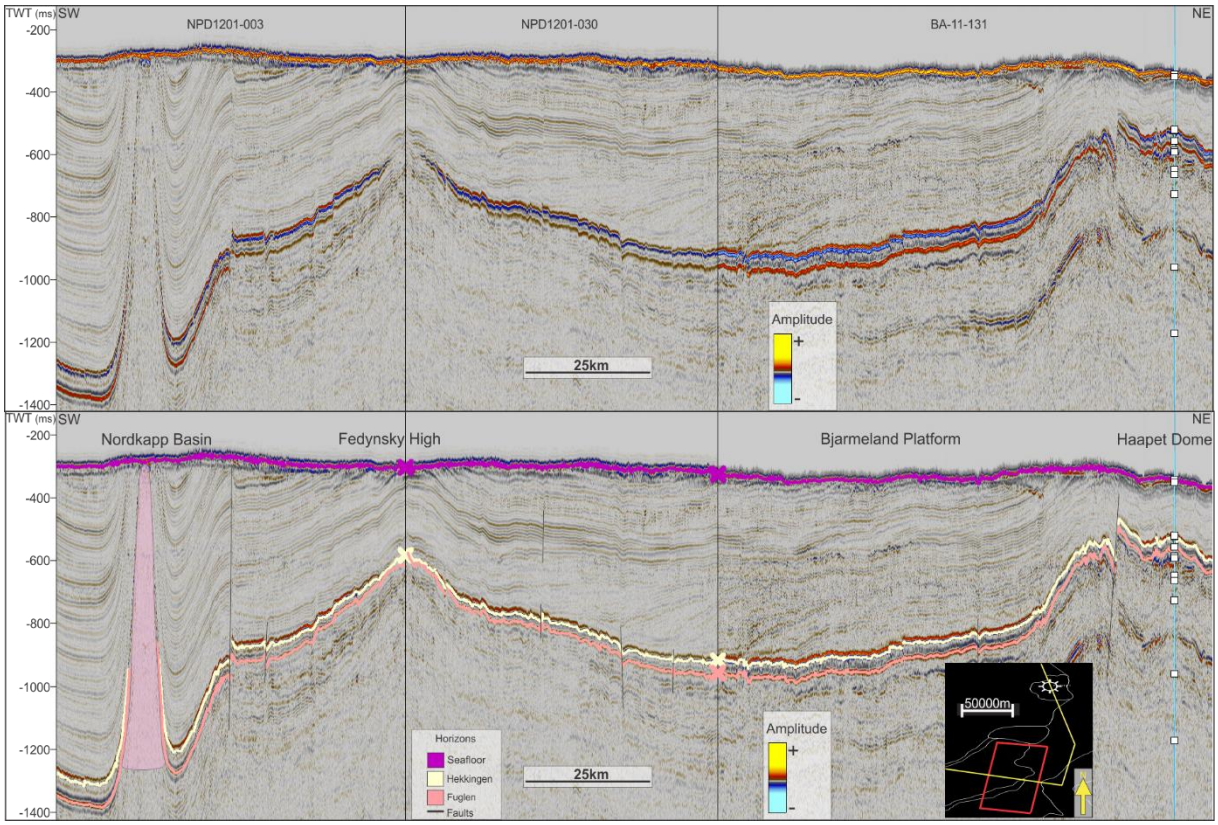

Figure 3.8: Regional composed seismic 2D-profle extending from the Nordkapp Basin to the Haapet Dome. Well 7435/12-1 is located NE of the NB, within the Haapet Dome. A) Uninterpreted. B) Interpreted.

3.2.4 Water column data

Two software's were used to identify and visualise potential gas flares in the multibeam echosounder water column data: FM Midwater and Fledermaus. In addition, Dmagic softwarere was used to process multibeam seafloor data to get high-resolution 3D seafloor models for selected areas.

3.2.4.1 FM Midwater

FM Midwater by QPS is a software used to interpret and process water-column echosounder data. Gas flares are interpreted based on the strong amplitude of the flares compared to that of the adjacent water mass. In volumetric multibeam water column data, a gas flare typically has

a shape of a candle flame, which is usually different to backscatter signal produced by fish, plankton, whales, etc. Moreover, a gas flare typically has a connection to the seafloor.

Hydroacoustic water column data was added to include a new dimension to the study and was acquired by the MAREANO-program in June 2012. The unprocessed data were imported to FM Midwater as navigation and seafloor bathymetry files (.all files) and water column data (.wcd files). Wcd files and navigation files were converted into 3868 .gwc files in order to interpret the water column data in FM Midwater (Figure 3.9). The high number of lines gives detailed information, on possible leakage. The density of lines ensures 100% coverage of the seafloor. Potential flares were identified, extracted and imported in Petrel 2019 to find spatial relation with bright spots, faults, truncations, etc.

Several factors make the identification of gas flares complicated; a) high ambient noise. B) Irregular or strong currents. c) High concentration of plankton. d) Fish schools. e) Unideal multibeam swath of the gas flares, resulting in only partial coverage of the flare.

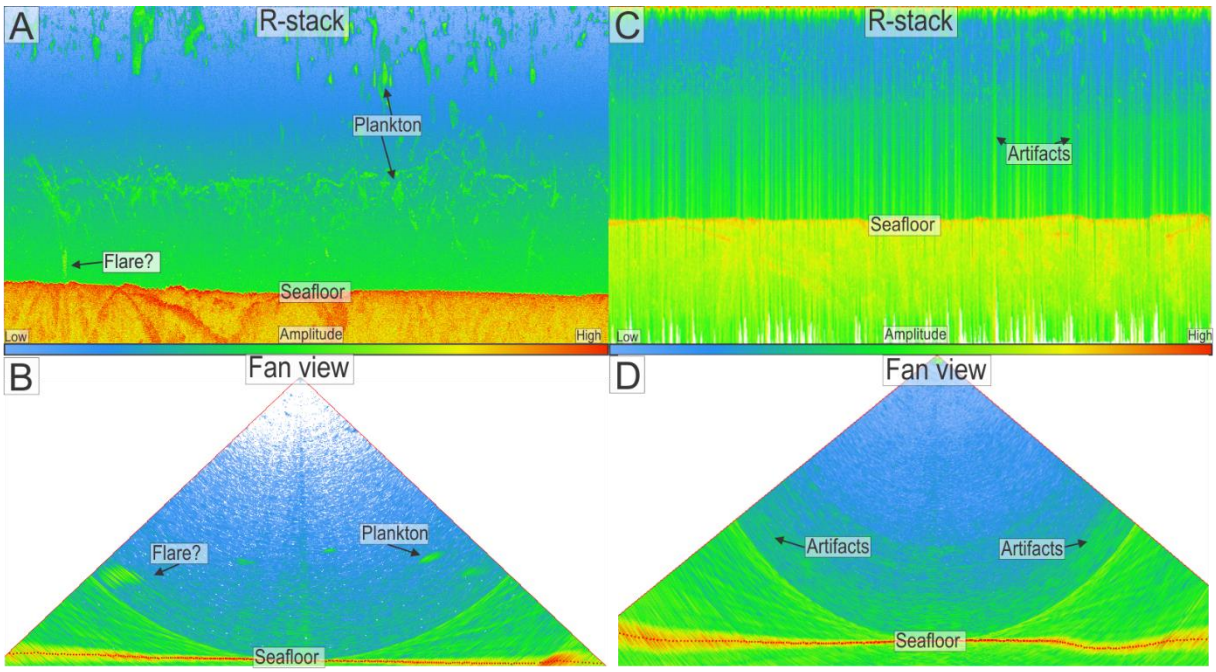

Figure 3.9: The figures show two examples in R-stack view and fan view, example 1 (A-B) shows a typical line, whereas example two (C-D) displays a noisy line with multiple artifacts. A) The R-stack view of the water column data displays irregular shaped anomalies (plankton or other marine organisms) throughout the water column and a linear shaped anomaly connected to the seafloor. B) Fan view of the water column data, showing the same linear shaped anomaly as mentioned in A) and other irregular anomalies. C) R-stack view of the water column, the straight lines shown throughout the water column are errors. D) Fan view of the same errors explained in C).

Artifacts on multibeam water column data:

Noise in the water column data makes it difficult to identify real objects, e.g. gas flares (Figure 3.9C). The artifacts can be related to acquisition errors, caused by stormy weather, interference with another equipment, such as a subbottom profiler or a single beam echosounder (Siwabessy et al., 2018). These abnormal data can be difficult to interpret because they may contain and signals somewhat similar to gas flares or mask the entire water column (Siwabessy et al., 2018) as displayed above.

3.2.4.2 Dmagic

Dmagic is a software that is generally utilized to visualize and process seafloor multibeam data. Navigation and seafloor data files (.all files) of the lines with potential flares were imported in D-magic and processed, in order to obtain the morphology of the seafloor, which was later visualized in Fledermaus together with gas flares extracted from the bulk volume of the water column data.

3.2.4.3 Fledermaus

This software can be used to visualize all types of gridded and ungridded data in both 3D and 4D. Navigation and seafloor data files processed in D-magic were exported in a common ascii format, imported in Fledermaus and converted into detailed bathymetric maps of the seafloor. A spectra of analysis tools allows for a thorough and detailed interpretation of the seafloor, with a resolution of 1x1 meter. Outcrops of the potential flares from FM Midwater were imported into Fledermaus together with the bathymetric maps of the seafloor.

4 Results

This chapter provides an overview of the interpreted horizons (Figure 4.1), sequences and faults followed by an overview of the shallow anomalies of the intra Cretaceous. Furthermore, the relationship between deep and shallow anomalies and the correlation between gas flares, shallow anomalies and underlying structures is also presented in this chapter.

The horizons are introduced in chronological order, starting with the Triassic (Top Havert and near Top-Permian), followed by Jurrassic horizons (Top Hekkingen and Top Fuglen) and Intra Cretaceous (Represented by K1-K4). Triassic and Jurassic horizons are explored to gain a better understanding of a potential petroleum system. The Intra Cretaceous reflectors, and associated shallow anomalies, are the main focus of this study. Well 7435/12-1 is used as a reference to correctly interpret the horizons representing Top Fuglen- and Top Hekkingen (Figure 3.8). Thus, six sequences are described and introduced from oldest to youngest.

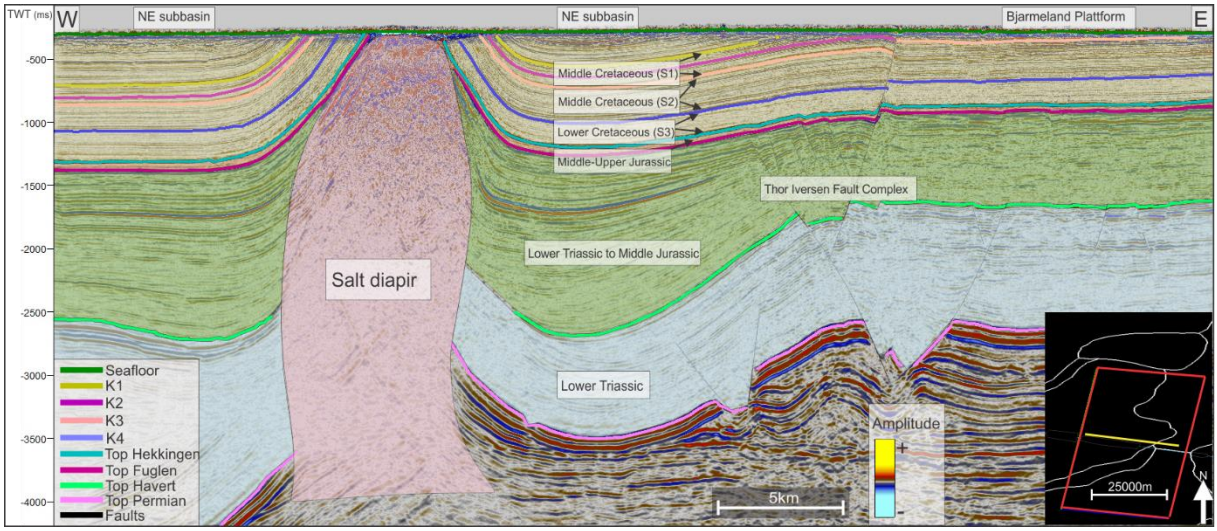

Figure 4.1: An overview of the interpreted horizons from Lower Triassic to Cretaceous. Structural elements from NPD.

4.1 Seismic Horizons

Top Permian horizon

The horizon representing the top Permian Formation has a reflection with amplitudes ranging from medium to medium-high, with a semi-continous character. The transition from the overlying Triassic units to the underlying Permian units below, give rise to a positive reflection coeficent.

The deepest areas shown in the time-structure map of the top Permian horizon are observed in the Nordkapp Basin (Figure 4.2A), along the western flank of the salt diapir, at a depth of

4400 ms (TWT). Shallowing towards the Bjarmeland Platform and the Finnmark Platform in the east, the shallowest areas are located towards the Fedinsky High in the east (2200 ms TWT).

Top Permian Formation is the interpreted unit most influenced by faulting in the study area, espescially along the Thor Iversen Fault Complex (TIFC). The throw ranges from 100-200 ms (TWT) in the southern parts of the complex and from 150-450 ms (TWT) in the northern parts (Figure 4.2A). The largest throw (450 ms TWT) is observed at the northern flanks of the Nordkapp Basin. The orientaition of the faults along the TIFC have a SW-NE strike in the southernmost parts, transitioning to S-N further north of the fault complex (Figure 4.2A).

Top Havert horizon

The top of the Havert Formation has a medium-high reflection, giving rise to a positive reflection coeficient. The contiuity is generally semi-continous.

An isochron map for the top Havert horizon (Figure 4.2B) shows a dip to the west / northwest and a shallowing towards the Fedinsky High. The deepest areas are located north / northwest in the Nordkapp Basin (NB) with depths of 3200 ms (TWT).

The top Havert horizon is heavily faulted along the TIFC. The throw of the faults ranges from about 400 ms (TWT) in the northern to middle parts and 150 ms (TWT) in the southern parts (Figure 4.2B). The orientaition of the fault along the TIFC has a SW-NE strike in the southernmost parts, transitioning to S-N further north of the fault complex.

Top Fuglen horizon

The reflection representing top Fuglen Formation displays a very high amplitude and high contunuity in the study area. Corellated to well 7435/12-1 (Figure 3.8), the boundary between the Fuglen Formation below and Hekkingen above, give rise to a positive reflection coefficient.

An isochron map of the horizon is introduced in Figure 4.2C. The shallowest parts of the horizon is observed south on the Finnmark Plattform (FP) at a depth of 700 ms (TWT), whereas the deepest part is located in the Nordkapp Basin, along the northwestern flank of the salt diapir (1400 ms TWT).

The top Fuglen is influenced by faulting along the Thor Iversen Fault Complex (TIFC). The throw varies from 40 to 100 ms (TWT), and reaches the highest values in the northern (100ms TWT) and middle parts (50 ms TWT) of the study area. The orientaition of the fault along the TIFC has a SW-NE strike in the southernmost parts, transitioning to S-N further north of the fault complex.

Top Hekkingen horizon (Base Cretaceous Unconformety)

The top Hekkingen Formation (BCU) is represented by a reflection showing a very high amplitude and high contunuity throughout the study area. By correlating to well 7435/12-1 (Figure 3.8), the boundary between the Hekkingen Formation below and Cretaceous strata above is identified showing a negative reflection coefficient.

An isochron map of the horizon is introduced in Figure 4.2D, showing that the shallowest parts of the horizon are located towards the Fedinsky High, at about 900 ms TWT. The deepest parts of the horizon are observed in the Nordkapp Basin, along the northwestern flank of the salt diapir (Figure 4.2D) at a depth of 1350 ms (TWT).

The top Hekkingen Formation / BCU is influenced by faulting along the Thor Iversen Fault Complex. The throw is the largest in the northern (120 ms TWT) and middle parts (80 ms TWT) of the TIFC (Figure 4.2D). The orientaition of the fault along the TIFC has a SW-NE strike in the southernmost parts, transitioning to S-N further north of the fault complex.

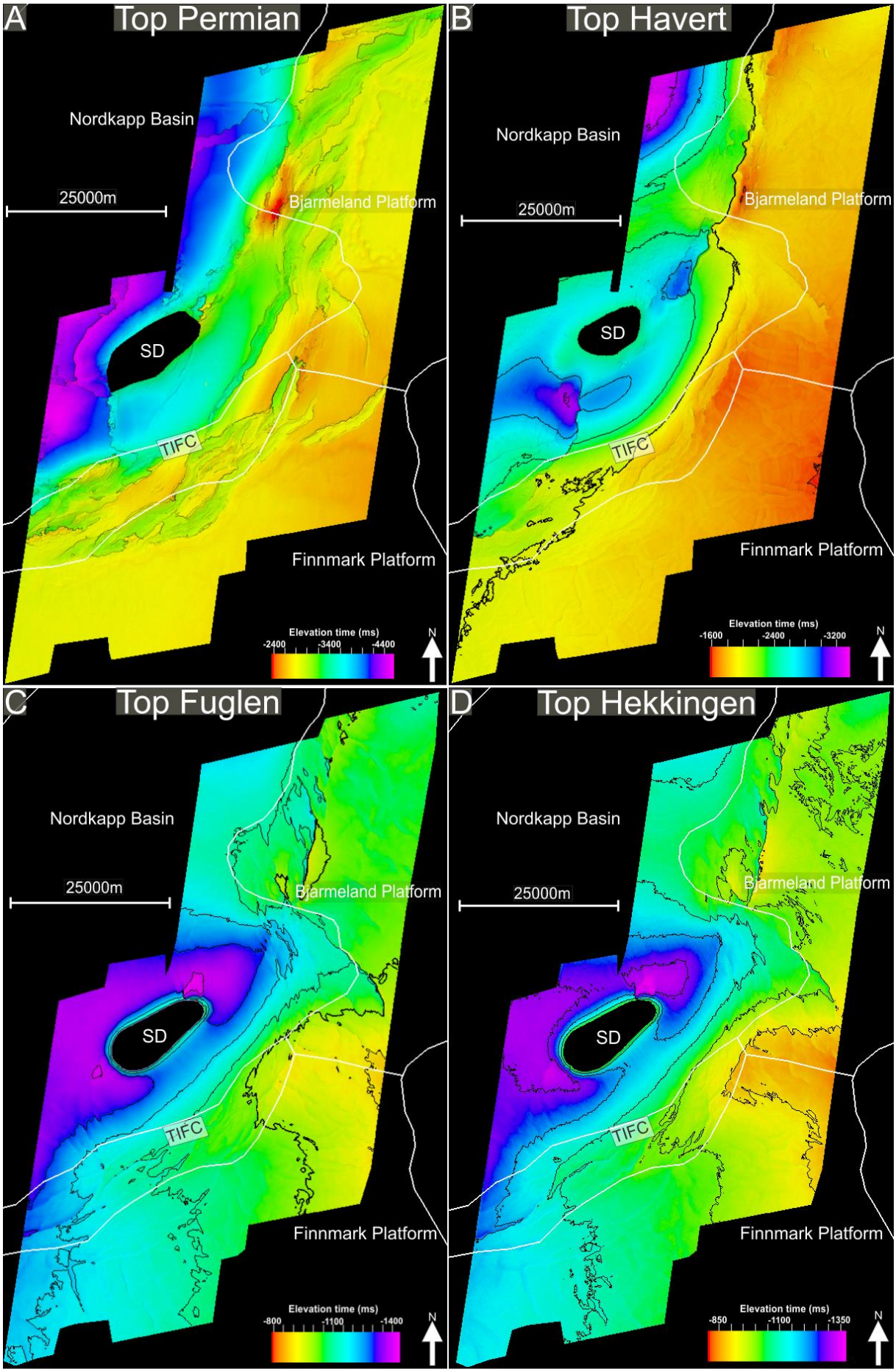
A
Top Permian
Nordkapp Basin
25000m
Bjarmeland Platform
SD
TIFC
Finnmark Platform
Elevation time (ms)
-2400
-3400
-4400
N
B
Top Havert
Nordkapp Basin
25000m
Bjarmeland Platform
SD
TIFC
Finnmark Platform
Elevation time (ms)
-1600
-2400
-3200
N
C
Top Fuglen
Nordkapp Basin
25000m
Bjarmeland Platform
SD
TIFC
Finnmark Platform
Elevation time (ms)
-800
-1100
-1400
N
D
Top Hekkingen
Nordkapp Basin
25000m
Bjarmeland Platform
SD
TIFC
Finnmark Platform
Elevation time (ms)
-850
-1100
-1350
N

Figure 4.2: A) Isochron map of the top Permian Formation, depth displayed in TWT (ms). B) Isochron map of the top Havert Formation, depth displayed in TWT (ms). Contour lines are set to 300ms intervals. C) Isochron map of the top Fuglen Formation, depth displayed in TWT (ms). Contour lines are set to 100 ms intervals. D) Isochron map of the top Hekkingen Formation (BCU), depth displayed in TWT (ms). Contour lines are set to 100 ms intervals. ABCD) TIFC=Thor Iversen Fault Complex. SD=Salt diapir. Structural elements from NPD.

Intra Cretaceous horizons

K1 horizon

The K1 horizon is represented by a reflection with medium-high amplitude throughout the study area. The K1 horizon corresponds to K1 (see Heiberg (2018) and Marin et al., 2017)) and represents the top of Cretaceous sequence S1 and the base of sequence S2, giving rise to a negative reflection coefficient, with a high to semi-high continuity.

An isochron map of the horizon is shown in Figure 4.3A. The horizon is generally shallowing from west to east, with the shallowest parts towards the tip of the Fedinsky High (670 ms TWT). The deepest parts ranges from the western parts of the FP to the western parts of the NB (1150 ms TWT).

The K1 formation is influenced by faulting along the Thor Iversen Fault Complex. The fault complex, which stretches north to south has a throw ranging from 20 to 100 ms (TWT). The greatest throw (100ms) is observed towards the Fedinsky High and the northern parts of the complex. The orientaition of the fault along the TIFC has a SW-NE strike in the southernmost parts, transitioning to S-N further north of the fault complex.

Structure A is marked in figure 4.3A as a structural high associated with faults, located along the Thor Iversen Fault Complex in the north between the Bjarmeland Plattform and the Nordkapp Basin (Figure 4.3A). The structural high is among the shallowest parts of the K1 horizon at a depth of 700 ms (TWT). The two main faults within the structure have a NW-SE orientation and can be categorized as F1 (towards the SW, 5.5 km in length) and F2 (towards the NE, 9 km in length). The shallowest parts within structure A is located along the axis of F1 and F2, becoming deeper perpendicularly to the faults, representing a slight doming.

K2 horizon

The K2 horizon is represented by a reflection with a medium to high amplitude throughout the study area. The K2 herein is correlative to the K2 of Heiberg (2018) and Marin et al., (2017), and represents the top of seismic sequence 2 and base of S3 (S3 corresponds to S4 (Figure 5.1), Heiberg (2018) and Marin et al., (2017) giving rise to a negative reflection coefficient.

An isochron map of the horizon is shown in Figure 4.3B, displaying that the deepest parts of the horizon is located southwest of the salt diapir in the Nordkapp Basin at a depth of 900 ms (TWT). The shallowest parts of the horizon are located at the boundary between the Bjarmeland Platform and the Finnmark Platform in the southeast (330 ms TWT), towards the Fedinsky High.

The K2 is influenced by faulting along the Thor Iversen Fault Complex (TIFC). The throw of the fault complex ranges from 10-80 ms TWT and is largest in southern (60 ms TWT) and northern margins (80 ms TWT). The orientaition of the fault along the TIFC has a SW-NE strike in the southernmost parts, transitioning to S-N further north of the fault complex.

Structure A can also be observed at the K2 horizon (Figure 4.3B), with the same trends as explained above. The only difference is the slight doming is less apparent and F1 and F2 is observed at a depth of 425 ms (TWT).

An elongated structure (Figure 4.3B) is located along the TIFC at the trippel junction between the Nordkapp Basin, Bjarmeland and Finnmarks Plattform, at a depth of 425 ms (TWT) and will be referred to as structure B. The orientation of the structure is S-N and has a length of approximately 3km (this structure will be further described in subchapter 4.5.3 (Figure 4.16-18).

To the north/northwest the horizon mirrors a circular shaped structure with a diameter of 3.6 km, located in the middle of the boundary between the Bjarmeland platform and the Nordkapp Basin at a depth of 550 ms (TWT) and will be referred to as Structure C (Figure 4.3B). Profile 4 and 5 (Figure 4.15) indicate that faults are likely the cause of this circular shape.

K3 horizon

The reflection that marks the K3 horizon has a high amplitude in the southern part of the study area and a medium amplitude in the north, with a continuity following the same trend and a negative reflection coefficient.

An isochron map for the horizon is introduced in figure 4.3C, displaying the deepest parts are observed along the northern, western and southern flanks of the salt diapir within the Nordkapp Basin, at a depth of 850 ms (TWT). The shallowest parts are located to the east where the horizon is truncated by the URU, and on the Bjarmeland Platform in the northeast (350 ms TWT).

The K3 is influenced by faulting along the TIFC stretching north to south in the study area. The displacement along the fault complex is ranging from 10 to 150 ms (TWT) and is at its greatest towards the north in the study area. The orientaition of the fault along the TIFC has a SW-NE strike in the southernmost parts, transitioning to S-N further north of the fault complex.

Figure 4.3 C displays the outline of structure A, which has the same trend as explained above. F1 and F2 represents the shallowest parts of the structure at a depth of 360-400 ms (TWT).

Structure C is also observed in the K3 horizon, with an increase in diameter to 4.5 km, located in the middle of the boundary between the Bjarmeland platform and the Nordkapp Basin at a depth of 450 ms (TWT) (Figure 4.3 C)

K4 horizon

The K4 horizon is represented by a reflection characterized by a medium to high amplitude, with highest amplitudes in the southern to middle parts and medium amplitude in the north. The continuity of the horizon varies from low to semi-continuous in the northern and eastern parts, with increasing continuity towards the southwest. The K4 horizon corresponds to K4 (see Vegard Heiberg (2018) and Marin et al., (2017) and indicates the top of the S3 seismic sequence (S3 corresponds to S4, Vegard Heiberg (2018) and Marin et al., (2017)) giving rise to a positive reflection coefficient.

An isochron map of the horizon is displayed in figure 4.3D, indicating that the deepest parts of the horizon are in the Nordkapp Basin (NB), at the western flank of the salt diapir (750 ms

TWT). The horizon is at its deepest in the west of the NB (800 ms TWT) gradually shallowing towards the east at a depth of 350 ms (TWT). The polygon in the east (Figure 4.3D), indicates where the horizon is truncated by the upper regional unconformity (URU)/seabed. The shallowest parts of the horizon are located along the the Bjarmeland Platform (BP) (300 ms TWT).

The K4 horizon is influenced by faulting along the Thor Iversen Fault Complex (Figure 4.10C), stretching north to south. The throw of the faults is ranging from 10 to 80 ms (TWT) and is the largest towards the north (Figure 4.3D. The orientaition of the fault along the TIFC has a SW-NE strike in the southernmost parts, transitioning to S-N further north of the fault complex.

Structure C is not present in K4, marking the vertical extent of the structure.

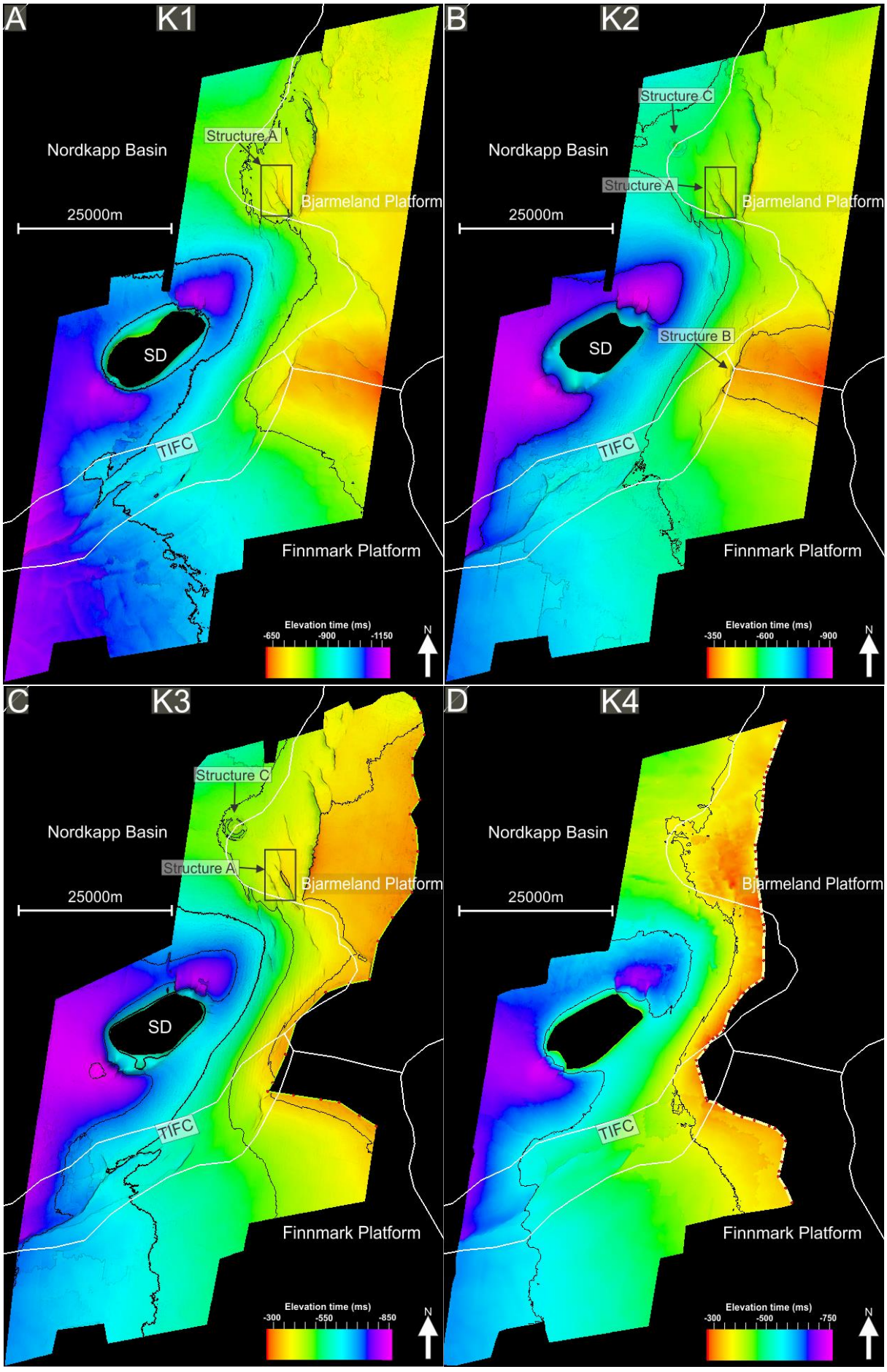
A
K1
Nordkapp Basin
Structure A
Bjarmeland Platform
25000m
SD
TIFC
Finnmark Platform
Elevation time (ms)
-650
-900
-1150
N
B
K2
Structure C
Nordkapp Basin
Structure A
Bjarmeland Platform
25000m
Structure B
SD
TIFC
Finnmark Platform
Elevation time (ms)
-350
-600
-900
N
C
K3
Structure C
Nordkapp Basin
Structure A
Bjarmeland Platform
25000m
SD
TIFC
Finnmark Platform
Elevation time (ms)
-300
-550
-850
N
D
K4
Nordkapp Basin
Bjarmeland Platform
25000m
TIFC
Finnmark Platform
Elevation time (ms)
-300
-500
-750
N

Figure 4.3: A) Isochron map of the K1 horizon and structure A, depth displayed in TWT (ms). Contour lines are set to 200 ms intervals. B) Isochron map of the K2 horizon and structure A, B, C, depth displayed in TWT (ms). A circular structure can be observed northwest on the horizon between the boundary between the Nordkapp and Bjarmeland Plattform. An elongated structure is also observable at the trippel junction between the Nordkapp Basin, Bjarmeland and Finnmark Plattform. Contour lines are set to 200 ms intervals. C) Isochron map of the K3 horizon and structure A,C, depth displayed in TWT (ms). The polygon (green line with red dots) marks where the reflector is truncated by the URU to the east. A circular shaped structure can be located north/northwest on the horizon, between the Nordkapp Basin and the Bjarmeland Plattform. Contour lines are set to 120 ms intervals. D) Isochron map of the K4 horizon, depth displayed in TWT (ms). The polygon (yellow line with red dots on c and d) marks where the reflector truncates towards the URU. Contour lines are set to 200 ms intervals. ABCD) Structural elements from NPD. TIFC=Thor Iversen Fault Complex. SD=Salt diapir

Upper regional unconformity (URU)

The URU is represented by a reflection with a high amplitude and is only locally present in the study area. The URU was interpreted on a peak and has a positive reflection coefficient. The URU horizon (Figure 4.4A) is mapped mainly on the Finnmark and Bjarmeland Plattform where it often tends to truncate towards the seafloor displaying the discontinuity of the reflector (Figure 4.4A).

The isochron map presented in Figure 4.4A, has a maximum depth of 440 ms (TWT) located in the western part of the Finnmark Platform, and the shallowest parts are located to the northeast on the Finnmark Plattfom (330 ms TWT).

There are no indications of faulting influencing the URU.

Seabed

The reflection representing the seabed was interpreted on a high amplitude peak with a positive reflection coefficient, and with a very high continuity.

An isochron map of the Seabed is presented in Figure 4.4B, showing that the shallowest parts are to the south (300 ms TWT). The deepest parts of the horizon are located at the southern part of the Finnmark Platform at a depth of 420 ms (TWT).

The horizon is characterized by a number of elongated depressions (Figure 4.4B), ranging from 2 to 20 km in length and reaching tens of meters in width.

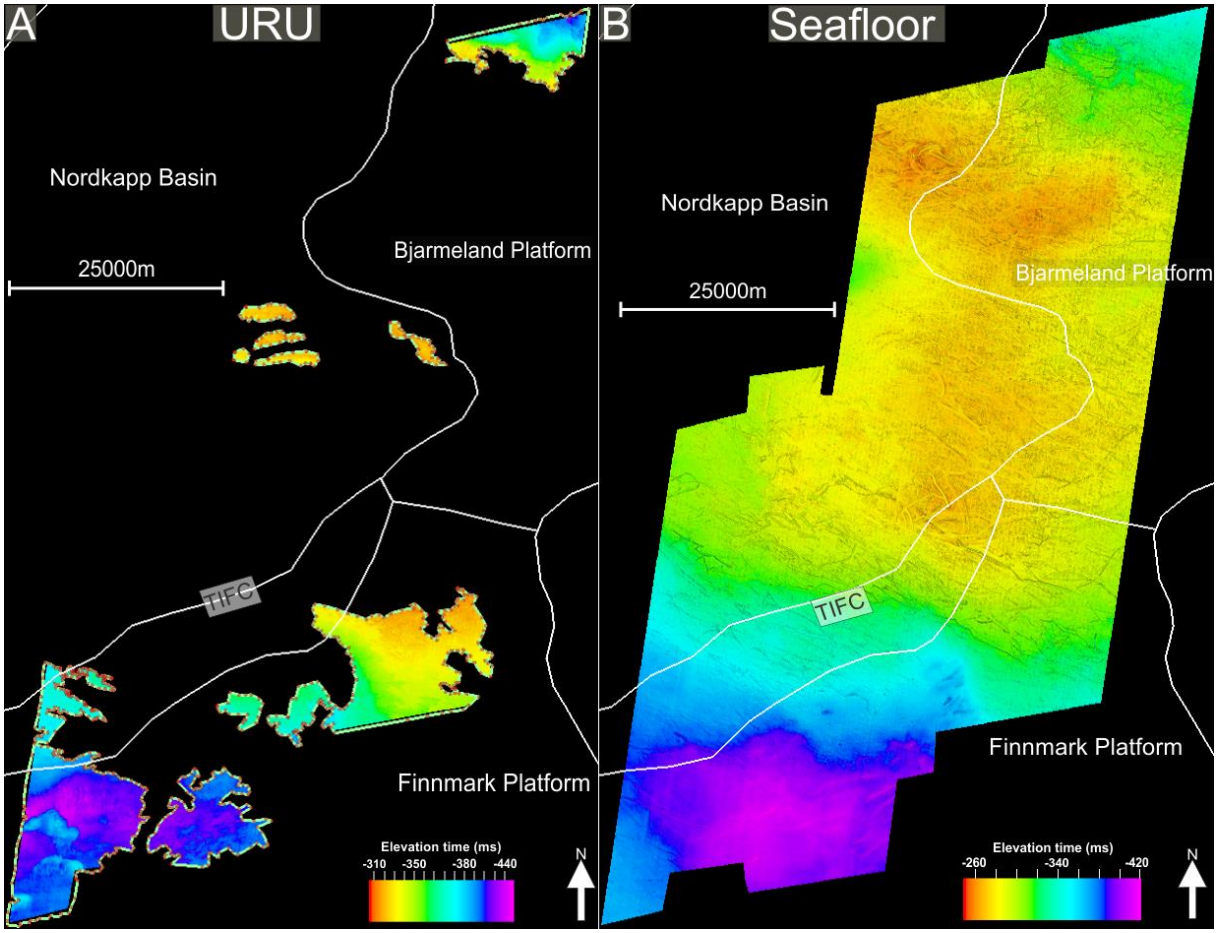

Figure 4.4: A) Isochron map of the URU, depth displayed in TWT (ms). Note that only a fraction of the study area is mapped due to patchy distribution of URU. B) Isochron map of the Seafloor, depth displayed in TWT (ms). AB) TIFC=Thor Iversen Fault Complex. Structural elements from NPD.

4.2 Seismic Units

Lower Triassic

The Lower Triassic unit is bounded by the top Havert horizon above and top Permian below. The thickness of the Lower Triassic unit varies throughout the study area, where both the thinnest and thickest areas are observed in the Nordkapp Basin (NB, Figure 4.5A). The thickest areas in the unit lie northwest of the salt diapir and reach a thickness of 2000 ms

(TWT), while the thinnest area is located northwest of the diapir toward the Bjarmeland Plattform (BP) and shows a thickness of only 250 ms (TWT).

The maximum thickness variation is observed along the Thor Iversen Fault Complex (TIFC) at 450 ms (TWT). The major fault north of the TIFC has a maximum thickness variation of 550 ms (TWT) along the fault (Figure 4.5A). The orientaition of the fault along the TIFC has a SW-NE strike in the southernmost parts, transitioning to S-N further north of the fault complex.

Middle Triassic to Middle Jurassic

The Middle Triassic – Middle Jurassic unit, delimited by the top Fuglen horizon above and top Havert Formation below, indicates a thickness trend similar to that of the top Havert horizon. The thickest parts of the unit are located in the NB, becoming thinner towards the FP and BP to the east (Figure 4.5B). The thickest parts are observed in the northwest in the Nordkapp Basin (2200 ms TWT) and the thinnest parts are related to the western sector of the BP (600 ms TWT).

The maximum thickness variation observed along the TIFC is 550 ms (TWT). The thickness variations along the fault complex ranges from 450 in the south to 550 ms (TWT) in the north. (Figure 4.5B). The orientaition of the fault along the TIFC has a SW-NE strike in the southernmost parts, transitioning to S-N further north of the fault complex.

Middle Jurassic to upper Jurassic

The unit representing middle to upper Jurassic is defined by the horizon attributed to top Hekkingen above and top Fuglen horizon below. The unit shows a general thinning towards the Finnmark Platform (FP) in the southeast and a thickening towards the Nordkapp Basin in the west. The thickest parts are observed along the flanks of the northwestern and southeastern flanks of the salt diapir within the NB (70 ms TWT), whereas the thinnest parts are located southeast in the FP (25 ms TWT).

Along the TIFC minor thickness variations are observed, ranging from 10-15 ms (TWT) in the south and 20 to 40 ms (TWT) towards the north. The orientaition of the fault along the TIFC has a SW-NE strike in the southernmost parts, transitioning to S-N further north of the fault complex.

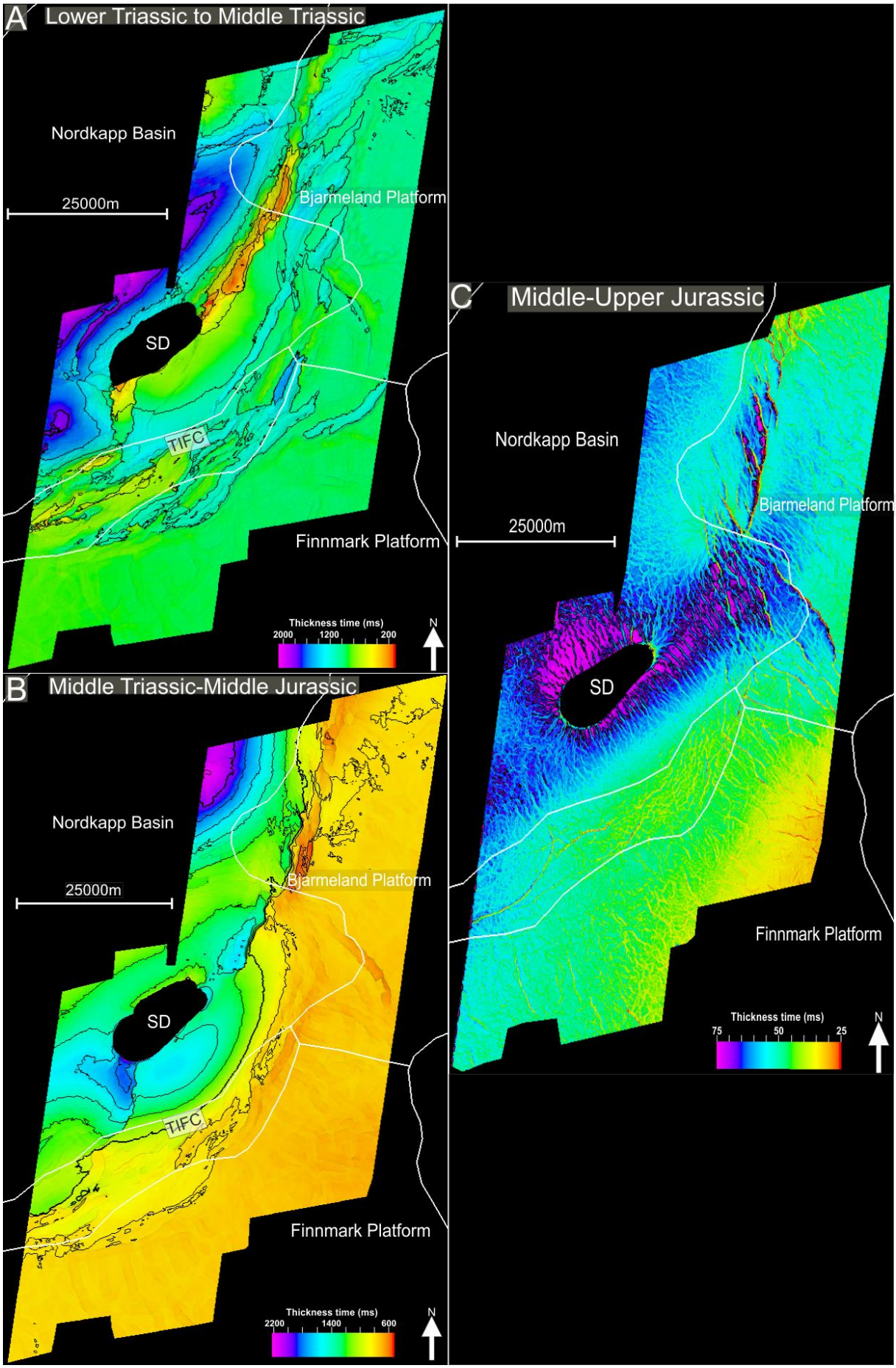
A Lower Triassic to Middle Triassic
Nordkapp Basin
25000m
Bjarmeland Platform
SD
TIFC
Finnmark Platform
Thickness time (ms)
2000 1200 200
N
B Middle Triassic-Middle Jurassic
Nordkapp Basin
25000m
Bjarmeland Platform
SD
TIFC
Finnmark Platform
Thickness time (ms)
2200 1400 600
N
C Middle-Upper Jurassic
Nordkapp Basin
25000m
Bjarmeland Platform
SD
Finnmark Platform
Thickness time (ms)
75 50 25
N

Figure 4.5: A) Time-thickness map of the Lower Triassic unit, bounded by the top Permian horizon at the base and top Havert horizon at the top. Contour lines are set to 300 ms (TWT) intervals. B) Time-thickness map of the Middle Triassic to Middle Jurassic unit, defined by top Havert horizon below and top Fuglen horizon above. Contour lines are set to 300 ms (TWT) intervals. B) Time-thickness map of Middle to Upper Jurassic unit, bounded by the top Fuglen horizon at base and top Hekking horizon at top. Contour lines are set to 75 ms (TWT). ABC) Structural elements from NPD.TIFC=Thor Iversen Fault Complex. SD=Salt diapir.

Cretaceous, sequence 1-3

Sequence 1 (S1)

Sequence 1, delimited by K1 above and top Hekkingen horizon below, displays an increase in thickness towards the south. The internal reflections are parallel and fairly continuous with a low-medium amplitude. The northeastern part of the BP contains the thinnest areas of the sequence (275 ms TWT), while the thickest areas are located southwest of the FP (60 ms TWT).

The maximum estimated thickness variation along the TIFC is 100 ms (TWT) in the south and 200 ms (TWT) in the north (Figure 4.6A). The orientaition of the fault along the TIFC has a SW-NE strike in the southernmost parts, transitioning to S-N further north of the fault complex.

Sequence 2 (S2)

Sequence 2 is delimited by K2 above and K1 below and displays an increase in thickness towards the south (Figure 4.6B). The internal reflections are relatively continuous with a low-medium amplitude. Southwest in the FP the thickest areas of the sequence is up to 375 ms TWT and the thinnest areas are located along the fault in the BP (75 ms TWT).

The maximum thickness variation along the TIFC is estimated to be about 100 ms (TWT) in the southern and 130 ms (TWT) in the northern parts of the fault complex. The orientaition of the fault along the TIFC has a SW-NE strike in the southernmost parts, transitioning to S-N further north of the fault complex.

Structure C is A circular structure has a thickness of 210 ms (TWT) at the flanks of the structure increasing towards the central parts (230 ms TWT) (Figure 4.6B).

Sequence 3 (S3)

Sequence 3 is defined by the overlying K4- and the underlying K2 horizon. The internal reflections have in general low-medium amplitude with the exception of the K3 reflector, which has medium-high amplitude (Figure 4.6C). The internal reflectors are mainly continuous. The thickness of this sequence is generally decreasing towards the south. The thickest areas are observed in the NB (260 ms TWT), along the southern flanks of the diapir, whereas the thinnest area is located east in the BP (40 ms TWT).

Minor thickness variations are observed along the TIFC at about 25 ms (TWT) in the north and 50 ms (TWT) in the south of S3 (Figure 4.6C). The orientation of the faults along the TIFC have a SW-NE strike in the southernmost parts, transitioning to S-N further north of the fault complex.

The circular shaped structure mentioned in the K2 and K3 horizon (Figure 4.3B-C) can also be observed to influence sequence S3 (Figure 4.6C). At this level an increase in thickness up to 220 ms (TWT) at the outer flanks and 190 ms (TWT) in the central parts of the structure (Figure 4.6C) is observed. This structure will be further described sub chapter 4.5.2 (Figure 4.17-18).

URU-Seabed

The URU-Seabed unit is defined by the overlying seafloor and underlying URU horizon. The unit is mapped in a total of 10 separated areas, and has a maximum thickness of 60 ms (TWT) northeast in the study area on the Bjarmeland Platform (BP), and to the far southwest on the Finnmark Platform. The thinnest parts of the mapped unit are 15 ms (TWT) displayed by the smallest polygon within the Finnmark Platform. As shown in chapter 3, the vertical seismic resolution is about 40 meters, thus the unit might have a larger extent, but below this resolution limit.

There are no faults influencing the upper regional unconformity (Figure 4.6D)

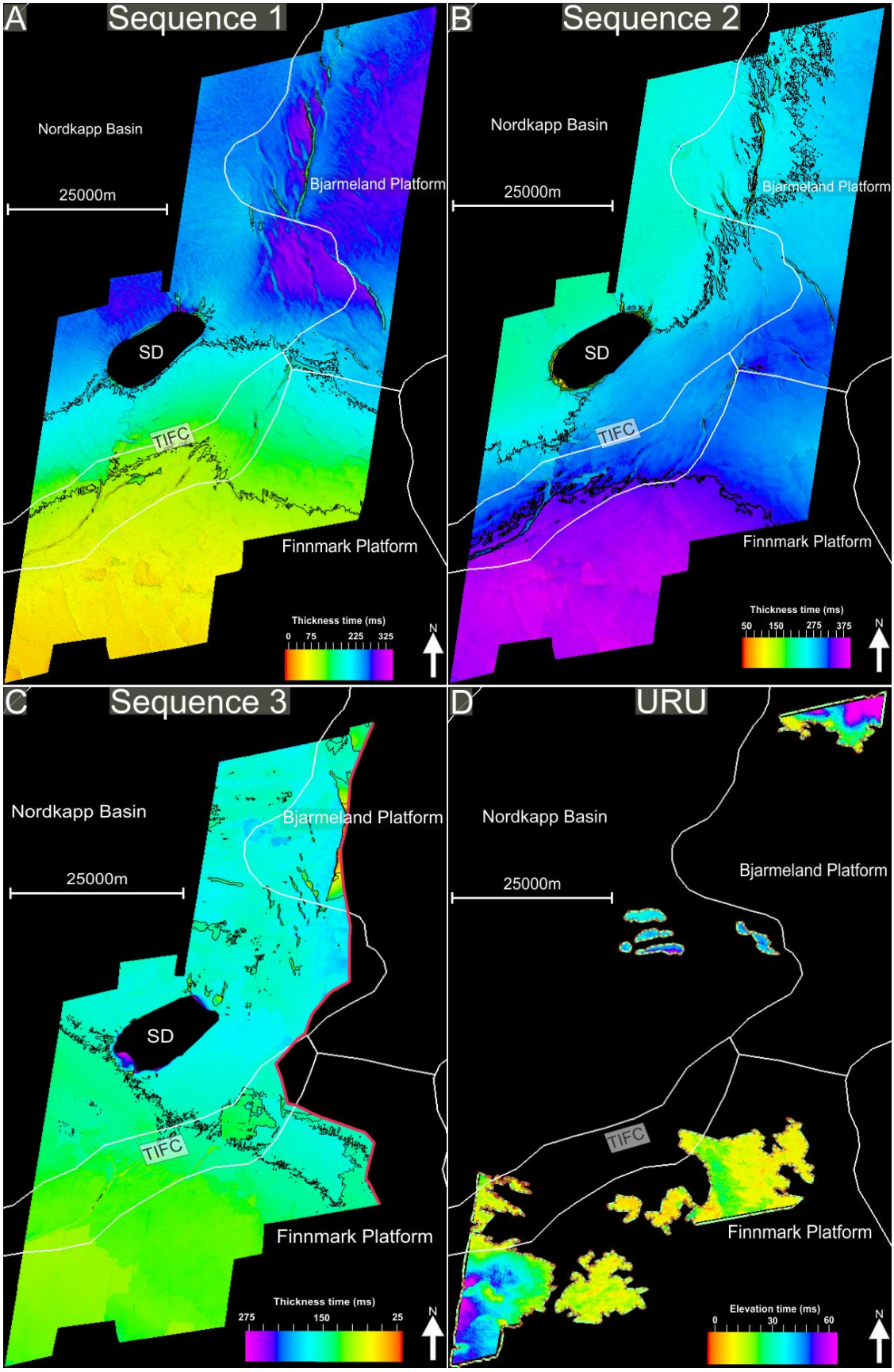
A
Sequence 1
Nordkapp Basin
25000m
Bjarmeland Platform
SD
TIFC
Finnmark Platform
Thickness time (ms)
0 75 225 325
N
B
Sequence 2
Nordkapp Basin
25000m
Bjarmeland Platform
SD
TIFC
Finnmark Platform
Thickness time (ms)
50 150 275 375
N
C
Sequence 3
Nordkapp Basin
25000m
Bjarmeland Platform
SD
TIFC
Finnmark Platform
Thickness time (ms)
275 150 25
N
D
URU
Nordkapp Basin
25000m
Bjarmeland Platform
TIFC
Finnmark Platform
Elevation time (ms)
0 30 60
N

Figure 4.6: A) Time thickness map of sequence S1. Contour lines are set to 100 ms intervals. B) Time thickness map of sequence S2. Contour lines are set to 65ms intervals. C) Time thickness map of sequence S3. The termination of the sequence is illustrated by the red polygon line. Contour lines are set to 74ms intervals. D) Time thickness map of the URU, delimited by the seafloor at top and URU at base. ABC) SD= Salt diapir. ABCD) TIFC=Thor Iversen Fault Complex. Structural elements from NPD.

4.3 The Salt Diapir

The Nordkapp Basin is a salt related basin (Gabrielsen et al., 1990), salt diapirs have no internal reflectors and affects the strata adjacent to the diapir, the salt roof is often marked with a high acoustic impedance (Jenyon, 1986). Based on these criteria's a salt diapir was interpreted within the Nordkapp Basin in the study area.

The salt roof representing a high amplitude contrast, is located at a depth of 300 ms (Figure 4.8), with no underlying internal reflectors (Figure 4.7).The horizons associated with this diapir are all uplifted along the flanks of the diapir (Figure 4.7), where the intra Cretaceous horizons truncates towards the URU and the horizons within the Jurassic-Triassic onlaps onto the diapir (Figure 4.7). The URU is not mapped around the diapir (Figure 4.4A). The salt diapir has an elongated shape (Figure 4.8) with a SW-NE orientation (Figure 4.8). It does not appear to influence the morphology of the seafloor above the diapir (Figure 4.7).

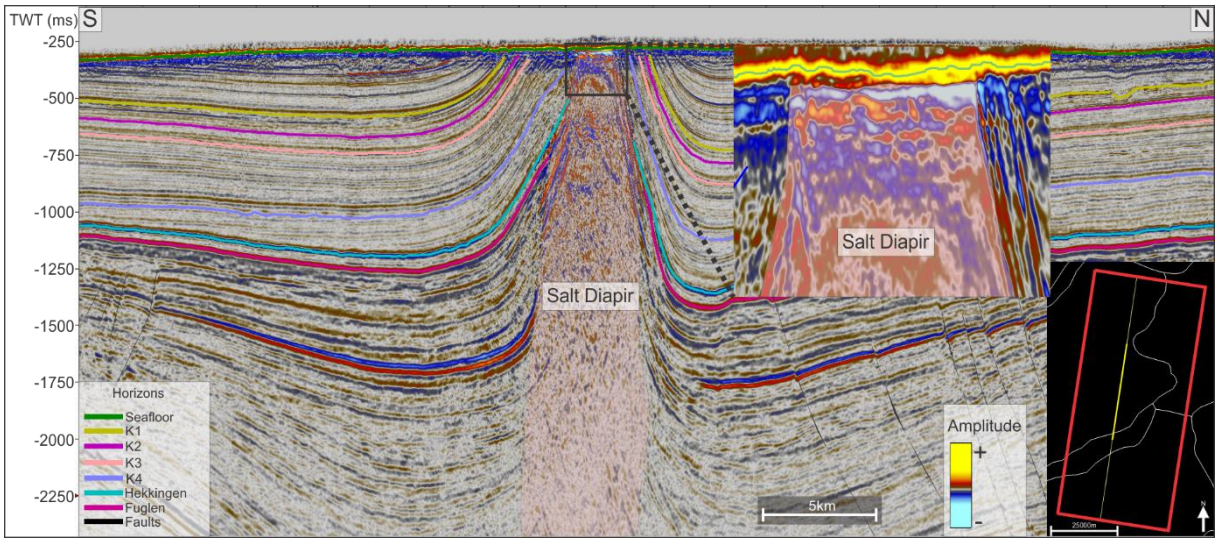

Figure 4.7: Seismic profile through the salt diapir, displaying the uplift of the different horizons within the study area and the outline of the diapir.

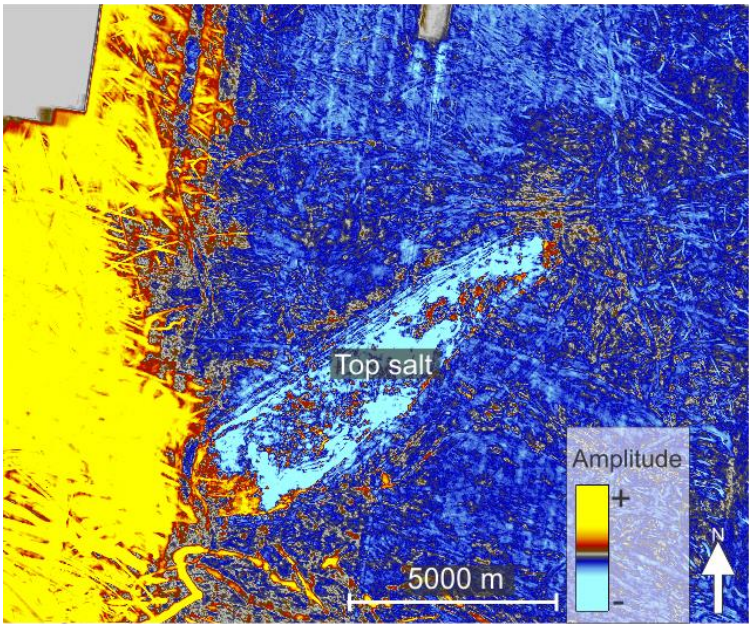

Figure 4.8: Time slice (z=300 ms) through the diapir, displaying the top salt, the location of the salt is displayed in Figure 4.3.

4.4 Faults

The main fault systems within the study area is related to the Thor Iversen Fault Complex (TIFC, Figure 4.9 and 4.10A-C). Isochron maps present the mapped faults and show their strike, dip and the outcrop of each fault at different stratigraphic levels (K4 horizon, top Hekkingen Formation and top Havert Formation, Figure 4.10A-C). The faults along the TIFC and south of the salt diapir, generally terminate in either the Upper Jurassic or below the URU and have extensional features (Figure 4.9).

The faults along the TIFC that terminate towards the URU and the Upper Jurassic, follows trends, in terms of orientation, dip and depth at which they originate. The orientation along the TIFC has the same strike throughout the study area, with a SW-NE trend in the southernmost parts, transitioning to S-N further north of the fault complex. The faults situated in the Triassic and Jurassic intervals generally dip towards the NW in the south and towards the west in the north of the complex (white fault planes in (Figure 4.10A-C), with a few exceptions indicated as black faults with an opposite dip (SE) (Figure 4.10A-B). The dip of the major white faults gradually dips more and more towards the east further north, whereas

the black faults have an opposite trend, dipping more and more west towards the north. The throw seems to generally increase with depth (see throw description of the horizons).

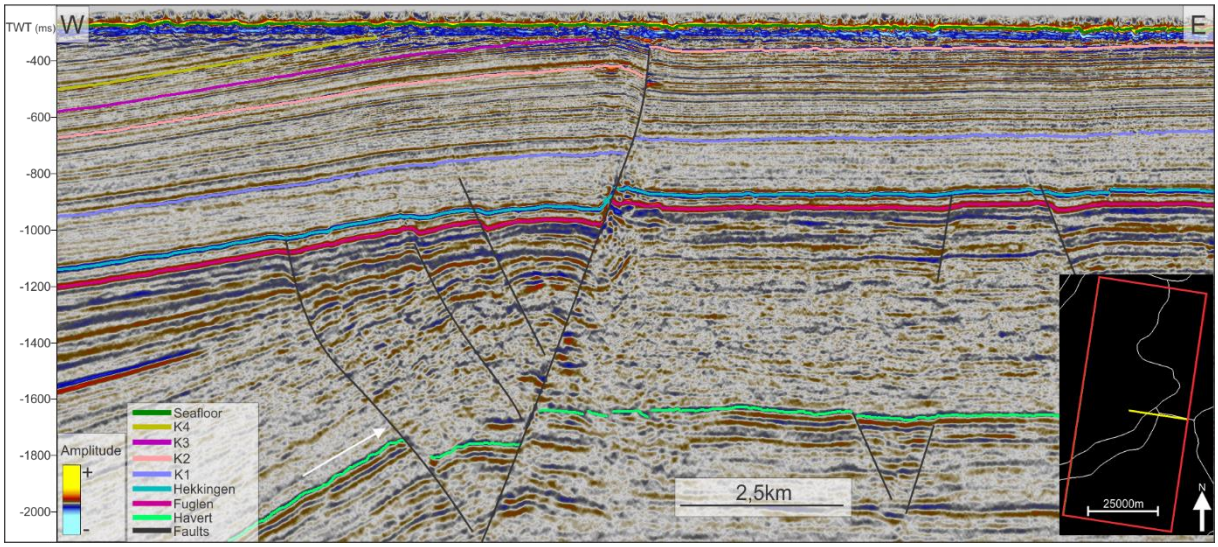

Figure 3.9: Profile displaying the dip, orientation and termination of the faults along the Thor Iversen Fault Complex (TIFC).

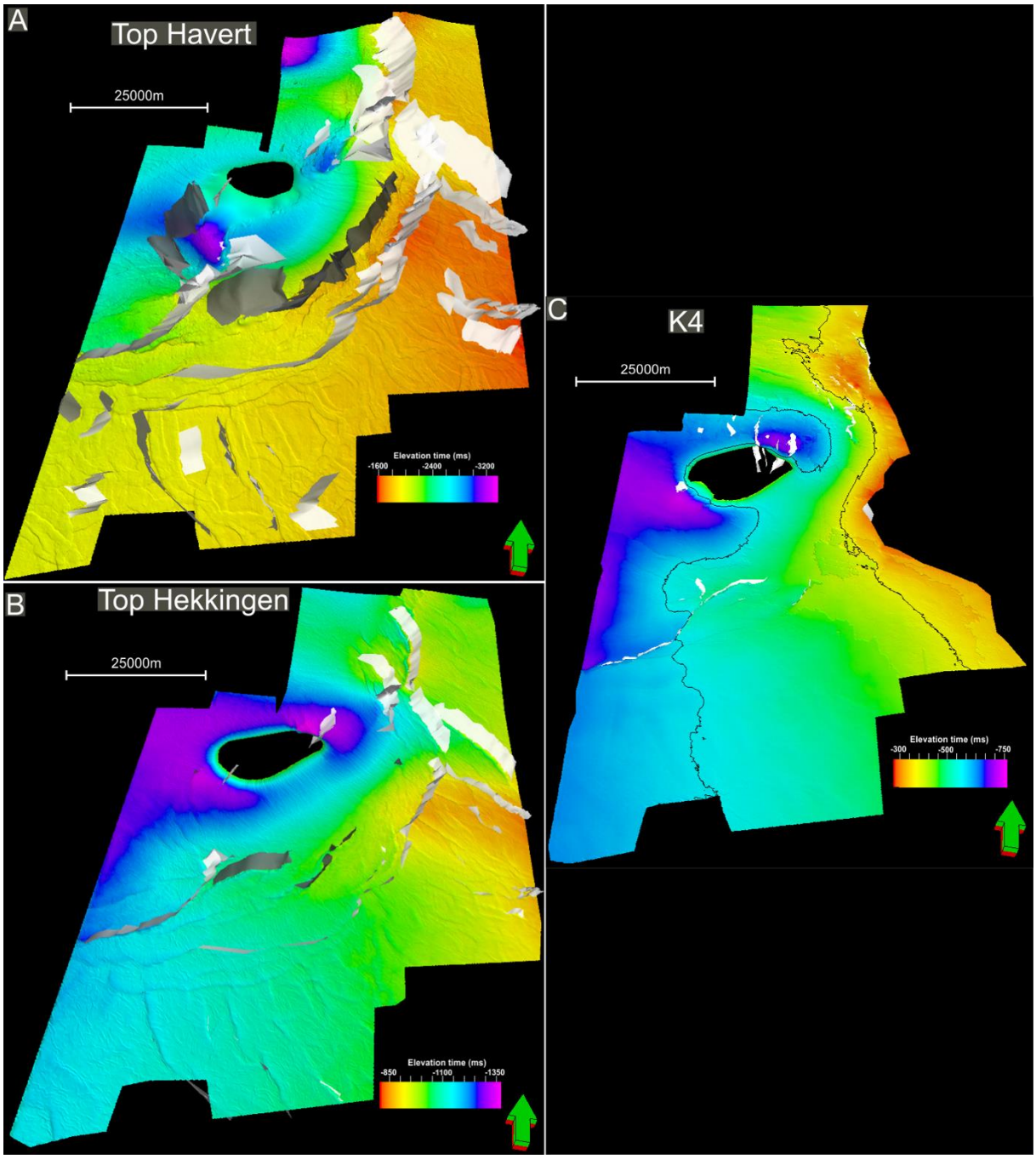

Figure 4.10: A) Isochron map of the top Havert Formation, displaying where the overlying mapped faults are located, their orientation and dip. B) Isochron map of the top Hekkingen Formation, showing the location of the mapped faults above the top Hekkingen, their orientation and dip. C) Isochron map of the K4 horizon, displaying the mapped faults overlying the horizon in addition to their orientation and dip.

4.5 Shallow seismic anomalies

In the following, shallow seismic anomalies are defined at a depth down to 800 ms (TWT). The amplitude anomalies are primarily located below and along the seabed/URU, K1, K2 or K4 horizons, and can be divided into four respective groups:

- Amplitude anomalies below the seabed/URU
- Amplitude anomalies below the K1 horizon
- Amplitude anomalies below the K2 horizon
- Anomalies below the K4 horizon

An overview map of strong amplitude anomalies (amplitude of 0.1 or more) together with variance map was generated for different stratigraphic levels (Figure 4.11A-D). Amplitude anomalies associated with structural closures will be further described below.

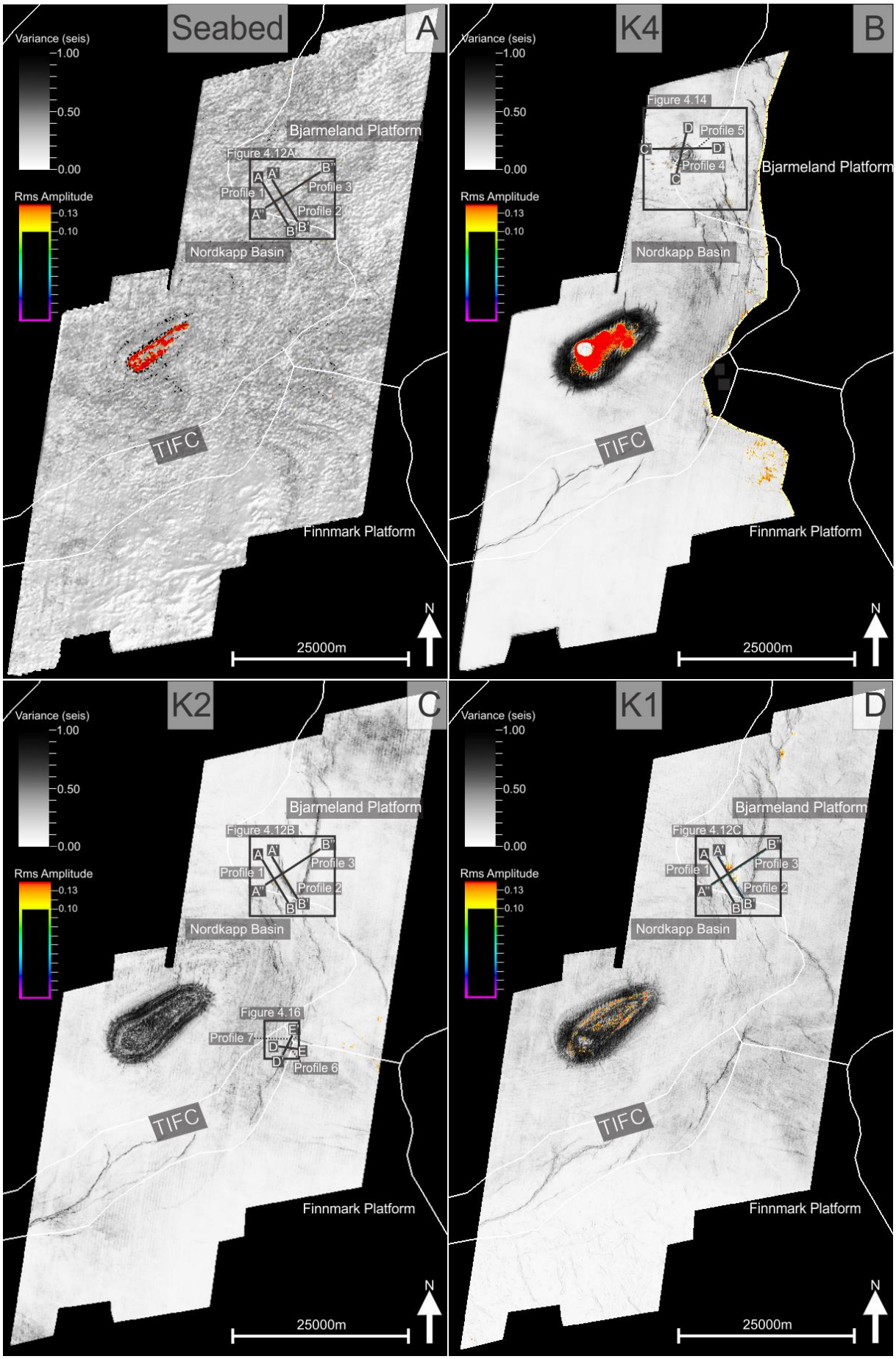
Seabed
A
Variance (seis)
1.00
0.50
0.00
Rms Amplitude
0.13
0.10
Figure 4.12A
Profile 1
Profile 2
Profile 3
Bjarmeland Platform
Nordkapp Basin
TIFC
Finnmark Platform
N
25000m
K4
B
Figure 4.14
Profile 4
Profile 5
K2
C
Figure 4.12B
Figure 4.16
Profile 6
Profile 7
K1
D
Figure 4.12C

Figure 4.11: An overview map highlighting the location of the identified shallow anomalies, defined at a depth down to 800 ms (TWT) (see profile 1-7). Displayed by a combination of an RMS amplitude map together with a variance map, where only the strongest amplitudes are shown, defined by an amplitude of 0.1. A) Variance and RMS amplitude map with a search window of 40ms, starting 10 ms below the seabed. Profile 1,2 and 3 is showcased within figure 4.12A-C in A), B) and C) because there are indications of anomalies in each level and was categorized as structure A. B) Variance and RMS amplitude map with a search window of 40ms just below K4. Profile 4 and 5 highlights the anomalies located adjacent to the circular structure C. C) Variance and RMS amplitude map with a search window of 40ms just below K2. Profile 6 and 7 together with with figure 4.16 displays a possible four way closure/structure B with high amplitudes within. TIFC = Thor Iversen Faults Complex.

4.5.1 Strong amplitude anomalies below the seabed/URU

Two major amplitude anomalies (A1-A2) can be observed below the seabed/URU. These strong amplitude anomalies are located in the northern part of the study area. Both anomalies (A1 and A2) can be characterized as bright spots, as they have reverse polarity compared to that of the seafloor (Figure 4.13, profile 1-3).

Amplitude anomaly 1 (A1)

The amplitude anomaly is located at the outline west of the Bjarmeland Plattform, 600 meters from the Nordkapp Basin borderline, above structure A (defined between K1-K3) (Figure 4.3 A-C). A1 occurs along/beneath the URU/seabed at 280-330 ms (TWT) (Figure 4.13 A-B) and has a linear shape with a NW-SE orientation. The high amplitude anomaly is widest in the northwestern parts exceeding 400 meters in width and gradually thins towards the SE (100 m). The length of the bright spot is about 2050 meters and covers a total area of approximately 0.45 km^2 (Figure 4.12A). The seismic reflection beneath the anomaly is influenced by faults, indicated by the discontinuity of the reflectors. The fault directly below A1 are categorized as F1 (towards the SW, Figure 4.13 A''-B'') and are parallel to the orientation of amplitude anomaly 1 (Figure 4.13 A'-B'), with underlying anomalies (A4) bounded by F1 and F2 (Figure 4.13 A''-B''). The fault seem to terminate about 40-50 ms (TWT) below the seafloor/URU and has the same strike as A1 (NW-SE) dipping towards the NE (Figure 4.13 A''-B'').

Amplitude anomaly 2 (A2)

Amplitude anomaly 2 lies parallel to A1 1.3 km further east, just above structure A (Figure 4.13 A''-B''). The anomaly has an elongated shape with a NW-SE orientation and a relatively constant width (140m). The length is about 2.3 km and the total cover area is about 0.32 km^2 (Figure 4.12A). The amplitude anomaly occurs beneath the URU/seabed between 278-330 ms (TWT). The reflections underneath A2 have the same trend as A1, showing discontinuity of the reflectors indicating the fault F2 (towards the NE, Figure 4.12). The underlying amplitude anomaly 5 (see below) is bounded by F1 and F2 (has the same dip as F1) (Figure 4.13 A''-B'').

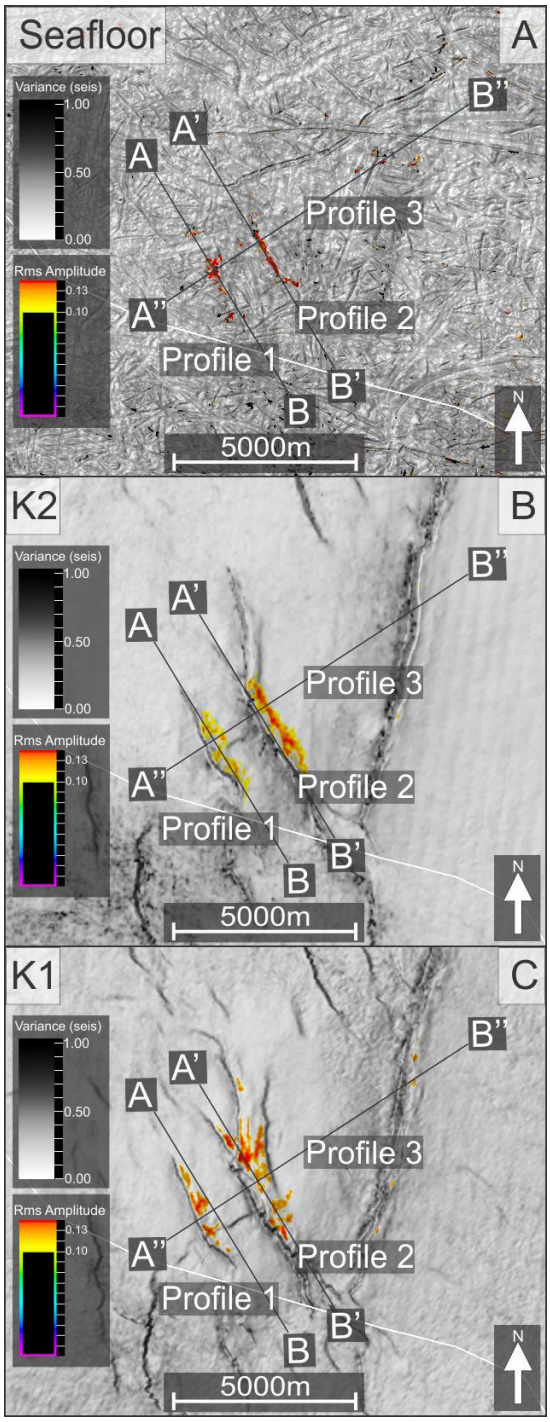

Figure 4.12: Variance and RMS amplitude map (displaying only the highest values) with locations and search windows as indicated in Figure 4.11. A), B) and C) highlights the shallow anomalies located in each stratigraphic level (Seafloor, K2 and K1) and gives a more detailed impression of the outline of each bright spot, morphological features, structures and profile 1-3 compared to figure 4.11. The amplitude anomalies in B) and C) is located at structural highs, referred to as structure A.

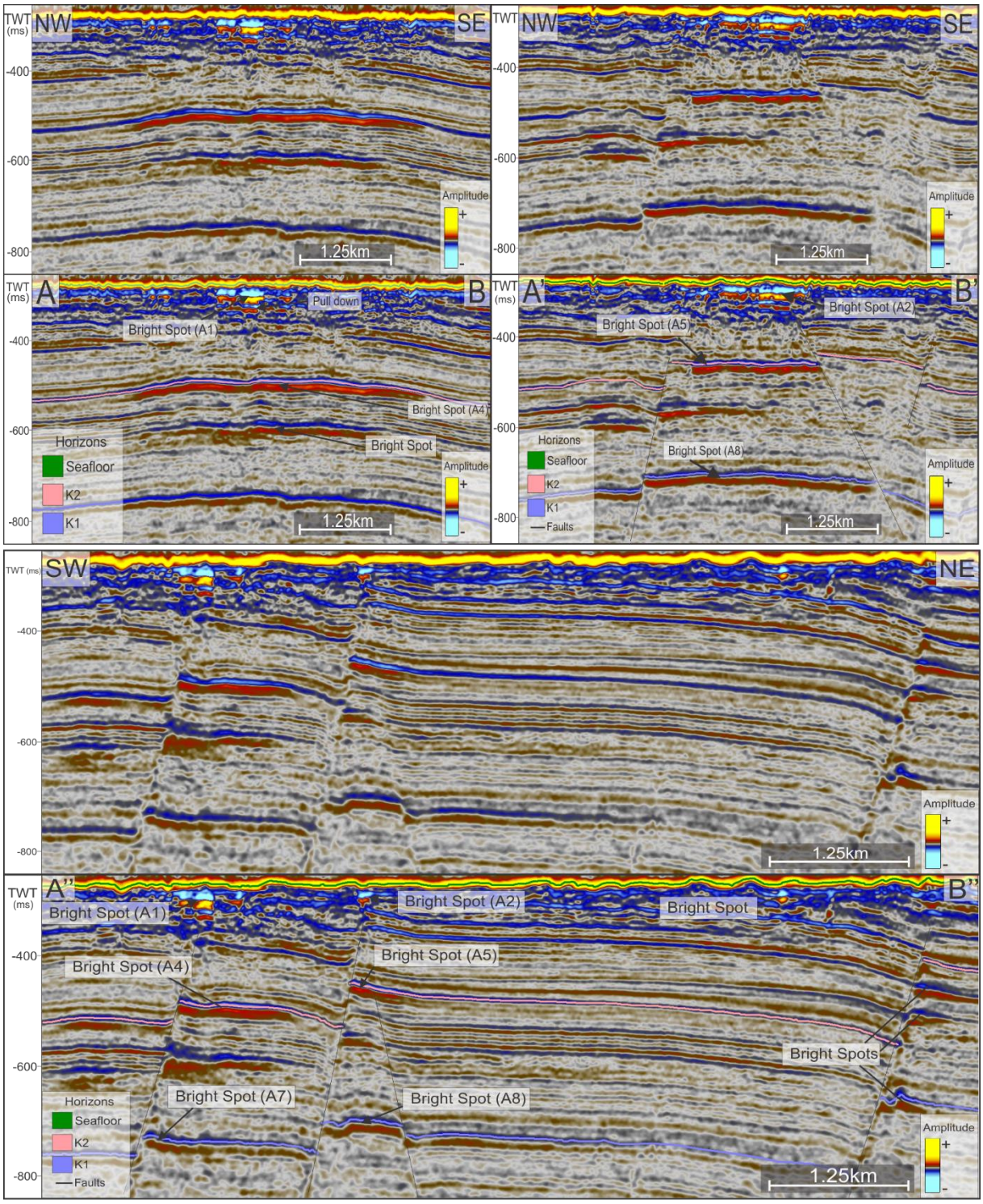

Figure 4.13: A-B) Seismic profile (profile 1) displaying the distribution of shallow bright spots as shown in figure 4.11- 4.12. A'-B') Seismic profile (profile 2) showcasing the shallow bright spots as indicated in figure 4.11-4.12. The bright spots are located at the same stratigraphic levels as figure 12. A''-B'') Seismic profile (profile 3) displaying the shallow bright spots as indicated in figure 4.12. Profile 1-3) The bright spots of each profile (1-3) are located at four different stratigraphic levels, below: the seabed, K1 and K2, and between K1 and K2. Each bright spot is located at a structural high (except A1 and A2), the structure in which the anomalies A4-A5 and A7-A8 is situated in is referred to as structure A.

4.5.2 Strong amplitude anomalies below the K4 horizon

Structure C and amplitude anomalies 3 (A3)

5 minor amplitude anomalies and 1 larger anomaly are located north in the study area at the boundary between the Nordkapp Basin (NB) and the Bjarmeland Plattform (Figure 4.14). The seismic amplitude anomalies can be observed at the outer flanks of the circular structure C (Figure 4.3 B-C)(indicated by the high variance values, Figure 4.14) below the K4 horizon, with reflections having a reverse polarity compared to the seafloor (Figure 4.15). The larger anomaly covers an area of approximately 0.135km^2, at a depth of 400-438 ms (TWT) (Figure 4.14). The minor anomalies are similar in size 0.05 km^2. The strong anomalies have an elongated to oval shape with an orientation varying from NE-SW and E-W (Figure 4.14). The seismic pattern adjacent to the anomalies is dominated by discontinues reflectors, indicating the influence of faulting (4.15 A-B). The faults seem to terminate towards the K4 horizon extending down to just below the K1 horizon (Figure 4.15 A-B). Structure C marks the lateral extent of these faults and has a diameter ranging from of 4.5km below K4, decreasing to 3.6 km below K2 (Figure 4.3 B-C). The vertical extent of structure C, starts 40 ms below K4 (Figure 4.14) down to 170 ms below K2. There are no amplitude anomalies observed above A3, there are however an increase in amplitude along the K2 reflector (Figure 4.15).

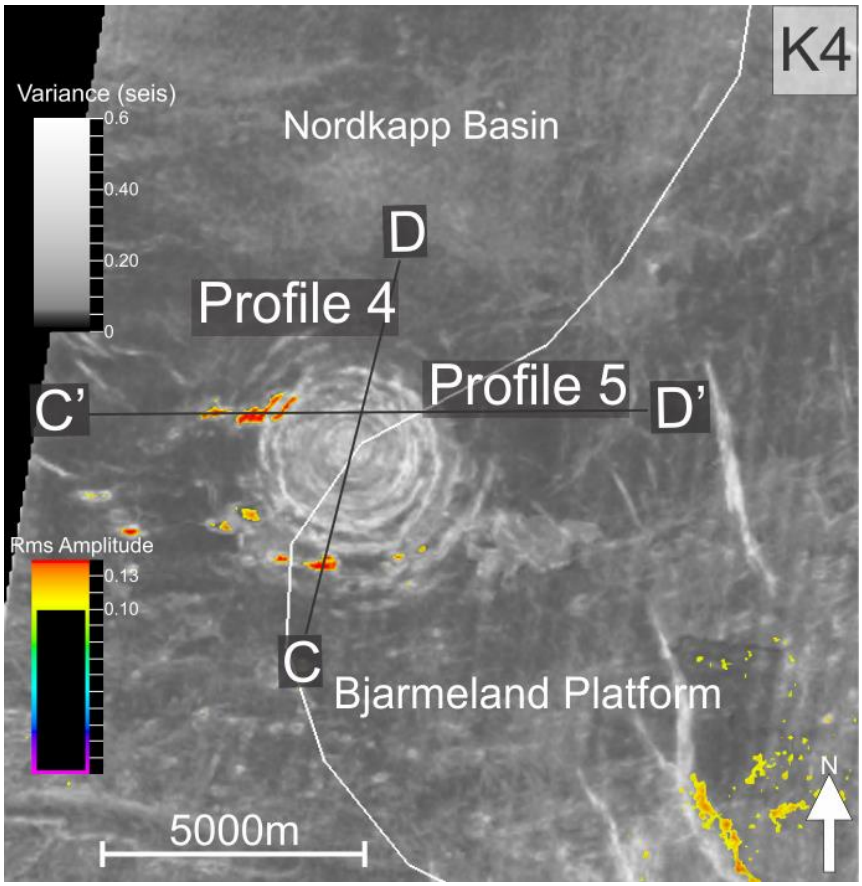

Figure 4.14: Variance and RMS Amplitude map with a 40 ms seach window below K4. Displaying the total area coverage of the amplitude anomalies at the flanks of the circular structure C and the location of profile 4 and 5. Structural elements from NPD.

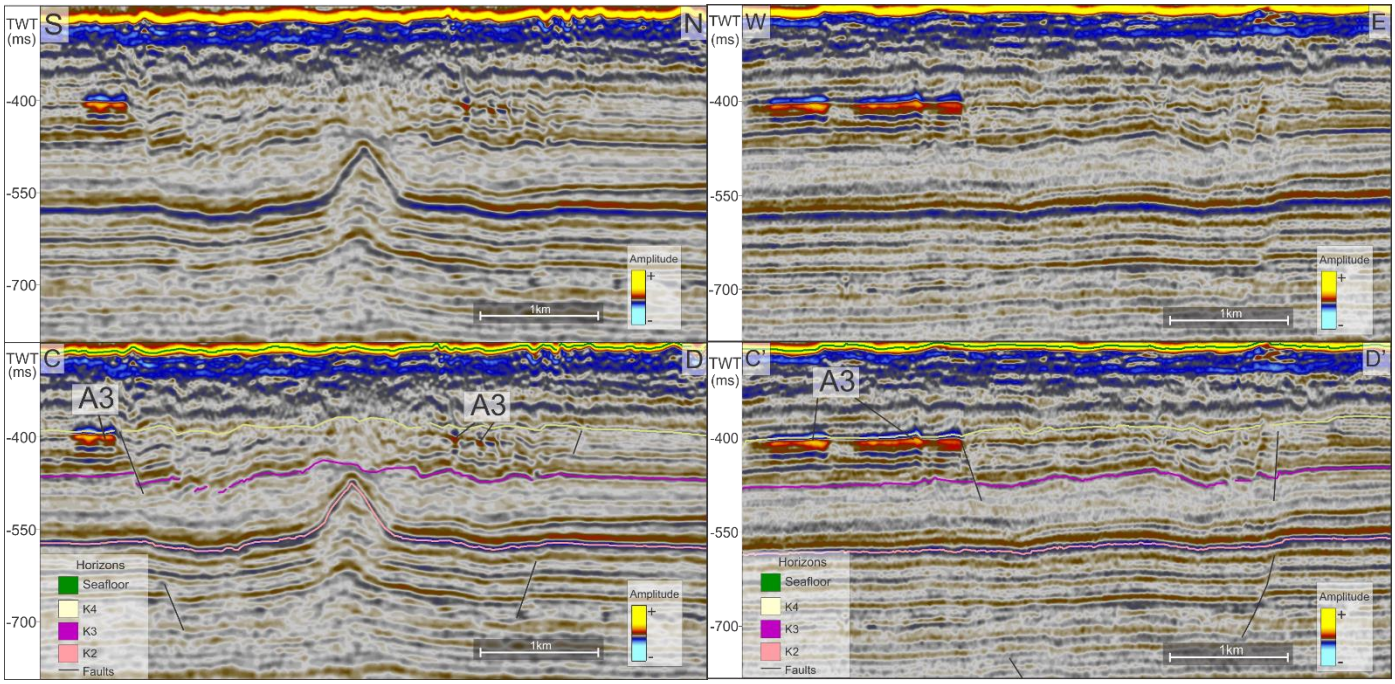

Figure 4.15: C-D) Seismic profile 4, showing the shallow amplitude anomaly 3, lying adjacent to the faults. The amplitude anomalies are located just below the reflector representing the K4 horizon. The faults mark the extent of the circular shape of structure C. The reflector representing the K2 horizon is uplifted in the central parts of structure C. C'-D') Seismic profile 5, displays seismic amplitude anomaly 3 as indicated in figure 4.14, lying below the K4 horizon. The faults show the extent of structure C.

4.5.3 Amplitude anomalies below the K2 horizon

Structure A-B and amplitude anomaly 4-6 (A4-A6)

Three amplitude anomalies (A4-A6) are located along/underneath the K3 horizon. A4 and A5 are located north in the study area within structure A (4.3 A-C), whereas A6 lies further south within structure B (4.3 B). The reflection of the strong anomalies (A4-A6) has a reverse polarity compared to the seafloor (Figure 4.13, 4.17 and 4.18).

Structure A and amplitude anomaly 4 (A4)

The seismic amplitude anomaly 4 is located below A1, at the western margin of the BP, along/underneath the reflector representing the K2 horizon, between 480 and 518 ms (TWT) (Figure 4.13 A-B). A4 and A1 have the same trends in terms of location, orientation (NW-SE) and shape (linear in all cases) (Figure 4.12 A and B). The width of the anomaly is largest in the northwest (401 m), gradually thinning towards the southeast (118m). The length is about

2.7 km and covers a total area of about 0.6 km^2 Figure 4.12B). Profile 1 shows the long axes of the anomaly and indicates that the anomaly is situated at a structural high, characterized as structure A (Figure 4.3 A-C, 4.11-13). The seismic reflections below, adjacent and above the amplitude anomaly 4 show increased amplitudes and discontinuous reflections. The A4 is bounded by F1 to the SW and F2 to the NE of the anomaly (Figure 4.13 A''-B''). Faults F1 and F2 extend down to the deeper parts of Triassic and have the same strike as the amplitude anomaly and terminates below the seabed/URU. The reflectors adjacent to F2 are downfaulted from NE to SW, which is also the case for the reflectors adjacent to F1. Between F1 and F2 the reflectors dip towards the NE and the same trend is observed for the reflectors NE of F2, whereas SW of F1 the reflector dips the opposite direction (SW). Hence, structure A shows slight anticline characteristics. Cross-section of the A4 (Figure 4.13 A''-B'') displays how the anomalies accumulate toward F1, dipping toward NE. High amplitudes with reverse polarity can also be observed SW of F1, below the reflector represented by the K2 horizon, dipping towards the SW (Figure 4.13 A''-B'').

Structure A and amplitude anomaly 5 (A5)

The strong amplitude anomaly 5 is located along/beneath the reflector representing the K2 horizon at a depth between 445 and 472 m, below the A2 and adjacent to the A4 (1.3 km east, Figure 13A'B'). The average width of the anomaly is 220 m, with a length of 3000 m, covering a total area of 0.66 km^2 (Figure 4.12B). Amplitude anomaly 5 is also situated at structure A (Figure 4.3 and 4.13 A'B' and A''-B''). A5 has a linear shape with a NW-SE orientation and appears to be bounded by two faults perpendicular to the extent of the anomaly (Figure 4.13 A'-B'). These faults are laterally minor and shallow seated faults, with a S-N strike dipping towards the south (the fault towards NW,) and north (the fault towards SE,), forming a horst structure. The amplitude anomaly 5 dips towards the NE and F2 lies parallel to it. The amplitude anomaly appears to increase in size towards the fault.

Structure B and amplitude anomaly 6 (A6)

The seismic anomaly 6 is located at the northern margin of the TIFC, bordering BP, FP and NB. A6 has a length of 1160 m and an average width of 310 m, covering a total area of 0.358 km^2 (Figure 16). The reflectors above A6 (K2 horizon) are dipping in four different directions

(Figure 4.17 and 4.18), indicating a potential four-way closure and are characterized as structure B. The anomaly occurs along/below the reflector represented by the K2 horizon, between 408 and 450 ms (TWT) and is elongated with an NNS orientation. The reflectors east of the anomaly display discontinuity, indicating a fault categorized as F3 with NNE strike and westward dip (Figure 4.17). The fault appears to terminate below URU/seabed and stretches down to the Lower Triassic. The A6 is situated below a structural high (structure B) (Figure 4.3 B and 4.16-18). Structure B has the same orientation as A6 and is widest (450m) in the south and thinnest towards north (150m), with a length of 3200m and follows the K2 reflector (Figure 4.3B and 4.16). The top of the amplitude anomaly has a curved shape and strong amplitude. The strength of the amplitude anomaly decreases and flattens towards the base. A6 follows the structural trend of the elongated structure (Figure 4.16-18).

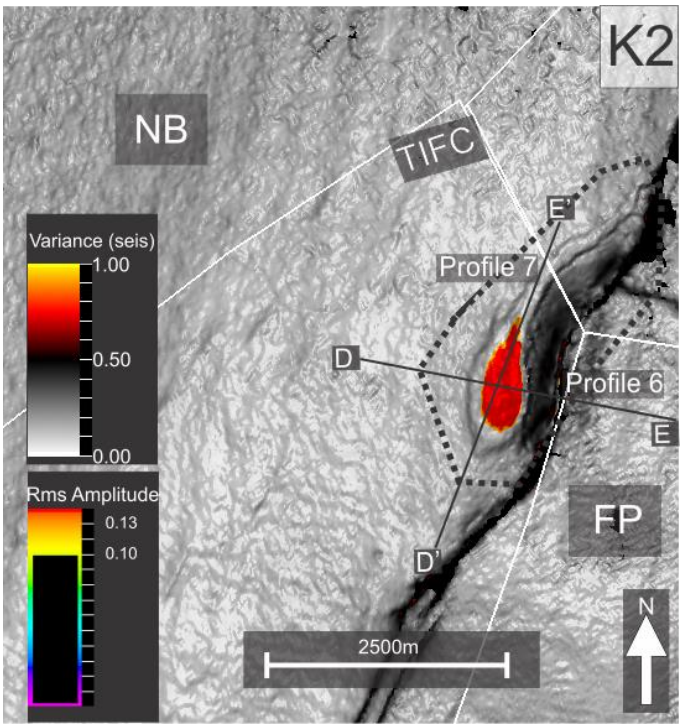

Figure 4.16: Variance and RMS Amplitude map with a 40 ms search window below K2. Displaying the total area coverage of the amplitude anomalies within the elongated structure B and the location of profile 6 and 7. Structural elements from NPD. TIFC=Thor Iversen Fault Complex. FP=Finnmark Platform. NB=Nordkapp Basin.

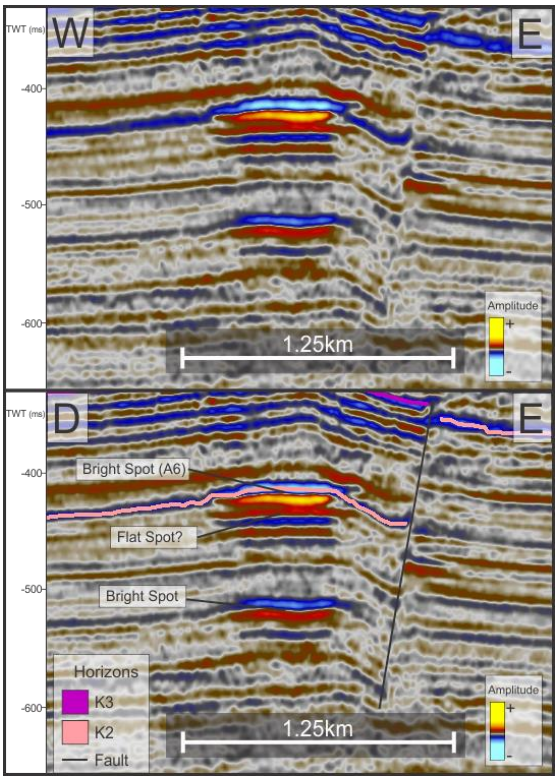

Figure 4.17: Seismic profile (profile 6, D-E) displaying seismic amplitude anomaly A6 as indicated in figure 4.16. The anomalies are located below the K2 horizon, representing structure B.

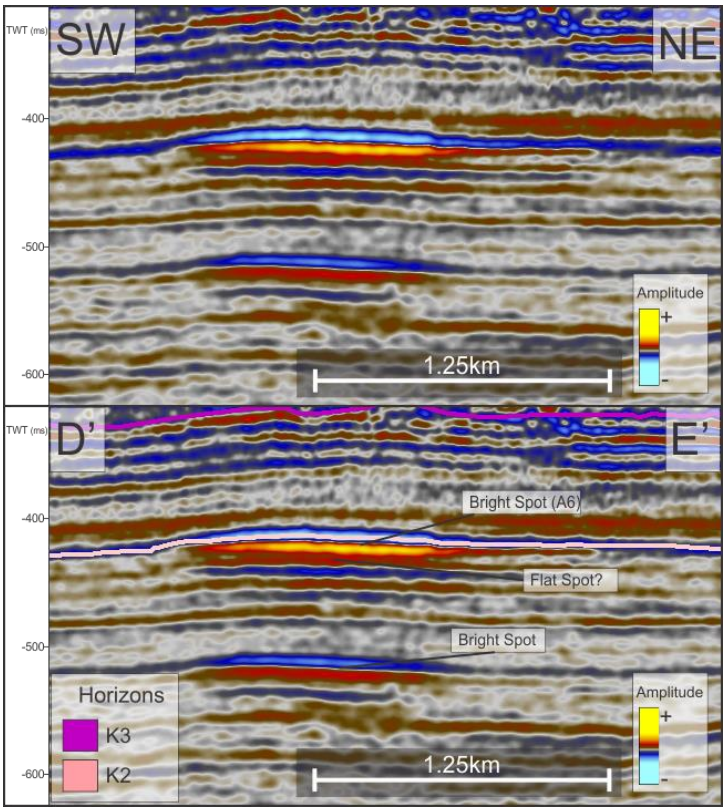

Figure 4.18: Seismic profile (profile 7, D'-E') showing the outline of A6 as indicated in figure 4.16. The amplitude anomalies are located below the K2 horizon, representing structure B.

4.5.4 Amplitude anomalies below the reflectors represented by the K1 horizon

Structure A and amplitude anomaly 7 (A7)

Seismic amplitude anomaly 7 is located below anomaly A4 and is also situated within structure A, along/below the reflector representing the K1 horizon between 740-770 ms (TWT). The anomaly has an elongated shape (Figure 4.12C), with an average width of 400 m and 1700 m in length. The total coverage area of A7 is about 0.68 km^2. A7 is dipping towards the NE and is located at a structural high within structure A, bounded by F1 and F2. The reflection of the A7 has a reverse polarity compared to the seafloor (Figure 4.13 A-B).

Structure A and amplitude anomaly 8 (A8)

Amplitude anomaly 8 is observed beneath A5, along/below the reflector representing the K1 horizon, within structure A between 690 and 724 ms (TWT). The anomaly 8 can be divided in two (A8' and A8'', Figure 4.12C) and shows reverse polarity compared to that of the seabed reflection (Figure 4.13A'-B'). The shape of A8' and A8'' is elongated with a NW-SE orientation. A8' is located towards the NW coving an area of 0.4 km^2, whereas A8'' is located towards the SE covering an area of 0.2 km^2. The dip of A8 is towards the NE and is bounded by F2, F3 and F4 (Figure 4.13 A''-B'').

4.6 Gas Flares

Out of 3868 lines of the processed water column data, only 7 lines show strong amplitude anomalies, indicating potential flares: 3489, 2203, 1987, 1199-95-92 and 1248 (Figure 4.19). Profiles 8-12 (Figure 4.20, 4.21, 4.23, 4.25 and 4.27) displays shallow bright spots, faults and unit truncations beneath the gas flares, the location of each profile is indicated in figure 4.19. The potential flares will be further described by correlating with seismic profiles and 3D images of the flares and surrounding seafloor. 3D view of the flares will only be used to highlight the strongest amplitude anomalies.

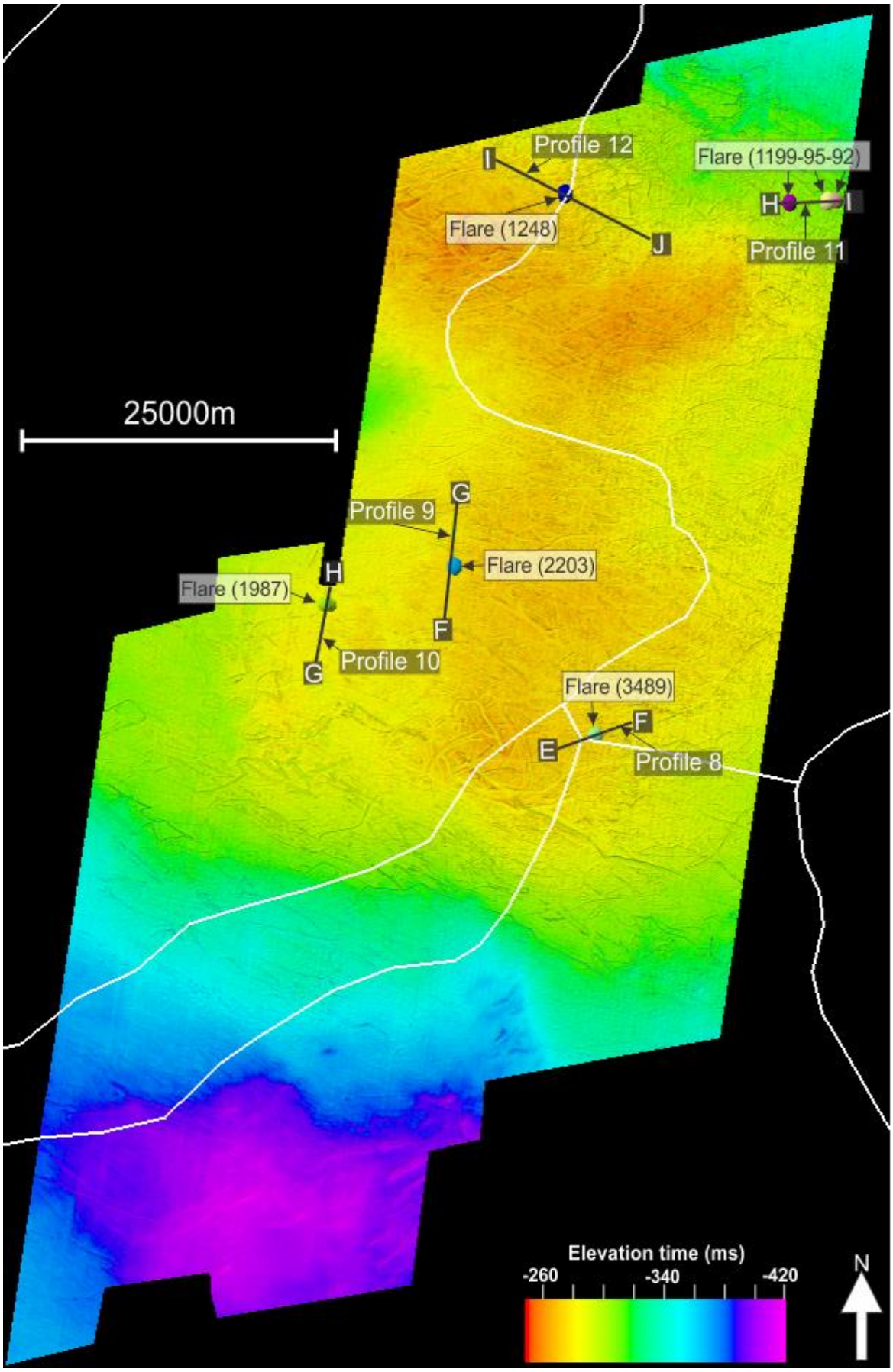

Figure 4.19: Isochron map of the Seafloor horizon, depth displayed in TWT (ms). Highlighting the strongest flares observed in the study area.

4.6.1 Potential Flare 1 (PF1), line 3489

One potential flare in inline 3489 was observed in water column data as an anomalously high amplitude compared to the ambient water column (Figure 4.20). The high amplitude anomaly has a linear shape with a slight bend and is situated close to the seafloor. PF1 is located east of A6 (Figure 4.20) at the northern margins of the TIFC above the seafloor. The potential flare has a height of 15 meters and is connected to the seafloor. The reflectors below the seabed are displaced by faulting. The fault farthest from structure B (Figure 4.20) terminates above the reflector representing K2 and is situated below the PF1 but has no amplitude anomalies associated with it.

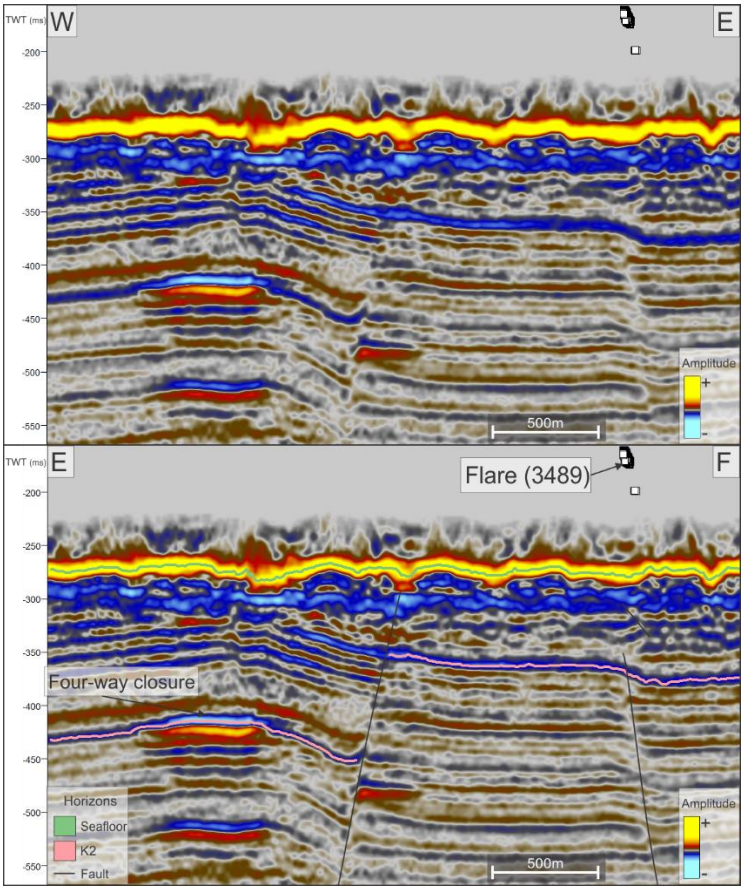

Figure 4.20: Seismic profile (profile 8, E-F, Figure 4.19) displays the outline of the flare in line 3489. The flare is located just above a fault and east of structure B/ a potential four-way closure.

4.6.2 Potential Flare 2 (PF2), line 2203 and amplitude anomaly 9

Two potential flares in inline 2203 (flare 1 and flare 2, Figure 4.22) were observed in the water column data as a high amplitude anomalies compared to the water column (Figure 4.21). Flare 1 (Figure 4.22) has a height of 22 m, amplitude of approximately 5 and the base is situated at a water depth of 204 m (Figure 4.22). The height of flare 2 is 15 m (Figure 4.22), the amplitude value is about 12 (Figure 4.22C) and the base is observed at a water depth 200 m (Figure 21). A linear shape with a slight bend and connection to the seafloor characterizes both flare 1 and 2. PF2 is situated in the central parts of the NB (Figure 4.19), just above the seafloor (Figure 4.21). The reflectors below PF2 and the seabed towards the north display high amplitude anomaly 9 with reverse polarity compared to the seafloor, indicating a bright spot (Figure 4.21).

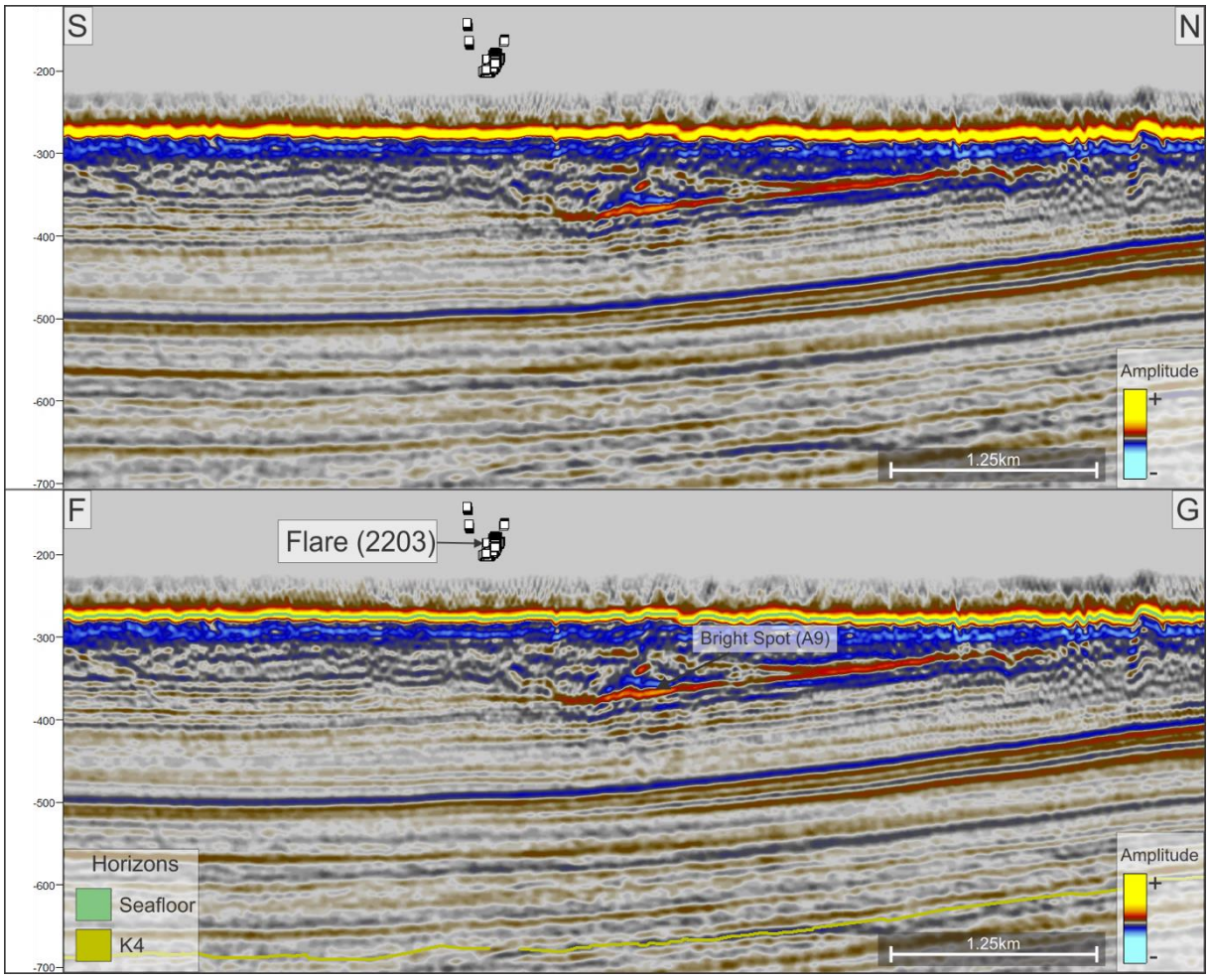

Figure 4.21: Seismic profile (profile 9, F-G, Figure 4.19) shows the outline of the flare in line 2203, with the underlying amplitude anomaly 9.

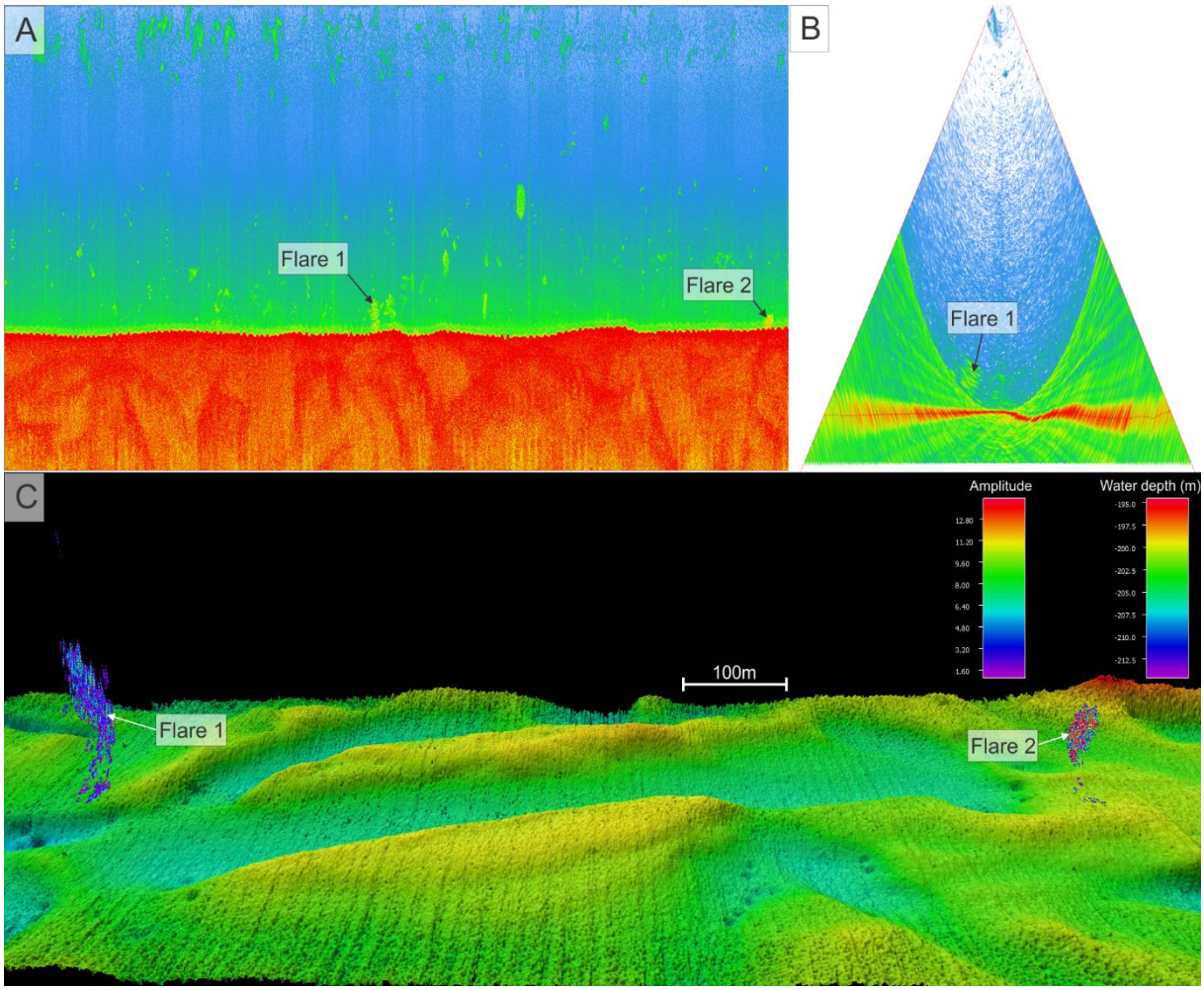

Figure 4.22: Water column anomalies at line 2203 (Figure 4.19 and 4.21). A) R-stack view of what might be potential flares indicated as flare 1 and 2. B) Fan view of the possible flare 1. C) 3D view of the potential flare 1 and 2, their amplitudes in addition to the water depth and minor depressions.

4.6.3 Potential Flare 3 (PF3), line 1987

There are three potential flares at line 1987 (flare 1, 2 and 3, Figure 4.24) and is characterized as high amplitude anomalies within the water column (Figure 4.24). Flare 1, 2 and 3 show no connection to the seafloor, they are linear in shape and have amplitude of approximately 3 (Figure 4.24 C). These potential flares are situated above a linear depression inhabiting minor circular depressions along the linear structure (Figure 4.24). The height of flare 1 is 20 meters, flare 2 is 15 meters (Figure 4.24 C) and flare 3 is 8 meters high (Figure 4.24 C). Potential flare 3 is located at the northern flank of the salt diapir within the NB (Figure 4.19). The

underlying reflectors are uplifted and truncate toward the seafloor/URU south of the flare (Figure 4.23). Below/along the seafloor a relatively high amplitude can be observed beneath PF3 in addition to a fault terminating below the seafloor (Figure 4.23).

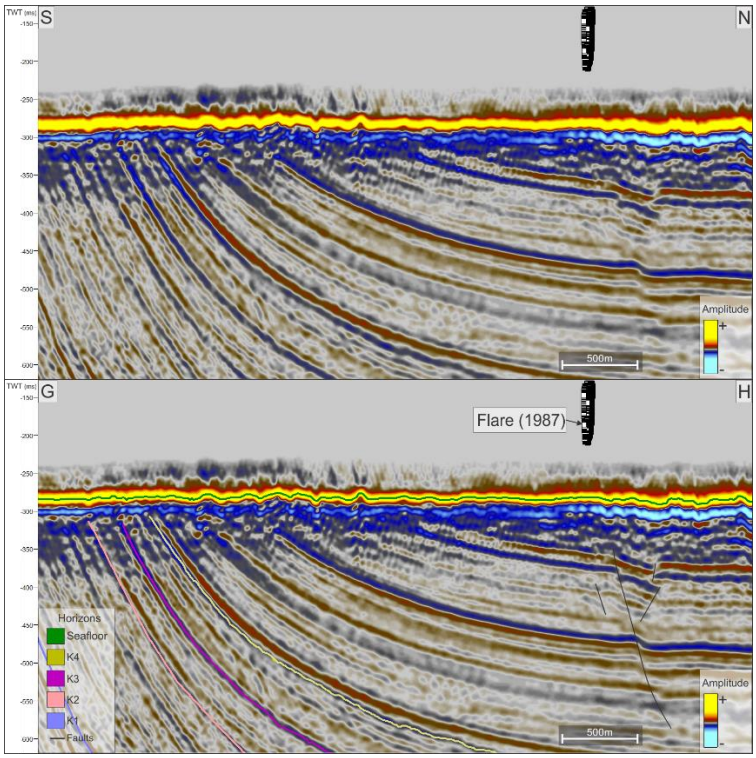

Figure 4.23: Seismic profile (profile 10, G-H, Figure 4.19) indicates the potential flare in line 1987, with an underlying anomaly and fault.

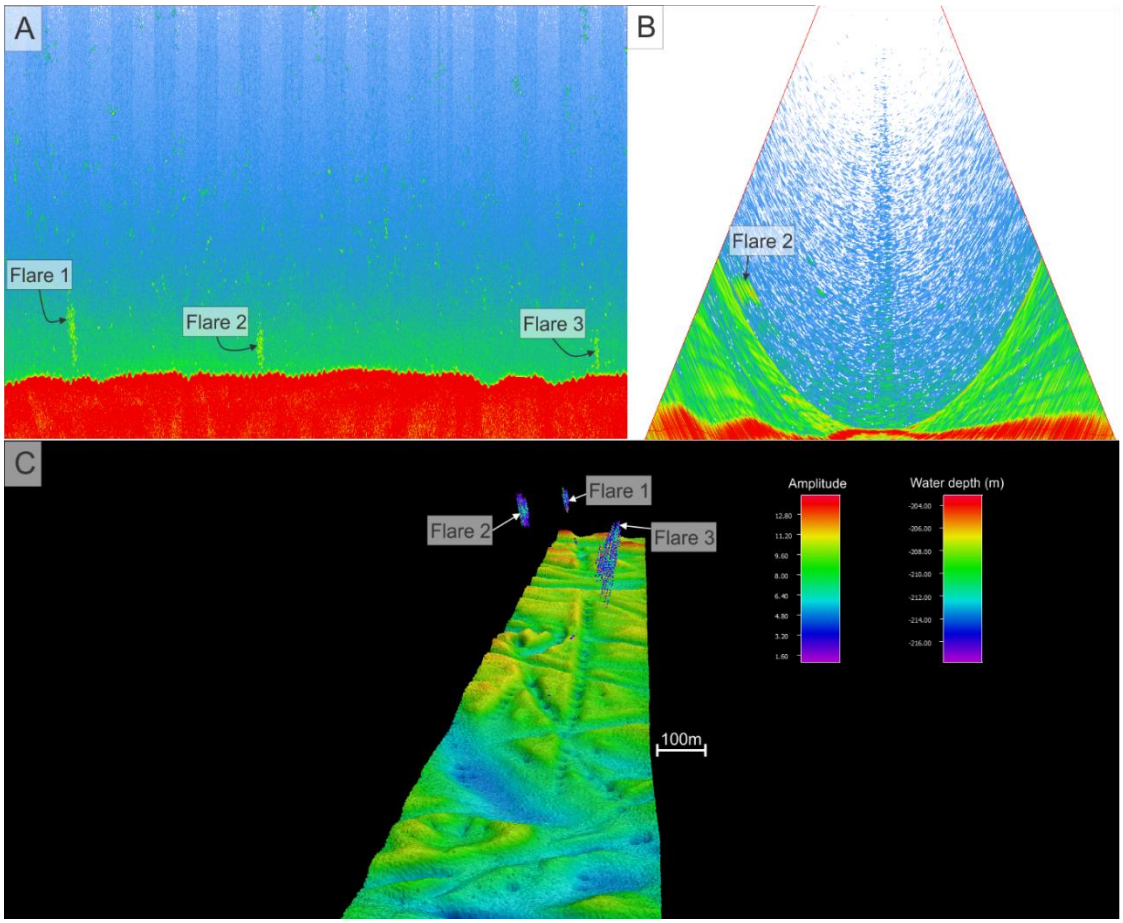

Figure 4.24: Water column anomalies at line 1987 (Figure 4.19 and 4.23). A) R-stack view of potential flare 1,2 and 3. B) Fan view of the potential flare 2. C) 3D view of flare 1,2 and 3, their amplitudes, water depth and minor depressions.

4.6.4 Potential Flare 4 (PF4, line 1199), 5 (PF5, line 1192) and 6 (PF6, line 1195)

Potential flares in line 1199 (PF4), 1192 (PF4) and 1195 (PF6) is located NE in the study area, within the Bjarmeland Plattform (Figure 4.19). They are characterized by their high amplitude anomalies compared to the water column (4.26). The reflectors below the potential flares are truncating towards the seafloor reflection and display an increase in amplitude towards the upper truncations (Figure 4.25), this is especially evident at the anomalies along the K3 reflector. The water column amplitude anomaly of the potential flare 5 and 6 are quite similar, while PF4 stand out. PF4 has the highest amplitudes and is therefore further highlighted (Figure 4.26).

Potential Flare 4 (P4), line 1199

There are four potential flares at line 1199 (flare 1, 2, 3 and 4, Figure 4.26) with a similar amplitude of 4 (Figure 4.26 C). Flare 2, 3 and 4 have connection to the seafloor at a water depth of 224 m, flare 1 has, however, has no connection (Figure 4.26C). The height of flare 1 is 16 m and it is situated above a minor circular depression. Height of flare 2 is 17 m, height of flare 3 is 14 m and they are also observed above circular seabed depressions. Flare 4 has a height of 8 m and originates from an elongated depression on the seafloor. The flares demonstrate a slight bend likely due to activity of the bottom currents.

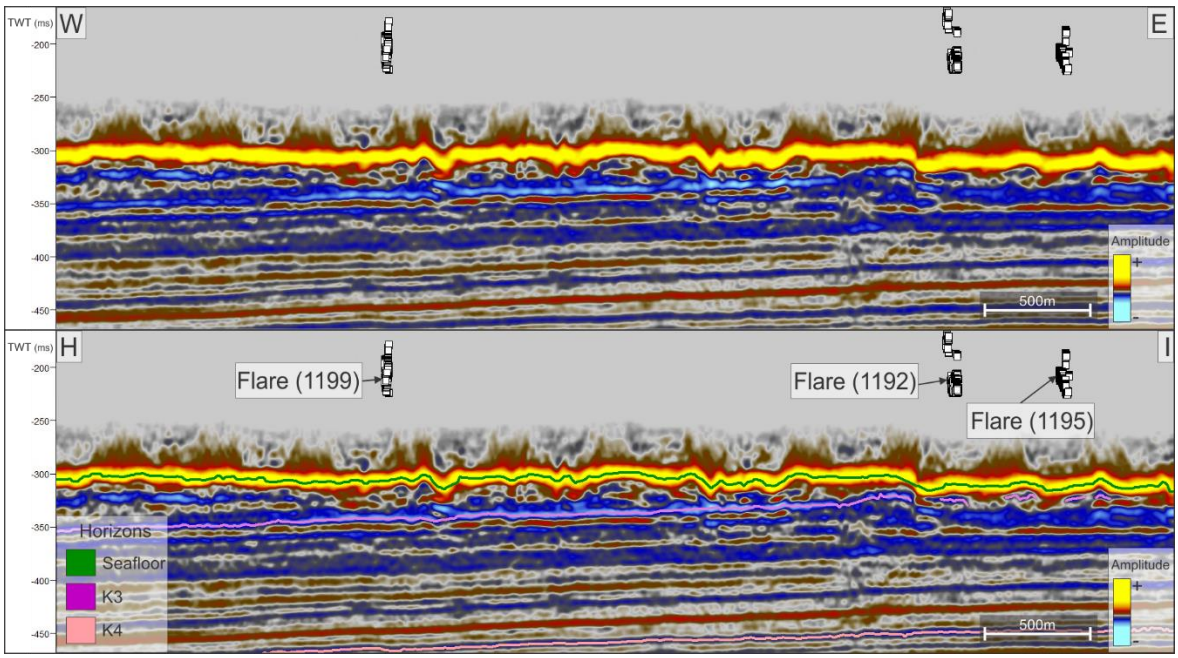

Figure 4.25: Seismic profile (profile 11, H-I, Figure 4.19) displays the outline of the flare in line 1199-92-95, located above truncating Cretaceous units.

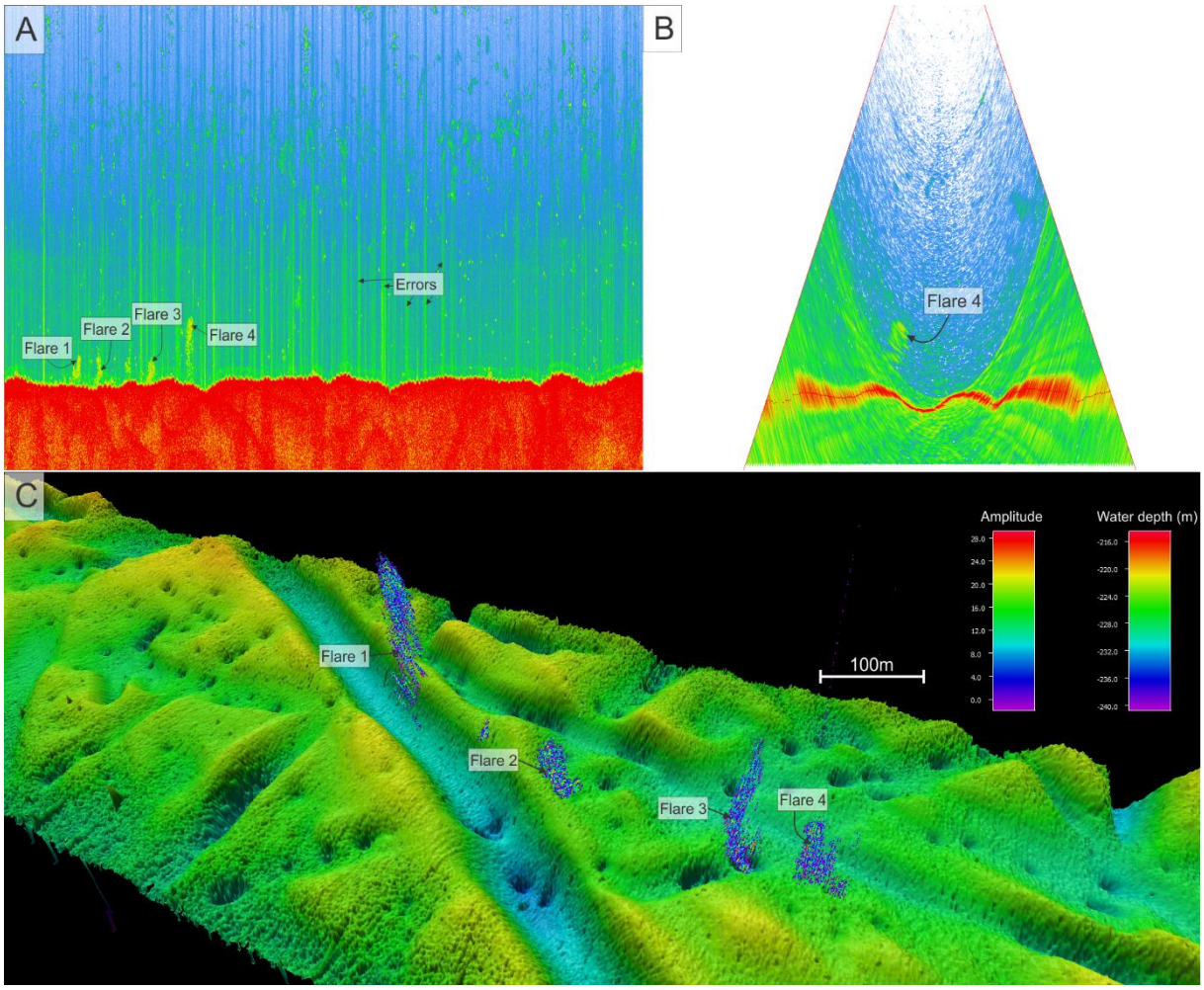

Figure 4.26: Water column anomalies at line 1199 (Figure 4.19 and 4.25). A) R-stack view of what might be potential flares indicated as flare 1,2,3 and 4. B) Fan view of the possible flare 4. C) 3D view of the potential flare 1,2,3 and 4, their amplitudes, water depth and minor depressions.

4.6.5 Potential Flare 7 (PF7), line 1248

One potential flare was observed in the water column data at line 1248, displayed as a high amplitude. The shape of the high amplitude is linear with a slight bend and its height is 18 m. PF7 is situated far north in the study area at the boundary between the NB and the BP. The reflectors below the PF7 are semi discontinues, showing minor faults. North of the gas flares in line 1248 (Figure 4.27) opposite dip of the reflector is observed, represented by the K3 horizon, towards the fault furthest north and referred to as structure D (Figure 4.27). The amplitude anomaly increases along the K3 horizon towards the fault north of the flare in line 1248 (Figure 4.27)

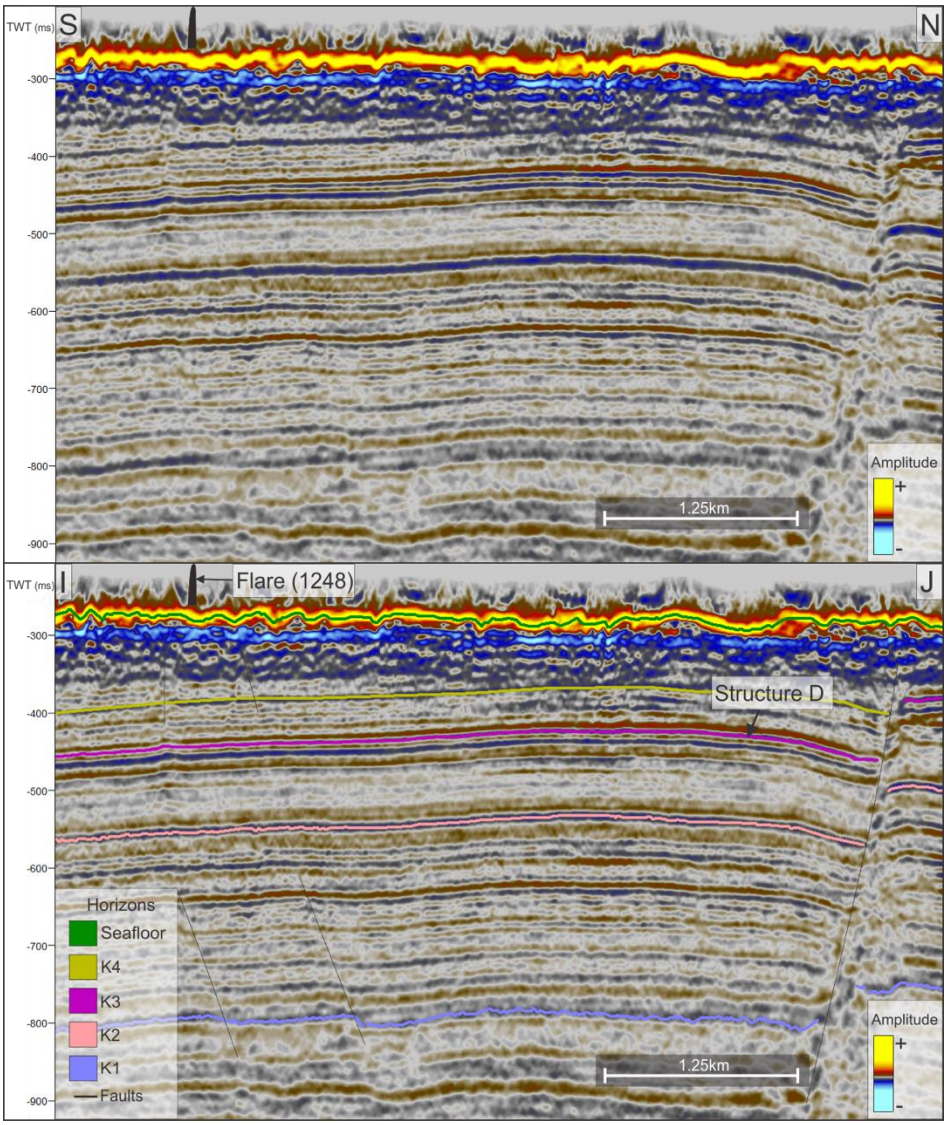

Figure 4.27: Seismic profile (profile 12, I-J, Figure 4.19) shows the location of the potential flare in line 1248, with an underlying fault.

5 Discussion

This chapter is dedicated to discussing the relationship between the observed shallow anomalies and the gas flares presented in the result chapter. Moreover it aims to discuss the potential role of observed structural features and larger structural elements to transport, accumulate and release hydrocarbons.

5.1 Geological development

5.1.1 Lithology and age of the Intra Cretaceous sequences 1-3

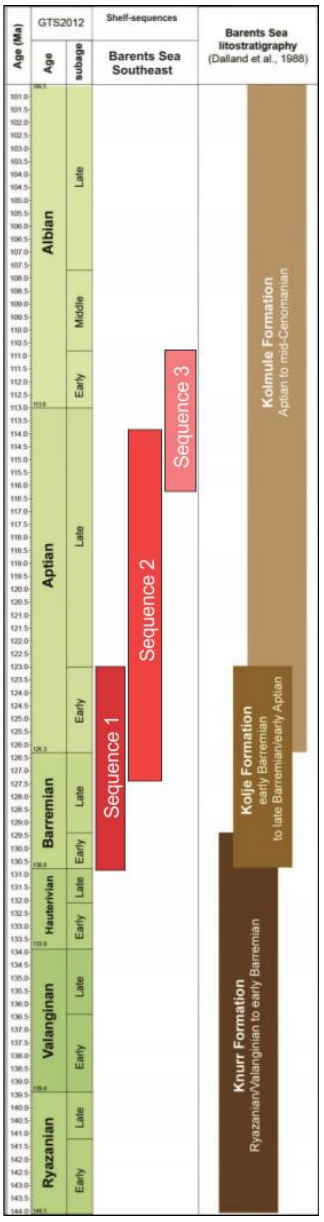

Figure 5.4: Proposed age of S1-S3 for this study, based on Marin et al., 2017; Heiberg 2018. Modified from Grundvåg et al., (2017).

Based on previous studies which can be tied to the study area (Marin et al., 2017); (Heiberg, 2018), the age of each respective sequence within the Intra Cretaceous can be identified. Sequence 1 is interpreted to be deposited during Barremian to Early Aptian age, corresponding to the Kolje Formation (Figure 5.1), whereas sequence 2 suggest deposits of Aptian age corresponding to the Kolje- and Kolmule formations (Figure 5.1). Lastly, sequence 3 is proposed to be of Late-Aptian to Early Albian age, which correlates to the Kolmule Formation (Figure 5.1). Due to lack of well data within the study area as well as the SE Barents Sea in general, uncertainties exist regarding the implied ages of each respective sequence (S1-S3).

Early Barremian- Early Albian

Well 7119/12-1, 7228/7-1A and 7124/3-1, which lies 15.5-29.5 km southwest of the study area (Figure 3.5) and shallow cores used in Bugge et al., 2002 (Figure 3.6) suggest that the Early Barremian to Early Albian is dominated by dark grey marine claystone with silty parts within the Nordkapp Basin and contains kerogen type 3 and 4. Therefore, the potential for petroleum generation is low, despite the total organic content (TOC) is between 1.1-3.8%.

Thickness maps of S2 and S3 suggest a relatively uniform thickness between the Nordkapp Basin and Bjarmeland Platform (Figure 4.6 B-C), which are indication of a low relief during deposition of these units. The shelf break marks the transition from shallow marine to deep marine environment. The Cretaceous stratigraphy in the study area is part of a larger clinoform system, transported towards the shelf margins (Marin et al. 2017; (Grundvåg et al., 2017) and are dipping towards the SW (Figure 4.9). During Aptian to Early Albian when sequence 2 and 3 were deposited, the shelf break was located SW of the NE subbasin, within the central subbasin of the Nordkapp Basin, prograding from the elevated areas in the northeast towards the southwest (Marin et al. 2017; Grundvåg et al. (2017). The northeast subbasin was most likely dominated by shallow marine deposits during this period, as opposed to the areas further south and west i.e. Bugge et al., (2002). Shallow marine environments might have higher energy regimes than the deeper

marine environments, and intervals of sands in the NE subbasin has also been proposed by Rojo et al., 2018.

5.1.2 Faults

The Nordkapp Basin has been through several tectonic episodes and is characterized as a fault-controlled basin. The basin is suggested to be developed in Late Paleozoic time and may be subdivided into three subbasin (Rojo et al., 2019). The orientation of the Late Paleozoic structural elements is generally NE-SW in the eastern Barents Sea, forming the foundation of weak zones. NE-SW striking faults is therefore prevalent in the eastern Barents Sea, where later reactivation of faults in Mesozoic and Cenozoic follows these zones of weakness (R. H. Gabrielsen et al., 1990). The Thor Iversen Fault Complex (TIFC) marks the southeastern boundary of the SE subbasin and has extensional characteristics, inheriting the NE-SW orientation in the eastern parts (R. H. Gabrielsen et al., 1990). The Nordkapp Basin is also closely related to salt pillows along the TIFC, forming salt cored anticlines along the complex (Rojo et al., 2019).

The main trend of the mapped faults in the study area is their termination below the URU and below the top Hekkingen Formation, both originating in Late Paleozoic to Early Triassic (Figures 4.9 - 10). The Upper Regional Unconformity (URU) appears not to be affected by the underlying faults, suggesting that they occurred prior to the Plio-Pleistocene glaciations (Lasabuda et al., 2018). The faults show a trend of increase in fault throw magnitude with depth (chapter 4.4), indicating several episodes of activation and reactivation of the faults. The faults terminating below the top Hekkingen Formation (Figure 4.9), likely occurred prior to the deposition of top Hekkingen Formation, in Late Jurassic time. The Cenozoic succession in the study area is missing, making it difficult to conclude when exactly the fault was reactivated during this age. The displacement of the Kolje and Kolmule Formation is constant, and lower than that of top Hekkingen Formation (Figure 4.2-3). This may suggest inactive faults during the deposition of the units and reactivation post deposition of the Kolmule Formation. The faults along the TIFC appears therefore to be reactivated in the Late Jurassic and during Cenozoic, based on the termination and the throw of the faults (Figure 4.2-3 and 4.9-10), which was also previously indicated by (R. H. Gabrielsen et al., 1990). The

dominating strike and dip along the TIFC is generally similar for faults terminating below the URU and below top Hekkingen Formation, with a NE-SW trend in the south gradually changing to S-N striking axis towards the north (Figure 4.10). The dominating dip direction is NW in the south and is gradually changing to westward dip in the north of the faults along the TIFC.

5.1.3 Structural development of structure A

Structure A are located at the northeastern margin of the Nordkapp Basin along the TIFC in the Cretaceous unit (Figure 4.3 A-C). The Structure has slight dome shaped anticline characteristic and is associated with rotated blocks (Figure 5.3). Generally it is assumed that the TIFC is of an extensional nature (R. H. Gabrielsen et al., 1990), but the slight dome feature of structure A (Figure 4.3 A-C) could possibly indicate some compressional or transpressional movements. The outline of Structure A might also be affected by reactivation of the underlying salt pillow during Cenozoic contraction, which could have caused a salt-cored anticline, as suggested by Rojo et al., 2019. The salt pillow below structure A is mapped as the most extensive salt pillow within the Nordkapp Basin (Rojo et al., 2019).

5.1.4 Structural development of structure B

Structure B are also located along the TIFC south of structure A (Figures 4.3B, 4.16-18 and 5.4), forming a four-way closure. The structure is directly related to the TIFC and are assumed to have the same geological development as structure A.

5.1.5 Structural development of structure C

Meteorite craters are formed as a response to meteorites bombarding the earth's surface, resulting in massive shock waves as the projectiles hit the surface (Westbroek & Stewart, 1996). Meteorite craters can be categorized as either small simple craters, which is typically 2-4 km (2km for sedimentary rocks and 4 km in igneous rocks) in diameter or larger complex craters (Mazur et al., 2000). Larger complex craters usually have a central uplift (8% of the craters diameter) as oppose to small simple craters. The flanks of an impact crater are

typically marked by a rim uplift together with faults. Historically, craters are often associated with economic deposits such as Cu, Ni, hydrocarbons etc, dramatically increasing the interest for meteorite exploration (Westbroek & Stewart, 1996). The structural character of the meteorite craters is well suited as potential traps for hydrocarbon migration, accumulating typically along the flanks of the impact crater (Westbroek & Stewart, 1996).

The circular shaped structure located northwest in the study area (Figures 4.3 B-C) has many similarities to the Mjølnir Crater, although in different scales. The Mjølnir Crater has a diameter of 50 km and is located in the Bjarmeland Platform, about 20 km west of the study area. Both structures show rim faults along the flanks of the structure and a central uplift (Figure 4.15)(Shuvalov et al., 2002). Based on these similarities, the circular shaped structure is likely to be a meteorite crater and is informally referred to as Thor`s crater. There are however no articles on this impact crater and, therefore, it has not officially been recognized as a meteorite crater yet. "The Thor`s crater" has a diameter of 4.5 km (Figure 4.14 and 4.15), the rim to floor depth is about 1.2km (Figure 4.15) and the central uplift is about 0.6 km (Figure 4.15) (13% of the craters diameter). The lithology in proximity of the impact crater is suggested to be of sedimentary origin, indicating that the crater is large enough to be classified as a large complex crater, supported by the central uplift within the crater. The formation of the Thor`s crater occurred prior to the deposition of top sequence 3 (K4), suggesting Early Albian (Figure 5.1).

5.2 Hydrocarbon source rocks

The average geothermal gradient of the Barents Sea is estimated to be about 30 °C/km (Laberg et al., 1998). Due to the thermal effect produced by the salt structures within the Nordkapp Basin, the geothermal gradient may vary from 22 to 69 °C/km (Bugge et al., 2002). The salt diapir within the study area is located just below the seafloor/URU and might have a general cooling effect on the adjacent strata. This is because the heat will be transferred to the top of the diapir, the lateral extent of such a thin diapir is however limited.

The generated isochron maps shows that the stratigraphy in the Nordkapp Basin generally is deeper compared to on the Finnmark and Bjarmeland platforms (FP and BP) (Figures 4.2-4.3 and chapter 4.1). The Nordkapp Basin also holds thicker sediments compared to the BP and FP. According to (Cedeño et al., 2019), the maturation of potential oil-prone Permian source

rock in the Nordkapp Basin stopped as a response to Oligocene uplift. However, the Permian source rock in the eastern subbasin are mature SW of the study area and overmature within the study area, as modelled by (Cedeño et al., 2019). This could suggesting that any observed hydrocarbons within the study area are not likely to occur from Permian source rock generating today, although long distance migration from the SW cannot be completely ruled out. In the paper of Cedeño et al., (2019), Middle to Upper Triassic gas and oil prone source rocks were estimated to be well within the oil window, which is also realistic for the study area, based on the depth of the Middle to Upper Triassic is situated.

Based on the wells situated within and adjacent to the Nordkapp Basin (Figure 3.5) and the shallow cores from Bugge et al., 2002 (Figure 3.6) the youngest source rock within the NB, is the Hekkingen Formation, with a TOC of about 10 wt%, and with kerogen type II and III. However, the Hekkingen Formation within the study area has been calculated to have a maximum depth of 1750 meters, which corresponds to a temperature of 52.5 °C based on normal geothermal gradient of 30 °C/km. The estimated temperature of the Hekkingen Formation is likely lower due to the adjacent salt diapir and the formation most likely is not active within the study area today (Cedeño et al., 2019) (Figure 5.2)). According to Henriksen et al. (2011a), 1500 meters of sediments (mainly Cenozoic) have been removed due to glacial activity, indicating that the Hekkingen Formation has potentially been generating hydrocarbons within the study area at some point, but this has most likely stopped due to (late) Cenozoic uplift and erosion.

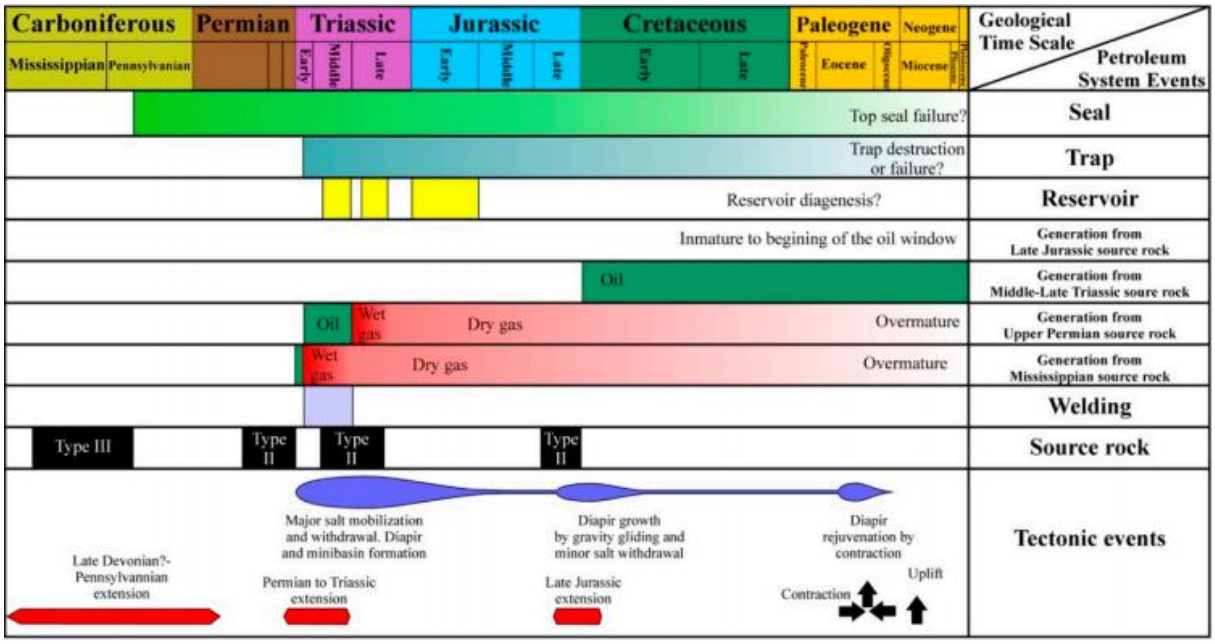

Figure 5.5: Petroleum system events chart of the Nordkapp Basin. Acquired form (Cedeño et al., 2019)

Based on the above, the oil-prone Middle-Late Triassic source rock is the most likely currently hydrocarbon-generating unit within the study area.

5.3 Faults and hydrocarbon migration along the Thor Iversen Fault Complex

5.3.1 Hydrocarbon migration along TIFC

Amplitude anomaly A1-A9, represent strong amplitudes with a reverse polarity compared to the seafloor, categorized as bright spots (chapter 3.2.1.1). Bright spots are usually associated with gas, which might also be the case for A1-A9. There are no boreholes in the area to confirm this, but adjacent wells (Figure 3.5, well 7124/3-1, 7226/11-1 and 7435/12-1) indicate the presence of gas (Table 3.2), shallow cores from Bugge et al. 2002 and well 7228/7-1 also indicate oil (Table 3.2). The closest well 7435/12-1 (Korpfjell) is located 9 km north of the study area, which is far, but increases the possibility of gas within the study area. Lithology changes can also result in amplitude anomalies with a reverse polarity, e.g.

intervals of sand overlying organic rich shale, another explanation may be tuning thickness on truncating units or a combination of these factors.

The Thor Iversen Fault Complex (TIFC) stretches from S-N throughout the study area and is associated with majority of the amplitude anomalies observed in the study area (A1-A2 and A4-A8, Figure 4.13 and 4.17-18). Faults can be categorized as either sealing (non-conductive) or open/leaking (conductive) (Ligtenberg, 2005). Leaking faults act as fluid conduits allowing migrating along the fault plane through sealing sequences etc., whereas sealing faults are not conductive and, thus may form structural traps. Amplitude anomalies (A1-A2 and A4-A8) are observed adjacent to certain faults adjacent to the TIFC, where the highest amplitudes (marked as A1-A2 and A4-A8) along the complex is associated with structure A (Figure 4.13 and 5.3) and structure B (Figure 4.17-18 and 5.4), with faults terminating in the URU. In contrast, majority of the faults along the TIFC shows no association with bright spots, suggesting either lack of hydrocarbons or sealing faults. Entire fault planes are seldom leaking, occurring rather along weak locations in the fault zones. Leakage along faults usually occur as a response to zones of weakness caused by fault intersections, fault complexities or fault plane irregualrities (Ligtenberg, 2005).

The SE-subbasin (Figure 3.5) is generally underexplored in terms of hydrocarbons exploration, as the primary focus for exploration has been the western sub-basin and is where the exploration wells are drilled (Figure 3.5). However, hydrocarbon shows and migration paths has been suggested along the TIFC in 2D seismic by Rojo et al. 2019. Strong amplitude anomalies possibly representing gas bearing rocks are detected in the strata in proximity to the TIFC (A1-A2 and A4-A8), suggesting active migration of gas originating from deeper parts of the fault and/or deeper parts of the Nordkapp Basin, seeping into permeable beds adjacent to the fault and accumulating in structure A and structure B (A1-A2 and A4-A8) (Figure 4.13, 4.17-18, 5.3 and 5.4). The potential shallow gas is generally observed at four stratigraphic levels along the TIFC (K1, K2, K4 and URU), which are situated adjacent or above the faults (Figure 5.3), possibly serving as conduits for migrating gas. A1 and A2 represent the anomalies directly above the faults (Figure 4.13), whereas A4-A8 are located adjacent to the faults along the TIFC. The possible shallow gas observed in proximity to the TIFC occurs along SW dipping faults. In contrast, SE dipping faults show no indications of shallow gas (Figure 4.9).

5.4 Hydrocarbon accumulation of the Intra Cretaceous sequences (1-3)

5.4.1 Hydrocarbon accumulation and sealing capacity

Potential Reservoirs

Reservoir quality is influenced by porosity and permeability, parameters which often decrease with depth due to increasing temperature and pressure enhancing diagenetic changes (e.g. compaction and cementation). The cooling induced by the salt diapirs in the Nordkapp Basin could therefore decrease the effect of the diagenesis on the Triassic, Jurassic and Cretaceous reservoirs, potentially increasing the reservoir quality (Cedeño et al., 2019). The best reservoirs within the Nordkapp Basin are assumed to be represented by the Fruholmen- and Stø formations and parts of the Kobbe Formation (Bugge et al., 2002), which lies between the interpreted Havert- and Fuglen formations. The observed anomalies in the study area which may represent gas seems to accumulate in the Upper Triassic to Lower Jurrassic and the Cretaceous represented by the Kolmule Formation. The Kolmule Formation are not known as a reservoir rock in the Nordkapp Basin and are likely dominated by shale. However, there are no wells in the NE subbasin and the depositional environment is suggested to be different from where the unit is drilled (se earlier discussion), which is why the potential reservoir properties of this unit in the study area are unknown, but intervals of potential reservoir cannot be ruled out.

Sealing capacity

During the Mesozoic and Cenozoic it is assumed that the diapirs continued to grow and several reactivations of suprasalt fault arrays along the basin boundaries have been identified by (Rojo et al., 2019). The result of this may have changed or even ruined structural traps and also the sealing capacity, leading to hydrocarbons leaking out of the system or redistributed to shallower traps (Rojo & Escalona, 2018). The extensive regional uplift in Cenozoic led to erosion and is also an important factor to consider in terms of hydrocarbon expulsion, as it may lead to top seal failure, remigration or hydrocarbon phase separation (Henriksen et al., 2011). The petroleum system in the Nordkapp Basin is very complex because of the deep

hydrocarbon generation of the source rock in addition to the destruction and change in the traps, resulting in flushing of older traps thereby mixing hydrocarbons of different ages (Figure 5.2) (Cedeño et al., 2019). Calculation based on Nyland et al. (1992) suggest increase in gas volume leading to over pressure and resulting in frequent fracture zones along cap rocks within the Nordkapp Basin.

5.4.2 Hydrocarbon accumulation and sealing capacity of the main stratigraphic traps

The shallow amplitude anomalies are located along the Thor Iversen Fault Complex in four stratigraphic levels (K1, K2, K4 and URU) and seems to accumulate in structure A, B and C (Figure 4.13-14 and 17-18), which will be described the below.

The Cretaceous succession comprising of marine claystone with intervals of sandstone (Rojo et al.,), display amplitude anomalies (A1-A2 and A4-A8) adjacent to the faults along the Thor Iversen Fault Complex. The shallow anomalies are proposed to be shallow gas and appear to seep into the adjacent strata where the leaked gas is sealed off by overlying lower permeability units (Figure 4.13 and 4.15). Permeable sandstone may function as a conduit for the migrating gas, whereas the overlying claystone acts as an impermeable barrier, sealing the vertical advance of the gas. This may also apply to the eastward dipping strata, where amplitude anomalies with reverse polarity appears to increase towards the upper truncations (Figure 4.9, 4.23 and 4.25), which is below the URU/seafloor along several reflectors towards the Fedinsky High. The increase of amplitude towards the upper truncation can be indication of hydrocarbons as it has reverse polarity and relatively high amplitude. Yet, lithology or/and tuning may serve as an alternative explanation. The mapped anomalies and associated structures are categorized accordingly: a) Structure A, associated with A1-A2, A4-A5 and A7-A8. b) Structure B linked to A6. c) Structure C, a meteorite crater associated with A3. There is strong correlation between the observed seismic anomalies (A1-A8), faults, structure A-C and the overlying seemingly impermeable units (K1, K2, K4 and URU). This increases the possibility that the mapped amplitude anomalies (A1-A9) represent gas.

5.4.2.1 Structure A

The amplitude anomalies A1-A2, A4-A5 and A7-A8 are associated with faults along the TIFC and a major dome structure, structure A (Figure 4.13), where each of these strong amplitudes represents structural highs, situated in the central parts of structure A. The possible migration of hydrocarbons in Figure 5.3 display possible lateral and vertical migration paths of the potential hydrocarbons into structure A. The faults categorized in the result chapter as F1 and F2 (Figure 4.13) display amplitude anomalies potentially representing gas, in different stratigraphic levels (K1, K2 and K4) of the Cretaceous unit adjacent to these faults. Amplitude anomalies adjacent to F1 and F2 were also observed in the Upper Triassic (Figure 5.3), suggesting that these faults are potentially working as migration pathways. Strong amplitude anomalies with reverse polarity can also be observed along the Cretaceous reflectors, increasing towards structure A (Figure 4.13). This may indicate lateral migration, assuming the anomalies represent hydrocarbons. A1 and A2 is introduced as the strongest amplitude anomalies in the study area and is located just above F1 and F2, sealed by the URU with no adjacent indications of gas, which may suggest that the assumed gas originates from the vertical migration, whereas A4-A5 and A7-A8 likely originate from a combination of lateral and vertical migration (Figure 4.13 and 5.3). Even though F1 and F2 are suggested to be leaking, the leakage isn't necessarily continuous and may be part of a dynamic system, where the assumed gas is preserved below K1, K2 and K4 until the pressure builds up to a certain point, resulting in some of the gas leaking upwards and thereby releasing the pressure. Most of the gas is left behind and this process are repeated again when the pressure are sufficient.

5.4.2.2 Structure B

The minor elongated structure B has a similar trend to that of the structure A, the main difference is the type of closure, scale and complexity of the structures (Figures 4.17-18 and 5.4). Structure B represent a four-way closure at the base of sequence 3 (K2) (Figure 4.3B, Chapter 4). Amplitude anomaly 6 located along/below structure B/base sequence 3 (K2) mirrors the outline of the structure, with an associated potential flat spot below the anomaly (Figure 4.17-18), which might represent a hydrocarbon – water contact (chapter 3.6.1). The fault classified in the result chapter as F3 is situated in proximity to structure B and display amplitude anomalies (representing bright spots) adjacent to the fault in different stratigraphic

levels (Upper Triassic and Cretaceous, Figure 5.4). Suggesting this fault may work as a migration pathway. Increased amplitudes (with reverse polarity compared to the seafloor) can also be observed above the structure (Figure 4.17-18), which might represent leakage from structure B, migrating along F3 to shallower levels, possibly explained by a dynamic system model as explained above for structure A.

5.4.2.3 Structure C

Amplitude anomaly 3 is situated along the top of sequence 3 (K4), at the flanks of the above discussed impact crater (Figure 4.14). No shallower anomalies (or gas flares, see below), suggest that the top of sequence 3 functions as an impermeable barrier sealing potential hydrocarbons within the impact crater (Figure 4.15). Below the potential meteorite crater, relatively high amplitudes with reverse polarity is observed along the base of sequence 3 (K2) (Figure 4.15). The faults along the flanks of the crater may have worked as migration pathways, migrating from the base of sequence 3 (K2) to the top (K4) towards amplitude anomaly 3 (Figure 4.15).

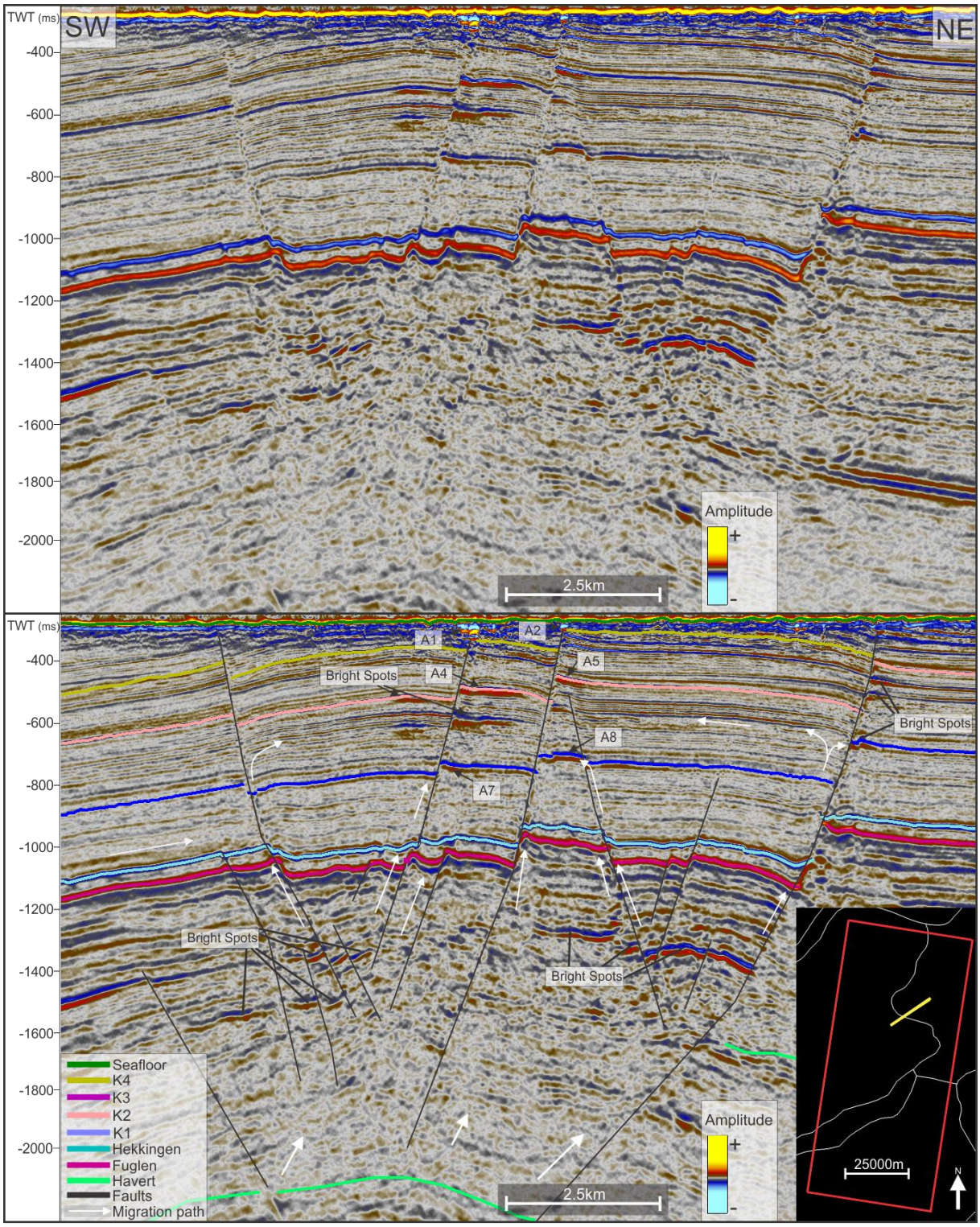

Figure 5.6: Seismic profile displaying the migration paths of the deep anomalies towards structure A.

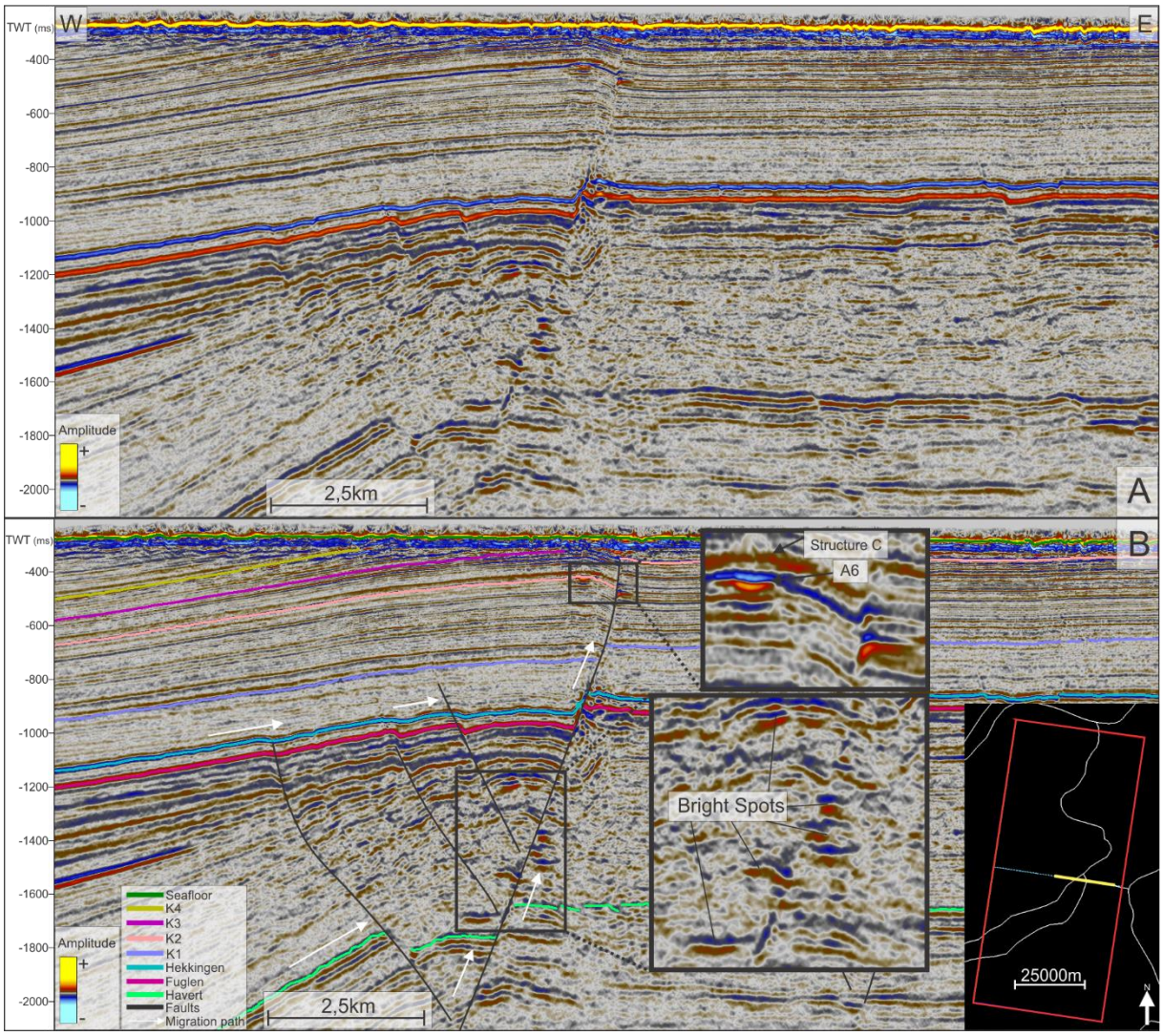

Figure 5.7: Seismic profile displaying the migration paths of the deep anomalies towards structure B.

5.5 Potential gas Flares

The potential flares observed in the result chapter will be further evaluated below. The confidence of the individual gas flares, varies based on the amplitude of the gas flares, topographic features on the seafloor and subsurface parameters which will be discussed in this subchapter.

5.5.1 Amplitude and height of the gas flares

The different flares have a relatively weak amplitude compared to the seafloor (Figure 4.22, 4.24 and 4.26) and a height ranging from 8-22 meters, giving rise to a relatively low confidence that they are caused by seeping gas, when compared to other gas flares in the Barents Sea, which often exceed 200 meters and have a strong amplitude compared to the seafloor (Chand et al., 2012). Another explanation for the height and the weak amplitude of the gas flares may be a weak gas flow, as a result of overlying sediments which are partially sealing or a low concentration of gas below the flares. The weak amplitude of the different flares is almost identical, the only exception are the gas flares in line 2203, which both have a slightly stronger amplitude (Figure 4.22). The gas flares in line 2203 have the largest underlying amplitude anomaly of the seven lines with gas flares (4.21), likely resulting in a slightly stronger flow, mirrored by amplitude of the flares in line 2203.

5.5.2 Topographic features at the seafloor

The observed elongated depressions observed throughout the seafloor (Figure 4.4B) are interpreted to be plough marks (Belderson et al., 1973). Plough marks seem to dominate the seafloor throughout the study area and are indications of iceberg activity. The seafloor showed no other topographic features that might be linked to the gas flares, such as pockmarks, mounds, mud volcanos etc. However, 3D view of the seabed (from Fledermaus, Figure 4.22, 4.24 and 4.26) displayed minor pockmarks, marked as circular depressions with a diameter ranging from 15-40 m and reaching a few m in depth, despite being unrecognizable on the 3D seismic horizon representing the seafloor (Figure 4.4B). This is due to higher resolution of the water column data compared to the 3D seismic. There are in total three lines (1199, 1987 and 2203) with 3D view of the flares, in which the flares in line 2203 are not associated with any specific topographic features (Figure 4.22). The gas flares in line 1199 (Figure 4.26) and 1987 (Figure 4.24), show a few of the gas flares in association with pockmarks, even though the majority of the pockmarks have no connection with the flares. The pockmark could have formed as a response to the gas flow, or it could be water outflow from the sediments experiencing compaction (Harrington, 1985). Most of the pockmarks are not active and are therefore not likely related to gas seepage.

5.5.3 Subsurface parameters associated with potential gas flares

The combination of 3D seismic and water column data across the study area indicate that the potential gas flares occur where the subsurface formations: a) Show faults associated with the Thor Iversen Fault Complex and the salt diapir, terminating below the URU. (Line 1248 (Figure 4.27), 3489 (Figure 4.20), 1987 (Figure 4.23)). b) Shallows and terminates below URU towards the Fedinsky High (Line 1199, 1195 and 1192 and Figure 4.25). c) Display shallow gas within the NB below the seafloor (Line 2203, Figure 4.21).

5.5.3.1 Faults related to potential gas flares

The study area is influenced by faults along the TIFC and the flanks of the salt diapir situated within the NB (Figures 4.10). Several of the potential gas flares occur above shallow faults terminating towards the URU/seafloor (line 3489, 1987 and 1248)). The TIFC is closely related to shallow amplitude anomalies which might represent hydrocarbons – potentially gas, and are observed in many stratigraphic levels (K1, K2 and K4, represented by anomalies A1-A2, A4-A8) in the Cretaceous. Two lines with observed gas flares are located along the TIFC, line 3489 and 1248 (Figure 4.19), whereas the potential gas flares in line 1986 (Figure 4.19) is associated with faults adjacent to the salt diapir within the study area.

The geology in structure B (Figure 5.4) is almost identical to the geology just north of the gas flares in line 1248 (Figure 4.27), with the same orientation and dip of the faults along the TIFC and opposite dipping reflectors, which can be characterized as structure D (Figure 4.27). The K3 reflector below the gas flares at line 1248 show an increasing amplitude anomaly with a reverse polarity, potentially representing hydrocarbons migrating towards the fault 4 km north of the gas flares (Figure 4.27) below structure D. The fault below the potential gas flares in line 1248, may have worked as a migration pathway for the potential hydrocarbons along K3, towards the URU/seafloor.

Potential gas flares was also observed in line 3489, east of structure B and the underlying amplitude anomaly 6 (Figure 4.20). No indications of potential gas flares is observed above structure B, even though amplitude anomalies below the seafloor is present. Potential gas flares in line 3489 is observed above a fault (Figure 4.20), which may function as a migration pathway towards the seafloor, despite the lack of hydrocarbon indicators along the fault.

Potential gas flares in line 1987 are located above a fault (Figure 4.23) along the flanks of the salt diapir within the Nordkapp Basin in the study area, likely formed as a response to halokinesis from the piercing diapir. Strong amplitude anomalies with reverse polarity, potentially representing gas, is observed below the seafloor and at different stratigraphic levels along the fault (Figure 4.23). A scenario where the fault function as a migration pathway is therefore plausible.

5.5.3.2 Truncations

Three out of the seven potential gas flares are located above truncations of intra Cretaceous reflectors towards the seafloor/URU towards the Fedinsky High (Line 1199-1195-1192 Figure 4.25). A general shallowing of all stratigraphic boundaries is apparent towards the Fedinsky High in the east of the study area, where the Upper-Middle Cretaceous reflectors eventually terminates towards the URU (Figure 4.25 and 4.3C-D). Termination of the Intra-Cretaceous reflectors can also be observed along the flanks of the salt diapir within the Nordkapp Basin (Figure 4.7). As the reflectors shallows towards the east, the amplitude increases towards the upper termination within sequence 1, with a reverse polarity compared to the seafloor. This might represent lithology changes or possibly fluids or gas from deeper parts following permeable formations towards the truncations, and potentially explaining the observed gas flares above these truncations at line 1199, 1195 and 1192 (Figure 4.19).

5.5.3.3 Shallow amplitude anomaly 9 (A9)

Amplitude anomaly 9 is located within the Nordkapp Basin and are situated above the top of sequence 3 (Figure 4.21), close to the seafloor. The anomaly has a reverse polarity compared to the seafloor and can be interpreted as a bright spot which are usually related to gas, although lithology changes are also possible explanations.

The gas flares located within line 2203 has the highest amplitude of the observed flares in this study and a height of 15 and 22 meters (Figure 4.22), which is among the tallest flares. These flares presumably originates from the distinct shallow amplitude anomaly (A9) below the gas flares (Figure 4.21), giving rise to a relatively high confidence tied to these flares. The overlying gas flares might suggest that the amplitude anomalies observed below are representing gas, migrating towards the upper truncation to the north.

5.5.3.4 Upper regional unconformity

The Cretaceous sediments in the study area are separated from the overlying glacial sediments by a regional unconformity, called the upper regional unconformity. This unconformity is defined as a thin cover of glacigenic sediments of Pliocene–Pleistocene age (about 2.5 M) truncating older units (Andreassen et al., 2008). The glacigenic sediments deposited above the URU are generally till, originating from ice sheets. Glacial tills often have relatively good sealing properties. The last glacial maximum eroded away major parts of the older glacigenic sediments in the SE Barents Sea, and in areas did not deposit any substantial layer of new glacigenic sediments (Lasabuda et al., 2018).

The URU within the study area is only mapped within a few areas in the northern and southernmost parts (Figure 4.4A). Amplitude anomalies with reverse polarity were observed throughout the study area and were interpreted as either lithology changes or hydrocarbons. A1 and A2 (Figure 4.13) are situated below the seafloor, potentially representing shallow gas. Leakage in the water column data was therefore a possibility, lack of visible glacigenic sediments (Figure 4.4A) above the anomaly, increases this possibility as the seafloor does seldom have sealing properties. A sizeable strong amplitude anomaly (A9) with reverse polarity (given standard polarity) can also be observed below the seafloor (Figure 4.21), which are located close to line 2203 (Figure 4.22), with no detectable glacigenic sediments below (Figure 4.4A). Water column data show no indication of potential gas flares above A1 and A2, whereas the potential gas flares observed in line 2203 are located above A9, even though both cases represented bright spots and lacked overlying glacigenic sediments (missing URU). This may be because the glacigenic sediments are in fact present and is too thin to be observed on the 3D data, functioning as an impermeable barrier, preventing the potential hydrocarbons in A1 and A2 from migrating. Calculation of the minimum thickness of the reflector representing the URU shows that it ought in some cases to exceed 40 meters to be visible in the 3D seismic. The potential gas flares on the other hand, represent possible signs of gas leaking through the seafloor/URU, and glacigenic sediments are therefore likely to be missing/thinner, of less impermeable lithology or have a stronger gas migration in these areas.

6 Summary and conclusion

In the NE sub-basin of the Nordkapp Basin in the Barents Sea, a combination of 3D seismic- and water column data allowed for detailed mapping of shallow seismic anomalies, shallow sub-surface structures and faulting potentially linked to gas flares in the water column.

Three structures (structure A-C) have been emphasized, together with the relation between possible vertical and lateral migration pathways, potential hydrocarbon accumulations in subsurface structures, and possible linkage to flares in the water column.

- The mapped anomalies (A1-A8) are primarily observed in the Cretaceous Kolmule- and Kolje Formation (sequence S1-S3), and are suggested to represent bright spots, situated within the structures A-C.
- Structure A (located along the K3 horizon) and B (located along the K2 horizon) are both related to fault blocks along the Thor Iversen Fault Complex, forming structural closures, possibly during Cenozoic. Structure C (located below the K4 horizon) is believed to be formed as a response to an impact from a meteorite during Early Albian.
- Amplitude anomalies situated within the structure A (A4-A5 and A7-A8), is limited by the top and base of sequence 2 (K2 and K1) working as potential impermeable barriers, bounded by the faults F1 and F2 in the Thor Iversen Fault Complex. The accumulations within structure A, are possibly originating from vertical and lateral migration from deeper seated source rocks.
- Structure B form a four-way closure and are associated with amplitude anomaly (A6), where the top of sequence 2 (K2) possibly work as an impermeable barrier.
- Indications of amplitude anomalies are observed above structure A (A1-A2) and B, possibly originating from hydrocarbons leaking through faults associated with the TIFC, through dynamic systems.
- Structure C is associated with amplitude anomaly 3, and are lacking indications of overlying amplitude anomalies, which may suggest that top of sequence 3 (K4) function as an impermeable barrier in this structure.
- There are observed no potential gas flares above structure A, B and C, which could indicate that the structures are sealing, making them interesting for future evaluation.

- Amplitude anomalies below the URU, are likely to represent minor gas accumulations and for the most part show no signs of leakage above, which may be due to glacigenic sediments acting as an impermeable barrier.
- Potential gas flares are observed on seven lines out of the 3868 lines within the study area, associated with relatively weak amplitude, suggesting a corresponding weak gas flow, potentially indicating low concentration/supply of gas or sealing of potential gas migrating upwards.
- Each respective flare is associated with amplitude anomalies possibly representing gas, despite the weak amplitude. The subsurface features such as truncations, faults and bright spot (A9), increases the possibility of gas leakage causing the individual flares. Observing potential gas in the area, could increase the possibility of gas being associated with the above mentioned seismic anomalies within structures A, B and C.

7 References

Anderson, M. (2011). *Investigating Plate Tectonics, Earthquakes, and Volcanoes*: Britannica Educational Publishing.

Andreassen, K., Hubbard, A., Winsborrow, M., Patton, H., Vadakkepuliyambatta, S., Plaza-Faverola, A., . . . Mattingsdal, R. (2017). Massive blow-out craters formed by hydrate-controlled methane expulsion from the Arctic seafloor. *Science, 356*(6341), 948-953.

Andreassen, K., Laberg, J. S., & Vorren, T. O. (2008). Seafloor geomorphology of the SW Barents Sea and its glaci-dynamic implications. *Geomorphology, 97*(1-2), 157-177.

Andreassen, K., Nilssen, E. G., & Ødegaard, C. M. (2007). Analysis of shallow gas and fluid migration within the Plio-Pleistocene sedimentary succession of the SW Barents Sea continental margin using 3D seismic data. *Geo-Marine Letters, 27*(2-4), 155-171.

Belderson, R., Kenyon, N., & Wilson, J. (1973). Iceberg plough marks in the northeast Atlantic. *Palaeogeography, Palaeoclimatology, Palaeoecology, 13*(3), 215-224.

Brown, A. (2004). Interpretation of three-dimensional seismic data: The American Association of Petroleum Geologists and the Society of Exploration Geophysicists. *Tulsa, OK, 535*.

Bugge, T., Elvebakk, G., Fanavoll, S., Mangerud, G., Smelror, M., Weiss, H. M., . . . Nilsen, K. (2002). Shallow stratigraphic drilling applied in hydrocarbon exploration of the Nordkapp Basin, Barents Sea. *Marine and Petroleum Geology, 19*(1), 13-37.

Busby, J. (2003). An Introduction to Geophysical Exploration P. Kearey, M. Brooks & I. Hill, Blackwell Publishing, Oxford, 2002, ISBN 632 04929 4,(softback), $29.95. In: Blackwell Publishing Ltd Oxford, UK.

Cedeño, A., Rojo, L. A., Cardozo, N., Centeno, L., & Escalona, A. (2019). The Impact of Salt Tectonics on the Thermal Evolution and the Petroleum System of Confined Rift Basins: Insights from Basin Modeling of the Nordkapp Basin, Norwegian Barents Sea. *Geosciences, 9*(7), 316.

Chand, S., Mienert, J., Andreassen, K., Knies, J., Plassen, L., & Fotland, B. (2008). Gas hydrate stability zone modelling in areas of salt tectonics and pockmarks of the Barents Sea suggests an active hydrocarbon venting system. *Marine and Petroleum Geology, 25*(7), 625-636.

Chand, S., Thorsnes, T., Rise, L., Brunstad, H., Stoddart, D., Bøe, R., . . . Svolsbru, T. (2012). Multiple episodes of fluid flow in the SW Barents Sea (Loppa High) evidenced by gas flares, pockmarks and gas hydrate accumulation. *Earth and Planetary Science Letters, 331*, 305-314.

Faleide, J. I., Tsikalas, F., Breivik, A. J., Mjelde, R., Ritzmann, O., Engen, O., . . . Eldholm, O. (2008). Structure and evolution of the continental margin off Norway and the Barents Sea. *Episodes, 31*(1), 82-91.

Faleide, J. I., Vågnes, E., & Gudlaugsson, S. T. (1993). Late Mesozoic-Cenozoic evolution of the south-western Barents Sea in a regional rift-shear tectonic setting. *Marine and Petroleum Geology, 10*(3), 186-214.

Gabrielsen, R., Farseth, R., Jensen, L., Kalheim, J., & Riis, F. (1990). 1990, Structural elements of the Norvegian continental shelf, part 1: The Barents Sea Region. NPD-bulletin No 6.

Gabrielsen, R., Kløvjan, O., Rasmussen, A., & Stølan, T. (2013). *Interaction between halokinesis and faulting: structuring of the margins of the Nordkapp Basin, Barents Sea region.* Paper presented at the Structural and Tectonic Modelling and its

Application to Petroleum Geology: Proceedings of Norwegian Petroleum Society Workshop, 18-20 October 1989, Stavanger, Norway.
Gabrielsen, R. H., Faerseth, R. B., & Jensen, L. N. (1990). *Structural Elements of the Norwegian Continental Shelf. Pt. 1. The Barents Sea Region*: Norwegian Petroleum Directorate.
Gabrielsen, R. H., Grunnaleite, I., & Rasmussen, E. (1997). Cretaceous and tertiary inversion in the Bjørnøyrenna Fault Complex, south-western Barents Sea. *Marine and Petroleum Geology, 14*(2), 165-178.
Glørstad-Clark, E., Faleide, J. I., Lundschien, B. A., & Nystuen, J. P. (2010). Triassic seismic sequence stratigraphy and paleogeography of the western Barents Sea area. *Marine and Petroleum Geology, 27*(7), 1448-1475.
Grimstad, S. (2016). *Salt tectonics in the central and northeastern Nordkapp Basin, Barents Sea.*
Grundvåg, S.-A., Marin, D., Kairanov, B., Śliwińska, K., Nøhr-Hansen, H., Jelby, M. E., . . . Olaussen, S. (2017). The Lower Cretaceous succession of the northwestern Barents Shelf: onshore and offshore correlations. *Marine and Petroleum Geology, 86*, 834-857.
Gudlaugsson, S., Faleide, J., Johansen, S., & Breivik, A. (1998). Late Palaeozoic structural development of the south-western Barents Sea. *Marine and Petroleum Geology, 15*(1), 73-102.
Harrington, P. (1985). Formation of pockmarks by pore-water escape. *Geo-Marine Letters, 5*(3), 193-197.
Heiberg, V. (2018). *The regional Cretaceous development of the southeastern part of the Norwegian Barents Sea-from seismic interpretation.* UiT Norges arktiske universitet,
Henriksen, E., Bjørnseth, H., Hals, T., Heide, T., Kiryukhina, T., Kløvjan, O., . . . Sollid, K. (2011). Uplift and erosion of the greater Barents Sea: impact on prospectivity and petroleum systems. *Geological Society, London, Memoirs, 35*(1), 271-281.
Hudec, M. R., & Jackson, M. P. (2007). Terra infirma: Understanding salt tectonics. *Earth-Science Reviews, 82*(1-2), 1-28.
Jenyon, M. K. (1986). *Salt tectonics*: Springer.
Larssen, G., Elvebakk, G., Henriksen, L. B., Kristensen, S., Nilsson, I., Samuelsberg, T., . . . Worsley, D. (2002). Upper Palaeozoic lithostratigraphy of the Southern Norwegian Barents Sea. *Norwegian Petroleum Directorate Bulletin, 9*, 76.
Lasabuda, A., Laberg, J. S., Knutsen, S.-M., & Safronova, P. (2018). Cenozoic tectonostratigraphy and pre-glacial erosion: A mass-balance study of the northwestern Barents Sea margin, Norwegian Arctic. *Journal of Geodynamics, 119*, 149-166.
Ligtenberg, J. (2005). Detection of fluid migration pathways in seismic data: implications for fault seal analysis. *Basin Research, 17*(1), 141-153.
Marin, D., Escalona, A., Śliwińska, K. K., Nøhr-Hansen, H., & Mordasova, A. (2017). Sequence stratigraphy and lateral variability of Lower Cretaceous clinoforms in the southwestern Barents Sea. *AAPG Bulletin, 101*(9), 1487-1517.
Mazur, M., Stewart, R., & Hildebrand, A. (2000). The seismic signature of meteorite impact craters. *CSEG Recorder, 25*, 10-16.
Mello, U. T., Karner, G. D., & Anderson, R. N. (1995). Role of salt in restraining the maturation of subsalt source rocks. *Marine and Petroleum Geology, 12*(7), 697-716.
Oglesby, D. D. (2005). The dynamics of strike-slip step-overs with linking dip-slip faults. *Bulletin of the Seismological Society of America, 95*(5), 1604-1622.
Ostanin, I., Anka, Z., di Primio, R., & Bernal, A. (2012). Hydrocarbon leakage above the Snøhvit gas field, Hammerfest Basin SW Barents Sea. *First Break, 30*(11).

Rojo, L. A., Cardozo, N., Escalona, A., & Koyi, H. (2019). Structural style and evolution of the Nordkapp Basin, Norwegian Barents Sea. *AAPG Bulletin, 103*(9), 2177-2217. Retrieved from https://doi.org/10.1306/01301918028. doi:10.1306/01301918028

Rojo, L. A., & Escalona, A. (2018). Controls on minibasin infill in the Nordkapp Basin: Evidence of complex Triassic synsedimentary deposition influenced by salt tectonics. *AAPG Bulletin, 102*(7), 1239-1272.

Shuvalov, V., Dypvik, H., & Tsikalas, F. (2002). Numerical simulations of the Mjølnir marine impact crater. *Journal of Geophysical Research: Planets, 107*(E7), 1-1-1-13.

Siwabessy, P. J. W., Tran, M., Picard, K., Brooke, B. P., Huang, Z., Smit, N., . . . Atkinson, I. (2018). Modelling the distribution of hard seabed using calibrated multibeam acoustic backscatter data in a tropical, macrotidal embayment: Darwin Harbour, Australia. *Marine Geophysical Research, 39*(1-2), 249-269.

Smelror, M., Petrov, O., Larssen, G. B., & Werner, S. (2009). Geological history of the Barents Sea. *Norges Geol. undersøkelse*, 1-135.

Vadakkepuliyambatta, S., Hornbach, M. J., Bünz, S., & Phrampus, B. J. (2015). Controls on gas hydrate system evolution in a region of active fluid flow in the SW Barents Sea. *Marine and Petroleum Geology, 66*, 861-872.

van den Boogaard, M., & Hoetz, G. (2015). *Seismic characterisation of shallow gas in the Netherlands.* Paper presented at the Abstract FORCE Seminar Stavanger.

Westbroek, H.-H., & Stewart, R. R. (1996). The formation, morphology, and economic potential of meteorite impact craters. *CREWES Res. Rep, 8*, 1-26.

Worsley, D. (2008). The post-Caledonian development of Svalbard and the western Barents Sea. *Polar Research, 27*(3), 298-317.